Facilitating Maximum Power Point Tracking by Inductor Integration onto a Crystalline Solar cell

Saurabh Chakravarty

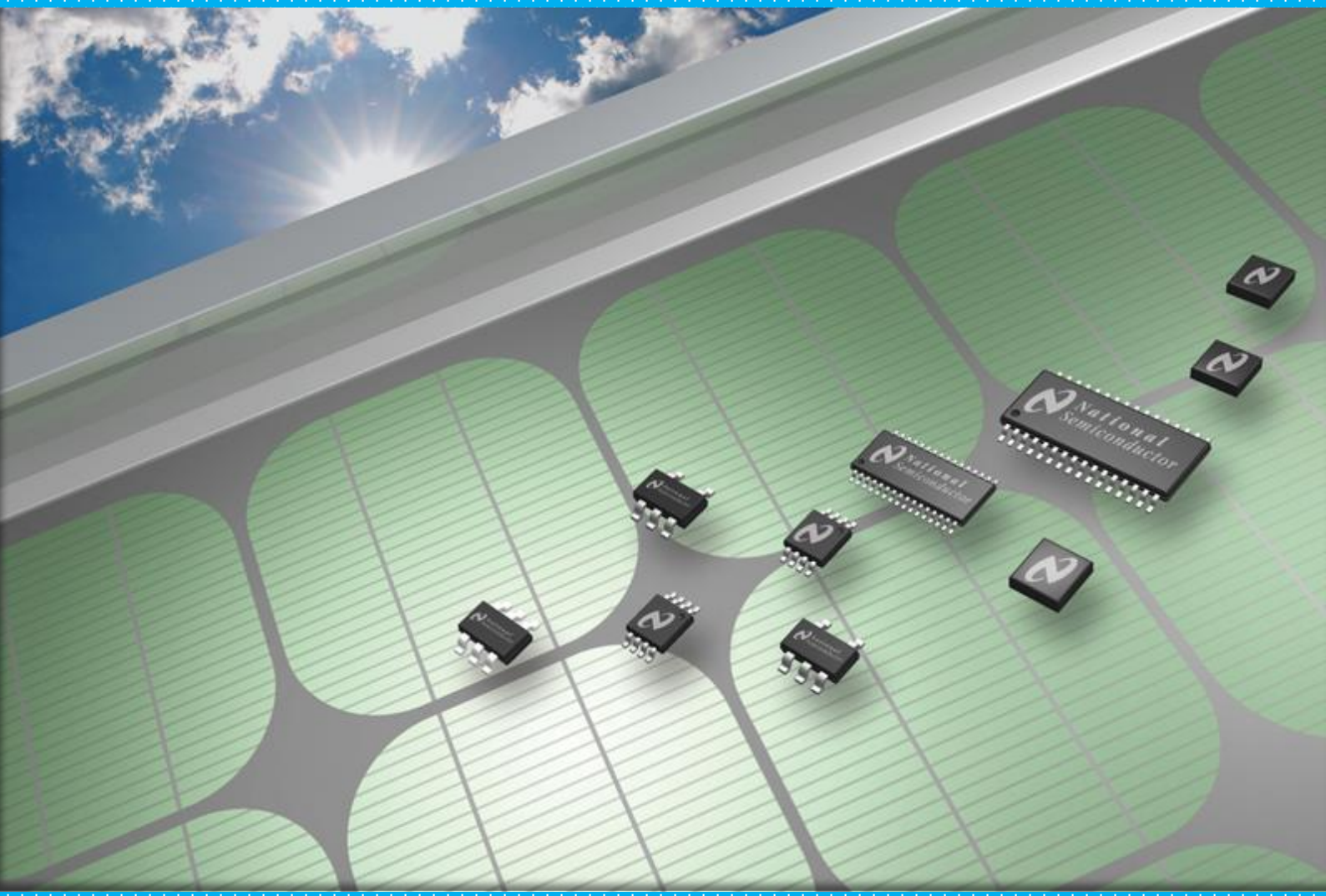

TU Delft Delft University of Technology

PVMD Delft University of Technology

Facilitating Maximum Power Point Tracking by Inductor Integration onto a Crystalline Solar cell

by

Saurabh Chakravarty

to obtain the degree of Master of Science
at the Delft University of Technology,
to be defended publicly on Thursday July 20th, 2023 at 14:30.

Student number:	5597862	
Project duration:	November, 2022 – July, 2023	
Thesis Supervisor:	Dr. R.A.C.M.M. van Swaaij,	TU Delft, Associate Professor, PVMD
	Dr. G.R. Chandra Mouli,	TU Delft, Assistant Professor, DCE&S
	Dr. P. Manganiello,	TU Delft, Assistant Professor, PVMD & Supervisor
	Ir D.A. van Nijen	TU Delft, PhD candidate, PVMD & Daily supervisor

TU Delft

Preface

The report is the outcome of my graduation project, 'Facilitating Maximum Power Point Tracking by Inductor Integration onto a Crystalline Solar Cell.' I completed it as part of my master's program in Sustainable Energy Technology (SET) at the Delft University of Technology. My background in Electronics Engineering has given me an apparent interest in the designs of PV system components. This prompted me to enroll in SET with a focus on Solar, Power, and Economics. I learned a lot about PV systems and the economics behind them throughout my master's program. I chose to focus my thesis work in this exciting area because I believe that it will help the end-users if PV system design is optimized.

My thesis project aimed to validate the possibility of using the solar cell self-inductance to partially design the DC/DC converter on the solar cell so that MPPT can be performed at the sub-module level. I appreciate this varied topic since it broadens my understanding of PV systems and the intricacies that go with them. Although the project's initial concept included performing experiments for model validations, this couldn't be achieved due to a big research gap and time constraints. However, I thoroughly loved learning and working with various software, which I am confident will be valuable in my future profession.

I would like to thank David van Nijen, my daily supervisor, for holding regular progress meetings and being accessible on short notice whenever I had difficulty understanding something. Apart from routinely assisting me with project work, he also took the time to assist me with my presentation and scientific writing abilities. Secondly, I would like to thank Dr. Patrizio Manganiello for sharing his expertise and opinions on the subject, hosting a lively interactive conversation, and providing a moral lift at each monthly meeting. I also want to thank everyone from the PVMD and DCE&S groups who assisted me with my thesis. I want to thank everyone from my workspace for their encouragement and assistance with my project. In addition, I would like to thank Dr. René van Swaaij and Dr. Gautham Ram Chandra Mouli for being part of my graduating committee.

Lastly, I would like to thank my family and friends for their support and encouragement throughout the duration of my thesis.

Saurabh Chakravarty
Delft, July 2023

Abstract

Photovoltaic (PV) modules have considerable difficulty when exposed to shading since even partial blockages can significantly reduce energy production. To make the PV module shade-resilience, sub-module maximum power point tracking(MPPT) can be done for each string in the module. One way of doing it is by using converters at the sub-module level, which can track the string's maximum power point(MPP) by varying its duty cycle. In conventional converter design, inductors are the bulkiest and costliest component used, which eventually makes the application of sub-module MPPT less cost-effective. However, a literature study found that solar cell generates self-impedance under biasing, which opens up the idea for cell-level integration of power electronics. This thesis aims to validate the possibility of using the self-inductance generated in the solar cell for partially designing the DC/DC converter on the solar cell such that MPPT can be performed at the sub-module level. To accomplish this objective, two distinct strategies have been examined: The utilization of solar cell self-inductance for designing a conventional boost converter on a solar cell surface and the integration of a planar coil onto a solar cell for partially designing a DC/DC boost converter.

A commercial PV module comprises a junction box that houses the DC/DC converter for sub-module MPPT. Literature studies found that under voltage biasing, a solar cell laminate generates a self-inductance of around 50 nH. This electrical property of solar cells can be exploited to partially integrate power electronics like converters onto the cell's surface, reducing the need for bulky passive components like inductors and even possibly eliminating the junction box. A conventional DC/DC boost converter is chosen because the inductor's position in the circuit makes it suitable for partial integration onto a solar cell. A conventional boost converter circuit was realized in PLECS software using MPP parameters of commercial solar cell MAXEON3 (V_{MPP} = 8.22V, I_{MPP}=6.08A, and P_{MPP}=50W). The inductor used in the converter requires a critical inductance value to make the converter operate in continuous conduction mode(CCM). This critical inductance value depends upon the converter's V_{in}, switching frequency, duty cycle, and input current ripple. For the application of sub-module MPPT, the converter was designed for a string of 13 series connected solar cells. Thus self-inductance of each cell adds up in the string. Through analytical analysis, it was found that the total self-inductance generated in the string (0.65μH) is insufficient for designing the boost converter(3.38μH) operating at 500kHz. Thus it was concluded that a conventional DC/DC boost converter could not be designed using only the solar cell self-inductance. However, if the inductance value of the solar cell is increased, it might be possible to design the conventional boost converter.

To increase the solar cell inductance, a planar coil must be added as a layer on the back of the solar cell. Adding the planar coil will increase the inductance of the solar cell. However, it will also add resistance, which will cause power losses. From literature studies and simulation results, it was found that the primary cause of AC resistance in a planar coil is skin and proximity effects. So, an optimized planar coil design is required, which can provide inductance for the converter's partial design while generating minimum AC coil resistance. Using COMSOL Multiphysics, a 3-D planar coil model with a gap in the middle was created and studied for different coil parameters. Firstly, the spacing between the coil turns is studied to minimize the AC resistance generated in the coil. It was established that by fixing the spacing parameter to 4mm, the proximity effect was dampened, and the coil had a lower resistance value, mainly due to the skin effect. Later, planar coils with high inductance values and quality factors were achieved by varying the gap size parameter. Considering higher granularity, for converters operating on strings of 5, 8, and 13 series connected solar cells, the best combination of planar coil designs is provided for each string. These combinations consist of lower quantities of coils that are suitable to generate more than the required critical inductance for the converter's design parameters. Having lower quantities of the coil for the converter design will significantly reduce the overall fabrication cost, therefore, making it cost-effective for sub-module MPPT applications.

Nomenclature

Table 1: Abbreviations used in the report

Abbreviation	Description
PV	PhotoVoltaics
FBC	Front-Back contact
MPPT	Maximum Power Point Tracking
PFC	Power-Factor Correction
AC	Alternating Current
DC	Direct Current
AM	Air Mass
IC	Integrated circuit
Q	Quality
BCM	Boundary Conduction mode
CCM	Continuous Conduction mode
DCM	Discontinuous Conduction mode
EMI	Electromagnetic interference
D	Duty-Cycle
SEPIC	Single-ended primary-inductor converter
ZVS	Zero-voltage switching
ZCS	Zero-current switching
IED	Infinite-Element Domain
M.F.	Magnetic Field

Contents

List of Figures

List of Tables

1

Introduction

This chapter will begin by providing a glance at the project's purpose. Later in the chapter, the methodology of the project will be explained, and by the end of the chapter, the main research question of the project will be put forward. Several pieces of information in this chapter will be explained in the later chapters.

1.1. Energy- Demand & Supply

The world's energy consumption has skyrocketed due to the expanding human population and the advent of new technologies. Figure 1.1 depicts the primary energy consumption (including both non-renewable and renewable energy) of various nations based on data obtained by University of Oxford scientists [1]. From fig 1.1, it can be observed that countries with large populations are significant consumers of energy. High energy consumption is necessary for the economic development of these nations [24]. Economically growing countries have begun industrialization in the past one or two decades, resulting in a significant energy demand to improve output. As a result, it is more important than ever to meet the expanding population's energy needs.

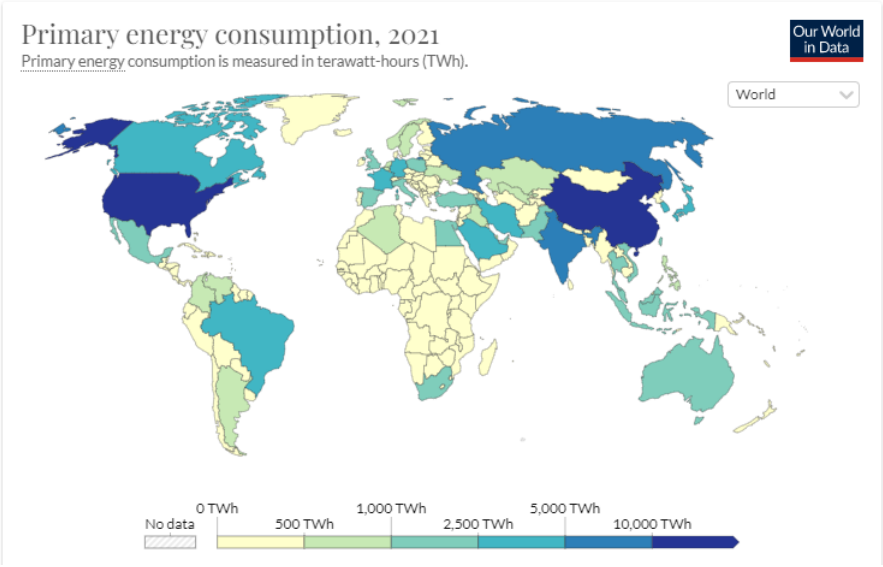

Figure 1.1: World Energy Consumption Data[1]

Figure 1.2 depicts the energy consumed from various sources. Fossil fuels such as coal and oil are the leading contributors to global energy generation. However, electricity produced from the combustion of fossil fuels is a major contributor to air pollution and climate change. The critical major greenhouse gases - carbon dioxide and methane- are emitted into the atmosphere annually through burning fossil

fuels for energy [25]. This led to an increase in the earth's average surface temperature by 1.1°C [26]. So, it is crucial to seek an Eco-friendly energy source that may stop environmental exploitation and limit the rising levels of the earth's temperature. Several green energy sources are available to humankind, including solar, wind, hydro, and thermal energy.

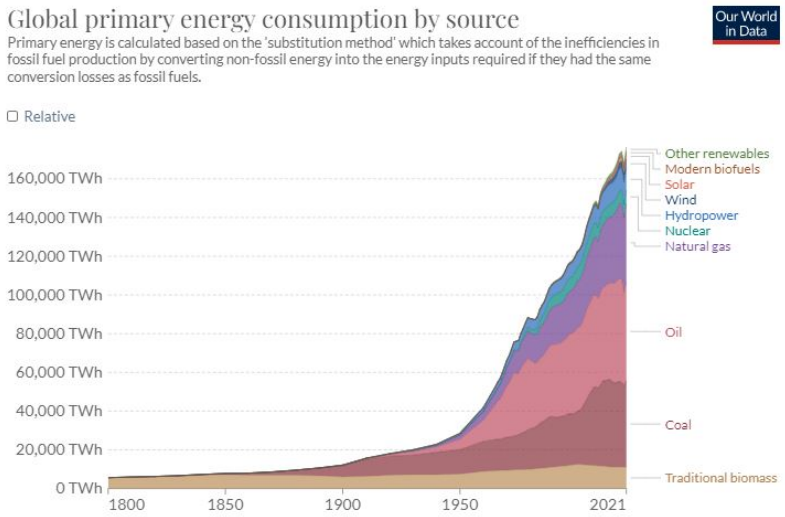

Figure 1.2: Various Energy source consumption to fulfill global energy demand[1]

1.2. Solar Energy

Solar energy is the most plentiful renewable source of all the available options. Solar energy can potentially supply the world's energy needs in a sustainable and high-quality manner[27]. On average, the annual global radiation that reaches the earth's surface is about 1600-2200kWh/m^2[28]. This energy can be transformed into electricity using solar cells, made of semiconductors, and can convert the photons into electricity, which can be stored in batteries for further uses in various other occupations [2].

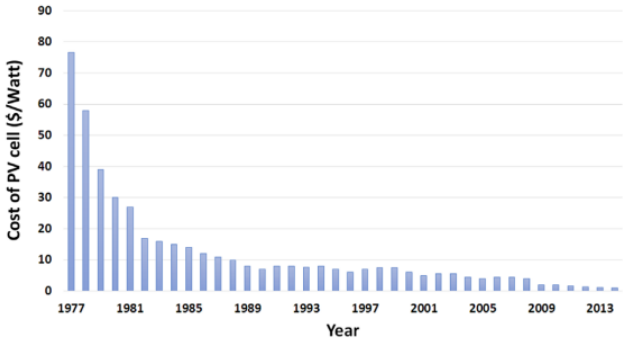

Figure 1.3: History of PV cost [2]

With an increasing focus on renewable energy sources and a global trend towards greener and more sustainable power generation, solar energy-based applications attract attention to replace fossil fuel energy. One of the most significant trends in the solar PV sector is the dramatic drop in the cost of solar photovoltaic modules by almost 99 percent over the last 36 years (figure 1.3). Government regulations that encouraged global PV market growth and innovations in PV technology, including improvements in conversion efficiency, were responsible for the decline in PV prices. This decreasing trend of solar costs has made it more accessible and economically viable for consumers [29].

Photovoltaic technology involves the direct conversion of solar radiation into electricity. The intensity of incident radiation determines the amount of power that can be generated by solar cells. Figure 1.4 represents a typical solar cell containing metal fingers and busbars for the collection. PV modules

consist of solar cells connected in series or parallel depending upon the output voltage or current requirement (figure 1.4). PV arrays (fig1.4) are designed by connecting the modules in series and parallel combinations depending on the load. These arrays are then placed on mounts which can be rotated vertically or horizontally to set module angle and azimuth for maximum power generation.

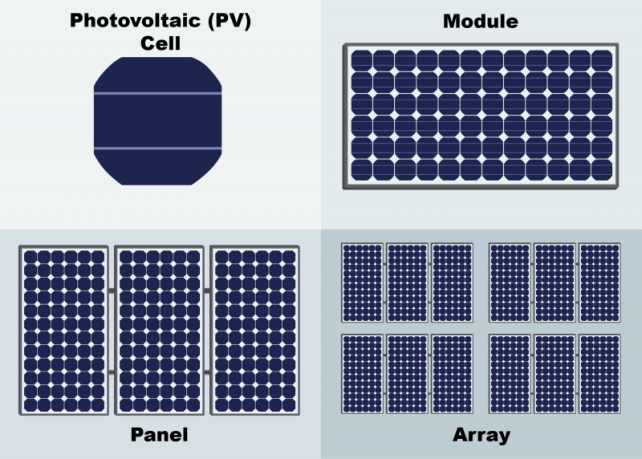

Figure 1.4: PV cell, PV Module, PV Panel, and PV array [3]

Photovoltaic energy conversion uses devices based on electronic semiconductors, mainly but not exclusively, crystalline silicon (c-Si). The majority of commercial solar cells are made from c-Si. In 2020, over 125GW of c-Si were installed, which is 95% of the overall PV market [30]. The most commercially used solar cell is a front-back contact (FBC) solar cell, which contains metal fingers for charge carriers at both sides of the cell, front and back. In interdigitated back contact cells (IBC), metal finger contacts are accumulated at the cell's back side to avoid shading losses at the front. Although IBC cells have higher efficiency than FBC cells due to their high design complexity, FBC cells are preferred more in the PV industry [31]. Both types of structures are presented in figure 1.5.

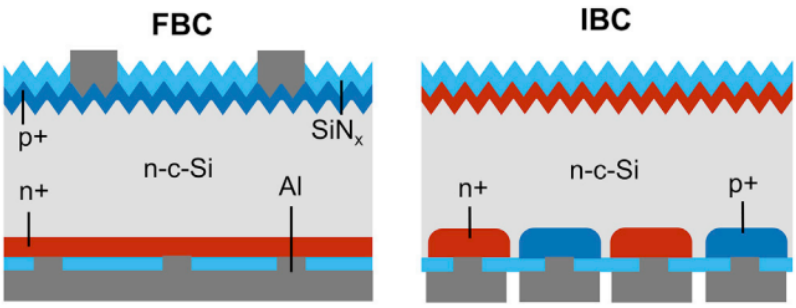

Figure 1.5: c-Si PV cell structure of FBC(left) and IBC(right)[4]

1.3. Photovoltaic Systems

Photovoltaic(PV) Systems are composed of multiple solar modules combined with other electrical hardware(Balance of systems/BoS), which uses the Sun irradiance energy to generate electricity. The BoS consists mainly of inverters, DC-DC converters, charge controllers, and batteries. The power converters are essential as they perform Maximum power point tracking (MPPT) on the module, perform power conversions like DC-DC and DC-AC, and control the battery charge. Based on the position of the converter in the PV system, different DC/AC conversion topologies for photovoltaic applications are showcased in Figure1.6. Based on the type of load usage, PV systems are classified as stand-alone, grid-connected, or hybrid systems. In a grid-connected system, the load relies on power from the grid and solar. The PV system is connected to the grid using an inverter, which converts the PV DC power into AC. During high solar irradiance, power generated from the PV is directly fed into the grid or to AC

loads. The grid operates in an AC system at a fixed voltage and frequency. Thus, it becomes necessary to use an inverter to convert DC from PV to AC for the grid and a converter to match the grid's voltage. This type of PV system uses a three-phase inverter to handle high-power transmission. In a stand-alone system, the loads present rely only on solar power. As a result, a battery is necessary for energy storage when there is little or no solar irradiation. The battery also has a charge controller, which disconnects the battery from the modules when it is completely charged or disconnects the battery from the load when drained below a certain threshold. A hybrid PV system combines the PV modules with a secondary power generator like diesel, gas, or wind. The secondary power generator provides power to load or charge the battery during lower irradiance. The PV system must generate the most energy possible to meet the grid's demand; thus, the inverters must be highly efficient.

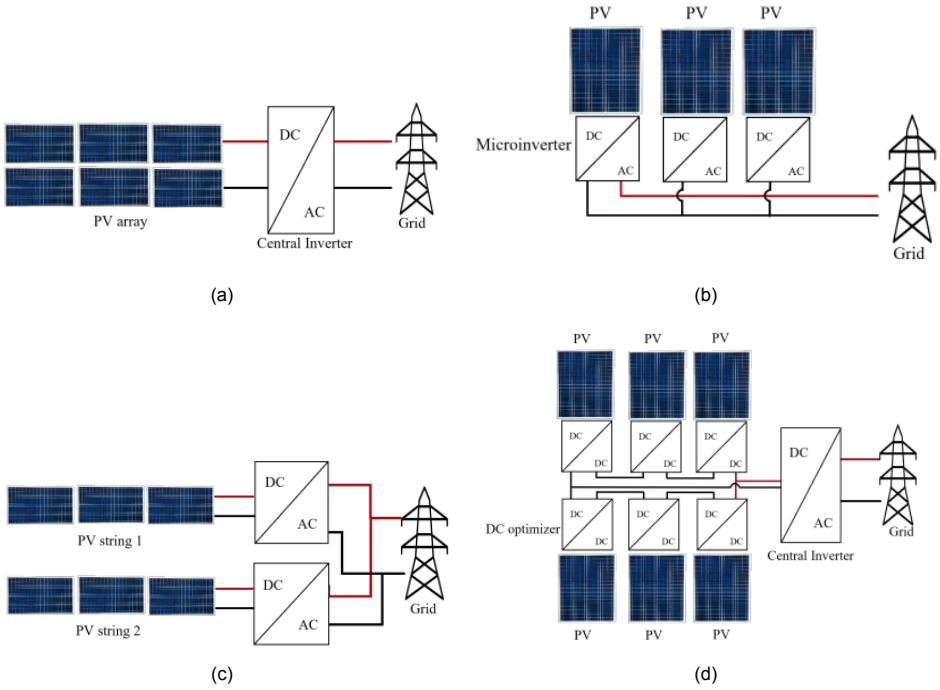

Figure 1.6: DC/AC topologies for PV application[5]: (a) Central Inverter (b)Microinverter (c) String inverter (d) Central Inverter with multiple optimizers

Different inverter topologies are designed for different PV system applications. Figure 1.6 shows different topologies. These topologies also determine the granularity of MPPT in the PV system. The central inverter is a common inverter option. Figure 1.6a depicts a central inverter configuration with only one inverter for all PV modules. The interconnection of modules (series/parallel combination) determines the inverter size. Using only one inverter in the PV system limits the potential of MPPT, causing high losses during module-level shading. MPPT must be performed at one or several modules rather than an array to reduce this power loss.

To diminish current-mismatch losses, the optimal way to track the maximum power point and perform power conversion at the module level is by using a micro-inverter configuration as shown in figure 1.6b. This configuration is assumed to have the highest efficiency as each module's maximum power tracking is done individually [5]. Another advantage of using this configuration is it prevents any failure occurring at the module level to affect the whole PV array's performance. However, due to its direct placement in the PV module, the inverter has to bear harsh conditions like high temperatures. Another disadvantage is the efficiency of the topology drops when required to convert the module's DC voltage to large output AC voltage.

A string inverter is an adaptation of a combined central and micro inverter, where each string of PV modules in an array is equipped with a DC/AC inverter (figure 1.6c). This configuration of the inverter can perform MPPT for each PV string independently. Hence, it is more efficient in tackling the shading issue than the central inverter. However, due to the current mismatch, there is still the risk of hot spots, which can damage the PV module in the long run [11].

DC/DC optimizers offer a unique power-tracking solution during shading conditions. Every PV module has a DC/DC converter that tracks the MPP. The output of each converter is directed to a single DC/AC central inverter. This inverter only operates for a limited range of input DC voltage. Varying the converter's duty cycle, the inverter's input voltage is within the acceptable range[11].

Module-level shading is a critical issue to deal with while designing a PV system. Central inverters are not optimal when considering the shading issues, as MPPT is done for an array. While micro-inverter and strings inverters are considered a better option for tracking MPP with higher granularity, leading to a higher energy yield during partial shading conditions. However, these inverters use power electronics like capacitors, inductors, and switches, making the junction box more bulky and costly.

1.4. Sub-Module level Partial Shading

Partial shading or non-uniform irradiance incident on a panel can cause significant power losses. Due to lower irradiance incident upon a solar cell, the cell current decreases (figure 1.7). A PV panel consisting series of connected cells, due to a lowered current of a single cell, affects the whole panel's performance. The more shading occurs, the larger the panel's power loss percentage [32].

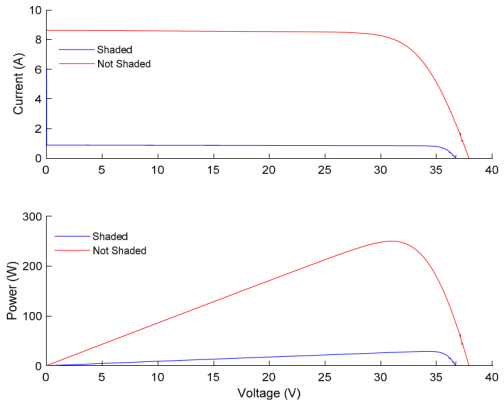

Figure 1.7: Decrease in cell current and power due to shading[6]

Shading can occur from surrounding objects like trees, buildings, leaves on the panel, or even another PV array mounted around it. These shadings have significant consequences on the output of the module:

- electrical mismatch
- uneven power-generation
- overheating of a shaded cell resulting in hotspot effect and degrading the cell lifetime
- damages on the module

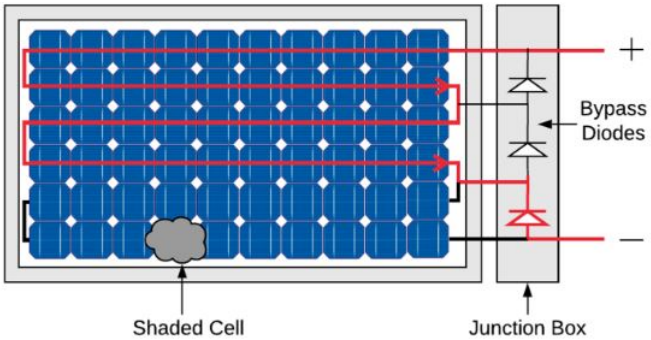

Figure 1.8: Standard PV module with bypass diode and picture presentation of shading[6]

A bypass diode is the most common way to mitigate the effects of module-level partial shading. The commercial PV modules are equipped with bypass diodes, as shown in figure 1.8. The bypass diode is necessary for integration in real-life conditions where shading on the module is a significant concern. As can be seen in the referenced figure 1.8, a bypass diode is incorporated in parallel with a series-connected set of solar cells. The bypass diode is engaged when a current mismatch occurs between the strings due to shading on some of the cells. Without a current imbalance in the string, the bypass diode will be in its ”off” position, preventing electricity from passing through it. The issue with using a bypass diode is the generation of multiple peaks in the P-V curve of the module (figure 1.9) under shading conditions [33]. This distorts the operation of the MPP tracker, as it gets difficult for the algorithm to find the global maxima on the P-V curve, leading to lower power generation (not at MPP values)[7].

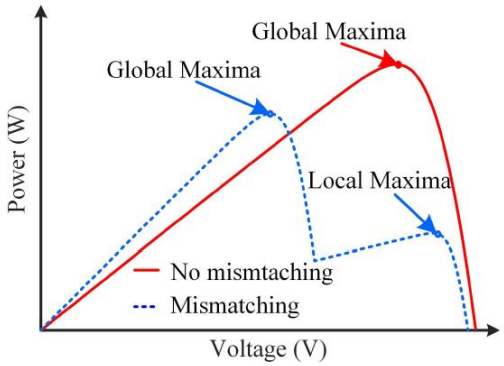

Figure 1.9: Multiple peaks in P-V curve due to activation of bypass diode [7]

There are many other methods for mitigating partial shading that do not use bypass diodes. Das et al., [34] discussed many different shading mitigation techniques in their review paper. The techniques are classified based on granularity, passive components, efficiency, and accuracy. Methods like the Equalization scheme (voltage and current) showed high efficiency and accuracy but with limited granularity and also used many passive Components. Other power-electronic-based techniques like switched capacitors or inductors are complicated in operation but are more effective as they restrict the formation of local maxima [7].

1.5. Proposed Idea - Utilizing solar cell impedance

Many shading mitigation methods proposed in [6], [7], and [34] use power converters for the application of MPPT. The converter is equipped with an inductor, which is the bulkiest and possibly costliest component used in the circuit. Thus to make the application of sub-module MPPT using a converter cost-effective, a new concept has been proposed that exploits the application of solar cell self-impedance.

1.5.1. Solar cell impedance

Nijen et al., [35] explained the capacitive and inductive nature of a modern c-Si PV cell. To understand the inductive behavior, they measured the impedance of PV cells with different cell structures and sizes. Finally, they found that a single-cell laminate generates inductance in the range of 63 to 130 nH (schematically explained in figure 1.10 using a one-diode model). Interestingly, they also found that the inductance generated in the solar cell is affected by mainly two factors: the number of bus bars (metal contacts) available in the solar cell area and the shape of the metal contacts.

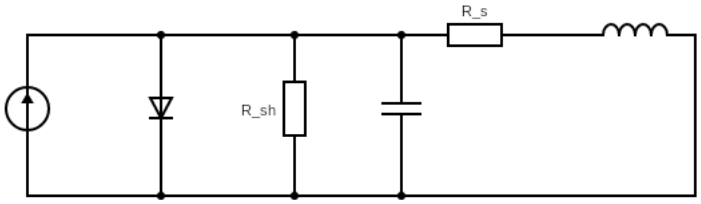

Figure 1.10: One-Diode equivalent solar model

1.5.2. Converter

A converter plays an essential part in BoS for signal alteration and tracking maximum power points. As the inverter requires a constant input voltage, having it directly connected to the PV module might not allow the PV module to operate at MPP, thus reducing the energy yield of the system. Therefore, a DC/DC converter is used between the PV module and the inverter. Varying the converter's duty cycle, the PV module is operated at MPP while not altering the inverter's input voltage. Three commonly used converters are buck, boost, and buck-boost converters. Figure 1.11 presents a conventional boost converter topology, which can be used for MPPT and stepping up the voltage.

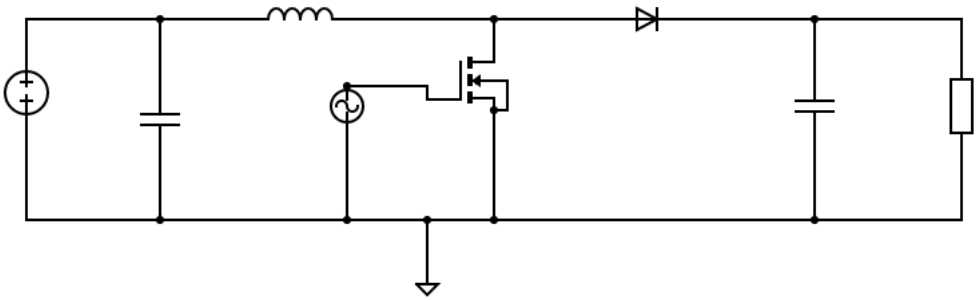

Figure 1.11: Conventional Boost Circuit [8]

1.5.3. Combined circuit design

Utilizing the solar cell's self-impedance for designing the converter can reduce the size and cost of the converter. Integrating the passive components with the design of c-si solar cells opens up new, optimally efficient ways of designing PV modules [4]. A DC-DC boost converter uses an inductor and capacitor at the front to filter out the ripples from the input signal. Figure 1.12 shows that the position of the inductor and capacitor in the boost converter is identical to the solar cell one-diode equivalent model (red-dotted region), making it possible to integrate the two.

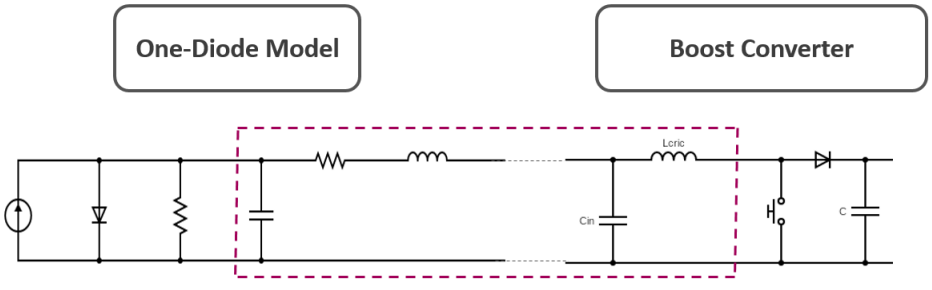

Figure 1.12: Proposed Combined Circuit- Solar cell one diode equivalent model & Boost Converter: The red dotted region shows the similarity of the impedance on both

1.6. Research Question & Thesis Outline

This thesis project aims to research the feasibility of partially integrating a DC/DC converter on a c-Si solar cell. Therefore, the main research question is:

How can the self-inductance of the solar cell support the topology of a DC-DC converter such that MPPT can be performed at the sub-module level?

To give a response to the main research question, a few sub-question have been formulated whose answers will be able to justify the answer for the main research question.

1. Which type of DC-DC converter can incorporate solar cell self-inductance?
2. Which type of planar coil design can match the impedance requirement of a DC-DC converter
3. How can integrating a planar inductor onto a solar cell support a DC-DC converter topology to achieve maximum power point tracking at the sub-module level?

With the introduction to the subject given, the chapters are ordered as follows. Theoretical background regarding the PV technology, DC/DC converter, Inductor, and several loss mechanisms in inductors are discussed in Chapter 2. In Chapter 3, simulation methods are described for modeling DC/DC converter and planar coils. In Chapter 4, the simulation results of the DC/DC converter and planar coil design are discussed. In Chapter 5, discussions are made regarding different choices of planar coil desing suitable for partial integration onto the solar cell. The report is completed with Chapter 6 by discussing the conclusion of the thesis work and the scope of further research work.

2

Theoretical Background

This chapter discusses some theoretical background about topics related to this thesis project. Although it is not cited in every instance, the majority of the information in this chapter comes from the Solar Energy Book written by Smets et al.,[11]. The chapter begins with section 2.1, discussing solar energy and its importance. Section 2.2 covers the basic principle behind the working of the solar cells. Section 2.3 gives a brief description of MPPT. In section 2.4, different topologies of DC-DC converters are discussed. Section 2.5 provides some information regarding inductors. At last, the chapter ends with section 2.6, where different types of loss mechanisms are presented.

2.1. Solar Energy

Capturing solar energy using PV panels to generate electricity is considered a promising market in the renewable sector [36]. The sun, the nearest star to The Earth, is the main source of energy packets known as photons of different wavelengths. These photon's energy is determined by their wavelength and can be calculated by:

$$E_{ph} = \frac{h \times c}{\lambda} \tag{2.1}$$

Where *h* is Planck's constant and c is the speed of light

A solar cell can absorb Photons with appropriate energy to generate electricity. Therefore, it is important to understand the spectral distribution of solar radiation (the number of photons of certain energy as a function of the wavelength). Figure 2.1 shows solar spectra of different radiations. Since the irradiance from the sun gets scattered in the atmosphere before reaching the Earth's surface, the number of photons reaching the surface is not equal everywhere across the surface of the Earth. Therefore, it is important to define conditions for comparing different solar cells and modules. Standard test condition (STC) is an industry-wide criterion for determining the efficiency of PV modules. It uses the AM1.5 spectrum as a reference where the solar irradiance incident on the sun-facing plane on a surface tilt of 37° to the horizontal. The total irradiance at STC is 1000W/m^2 with a cell temperature of 25° [11]. Figure 2.1 shows the spectral irradiance of AM) which represents the spectrum outside the earth's atmosphere, and AM1.5. The irradiance of AM0 is 1361W/m^2.

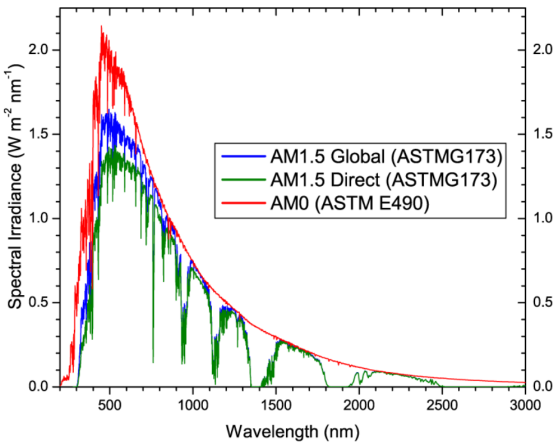

Figure 2.1: Spectral Irradiance of different solar spectrum[9]

2.2. Working principle of solar cell

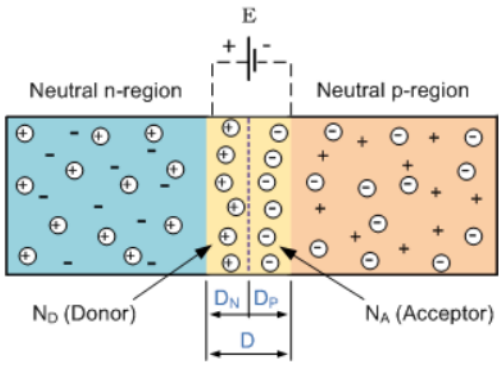

Figure 2.2: n-p junction of a solar cell

The working principle of a solar cell is based on the photovoltaic effect, which is the formation of potential differences at a junction of two different materials in response to electromagnetic radiation(photons). PN homojunction is found in various crystalline silicon solar cell architectures. The p-type material is doped with impurities like boron, aluminum, gallium, etc, which are acceptor ions. At the same time, the n-type is created by doping impurities like Phosphorous, which are donor atoms. Other types of junctions are heterojunctions made of two different materials and metal-semiconductor junctions. Figure 2.2 shows an n-p junction of c-Si. When the junction is illuminated, a photon with sufficiently high energy can excite an electron from the valence band to the conduction band, thus resulting in the generation of free electrons in the conduction band and a hole in the valence band. Only photons with energy more than the bandgap energy of the material result in the generation of electron-hole pairs in the semiconductor material. The energy of the photons is given by the equation 2.1, which shows that it is wavelength dependent. Hence not all the photons can generate charge carriers. The electric field in the depletion region of the pn junction separates the charge carriers. These charge carriers are then collected at the electrical contacts and used in the external circuits. [11]

Solar cell performance is characterized by parameters like maximum power (P_{max}), the short circuit current (I_{sc}), open circuit voltage (V_{oc}), and fill factor (FF).

Short circuit current
The short circuit current density is the current which flows through the solar cell when the voltage across the solar cell is zero. For an ideal solar cell with moderate resistive losses, the short circuit current is

almost equal to the photogenerated current. Hence in the commercial PV module, the datasheet of the manual mentions the short circuit current, which is the maximum current generated in the module at STC. The short circuit current depends upon the photon flux incident on the cell and the area of the solar cell. Thus, the short circuit current density(J_{sc}) is often used to avoid area dependency. In the STC spectrum, a crystalline solar cell delivers a maximum possible current density of 46mA/cm^2, while commercially available solar cells have a current density of around 35mA/cm^2.[11]

Open Circuit voltage
Open circuit voltage is the maximum voltage from a solar cell when no current flows through the external circuit. Open circuit voltage resembles forward bias voltage, during which the cell's dark current density compensates for the photocurrent density. The equation measures V_{oc} of a solar cell. The equations 2.2 show the dependence of V_{oc} on saturation current density(J_o). J_o depends on the recombination of charge carriers in the cell; hence V_{oc} is a good measure of the amount of recombination in a solar cell. Commercially available solar cells have V_{oc} of 600mV while in AM1.5 conditions, the laboratory c-Si have V_{oc} is up to 720mV.[11]

$$V_{\mathrm{oc}} = \frac{k_{\mathrm{B}}T}{q} \ln\left(\frac{J_{\mathrm{ph}}}{J_0} + 1\right) \approx \frac{k_{\mathrm{B}}T}{q} \ln\left(\frac{J_{\mathrm{ph}}}{J_0}\right) \tag{2.2}$$

Here,

- k_B is Boltzmann constant
- T is temperature, q is the charge
- J_{ph} is photocurrent density due to the flux of photogenerated charge carriers
- J_o dark current density/saturation current

Fill Factor
During the operating point of V_{oc} and J_{sc}, the power produced by the solar cell is zero. The fill factor is a measure to determine the maximum power generated by the solar cell in conjunction with V_{oc} and J_{sc}. It is the ratio of the maximum power of the cell at MPP ($P_{\mathrm{max}} = V_{\mathrm{mpp}} \times J_{\mathrm{mpp}}$) and product of V_{oc} and J_{sc}. Equation 2.3 represents the fill factor.

$$FF = \frac{J_{\mathrm{mpp}} V_{\mathrm{mpp}}}{J_{\mathrm{sc}} V_{oc}} \tag{2.3}$$

Lastly, the cell conversion efficiency is calculated under the STC conditions. Equation 2.4 represents the conversion efficiency. Commercially available ci-solar cells have FF in the range of 0.75-0.80 with a conversion efficiency of 22-26%

$$\eta = \frac{P_{\mathrm{max}}}{I_{\mathrm{in}}} = \frac{J_{\mathrm{MPP}} V_{\mathrm{MPP}}}{I_{\mathrm{in}}} = \frac{J_{\mathrm{sc}} V_{\mathrm{oc}} FF}{I_{\mathrm{in}}} \tag{2.4}$$

2.3. Maximum Power point Tracking(MPPT)

MPPT plays an important role in PV systems by increasing the energy yield of PV modules. Figure 2.3 shows the I-V curve of an illuminated solar cell. The shape of the I-V curve remains the same even though inter-connecting the cell in series or parallel combinations increases the overall voltage and/or current. To explain the functionality of MPPT, the I-V curve of only one solar cell is shown in Figure 2.3.

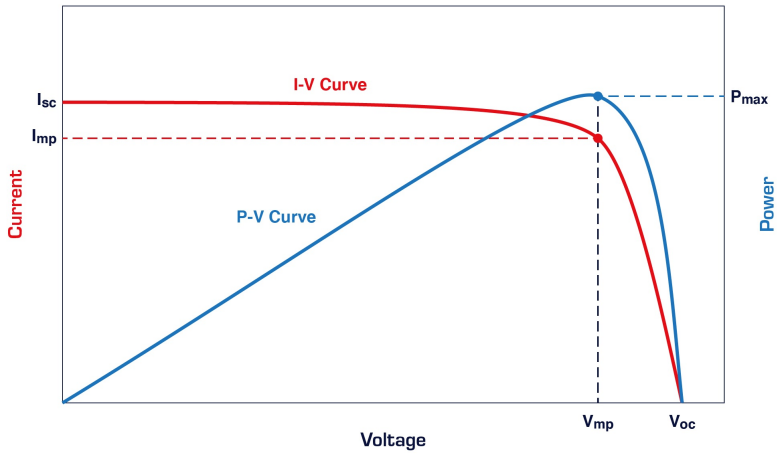

Figure 2.3: I-V & P-V curve [10]

The I-V curve of a solar cell depends on factors like temperature and irradiance. Figure 2.4 shows the variation of current and voltage for changing irradiance and the module's temperature. Increasing the irradiance results in increased current and voltage, while increasing the temperature results in increased current but a drop in voltage value.

The operating point is the point of the I-V, which labels the current and voltage value at which the PV module is being operated at a given time. Transforming the I-V curve into a P-V curve is shown in Figure 2.3. To generate the maximum output power at a given irradiance and temperature, the operating point resembles the maximum of the P-V curve. This maximum point is known as the maximum power point (MPP).

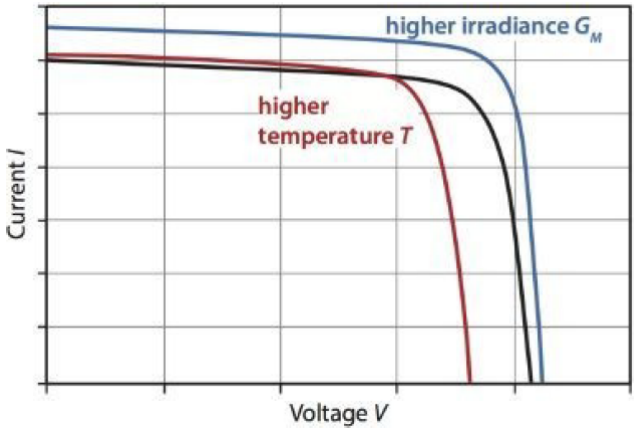

Figure 2.4: Effect of varying temperature and irradiance on I-V curve [11]

To extract maximum power out of the PV module, it is important to force the module to operate at MPP. However, the MPP on the I-V and P-V curves may shift due to the effects of irradiance and temperature on the module's current and voltage values. Therefore, it is important to track the changes in the P-V curve such that in any instance (irradiance and temperature), the operating points can be adjusted to be at MPP. This method of tracking the changes is known as maximum power point tracking (MPPT). MPPT is not a component itself but rather an algorithm present in a converter or charge controller. MPPT can be done using a hard-coded algorithm or changing the duty cycle of the switch such that any variation in input voltage can be regulated to give a stable constant output. Research papers ([37],[38] and [39]) have shown the Pertub & observe (P&O) algorithm and Incremental conductance method where the output voltage is feedback using a closed loop and then a transfer function is used to increase or decrease the duty cycle of the switch accordingly.

2.4. DC-DC Converters

Due to uncertainty in the irradiance level, the output voltage of the photovoltaic system is variable. Thus, to keep a constant and regulated DC voltage, DC-DC power converters are employed to execute that job.

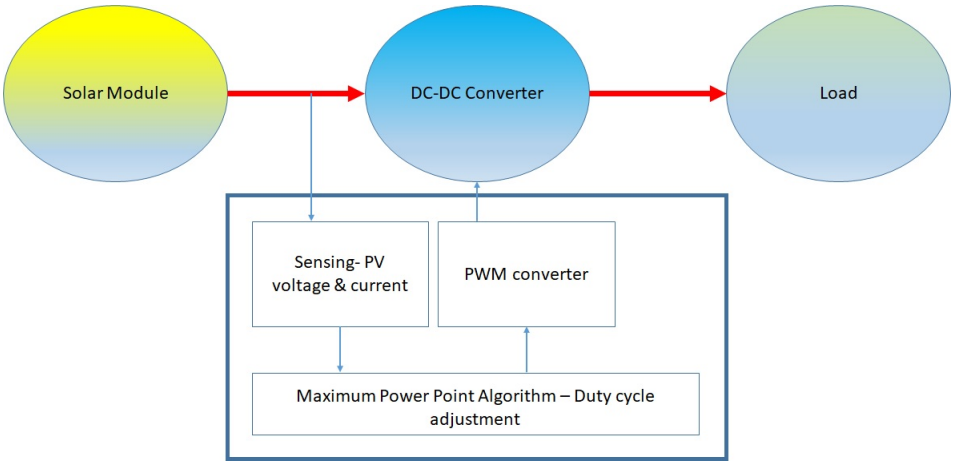

Figure 2.5: Schemtaic of PV system

The DC-DC converter technique was introduced in the 1920s, and since then, research has been going on to make the conversion task more efficient and smooth [40]. It is predominant in power engineering, mainly in industrial applications, hardware circuits, and especially in renewable power generation. Many DC-DC converter topologies are being used to modulate the voltage according to the application. Figure 2.5 shows a simple schematic of the PV system where a DC/DC converter is used to extract maximum power out of the module by regulating the solar module's voltage using MPPT.

Converters are mainly classified into two types; isolated DC-DC converters and non-isolated DC-DC converters. In an isolated DC-DC converter, the input and output part of the converter is isolated by an electrical barrier using a high-frequency transformer. This makes the circuit complex and high cost. Compared to isolated converters, non-isolated converters have a simple circuit design and low cost. This thesis report will mainly focus on the performance analysis of non-isolated DC-DC converters- Boost, CUk, and SEPIC.

2.4.1. Boost Converter

A conventional boost converter plays a vital role in renewable energy systems by stepping up an unregulated DC voltage to a higher constant DC output. A careful design of a boost converter is concerned with its output power and operational efficiency. Renewable energy technology like PV technology needs a DC/DC converter as a way of power transmission to perform energy injection to loads and batteries. Power converters are built from a combination of four components: an inductor, switch, diode, and capacitor. Figure 1.11 shows a conventional boost converter topology. The power transmission (absorption from cell and injection to load) is done through switching cycles. The ratio between the ON and OFF time during one period controls the output voltage. The switch used in a boost converter is controlled using a gate driving circuit. In a conventional boost converter, pulse width modulation (PWM) switching is used. At a constant frequency, the PWM generates a square wave of the ON and OFF period. Now, the duty cycle of a switch, D defined as the ratio of ON duration to the entire switching period, is used to regulate the ratio between input and output voltage. The boost converter operation happens in three different modes, boundary conduction mode(BCM), continuous conduction mode(CCM), and discontinuous conduction mode(DCM), depending upon the relative length of the switching period [8]. Another way of defining the operation of a boost converter is by the size of the inductor used. Critical inductance(L_{cric}) is the value of inductance the circuit requires to operate in boundary conduction mode. Equation2.5 shows the critical inductance and how the switching frequency has a significant influence

over it [8].

$$L_{\text{circ}} = \frac{V_{\text{in}} * D}{\Delta I_{\text{L}} * f_{\text{sw}}} \tag{2.5}$$

here;

- V_{in}: input voltage to the boost converter
- D: duty cycle of the switch
- ΔI_L: current ripple in the inductor
- F_{sw}: switching frequency of the switch

Table 2.1 shows how the inductance value of an inductor(L) with respect to critical inductance value(L_{circ}) has an influence on the operation of the boost converter.

Table 2.1: Boost Converter Mode of Operation

Condition	Mode of Operation
$L > L_{cric}$	CCM
$L = L_{cric}$	BCM
$L < L_{cric}$	DCM

Boundary Conduction Mode
In boundary conduction operation mode, the switching device is turned ON when the voltage across it is zero and turned OFF when the current in the switch reaches zero (figure 2.6). This leads to a continuous current flow in the inductor and a power transfer with fewer losses. This switching feature of the converter at BCM makes it a good choice for zero-voltage/current switching, which is discussed in detail in appendix **??**. Converter operating at BCM requires a much simple control scheme. However, the main disadvantage of BCM is the increased inductor current ripple. From table 2.1, it can be observed that the inductance value for BCM is much lower than CCM, thus allowing higher current ripple for which a much more complex filter is required [41].

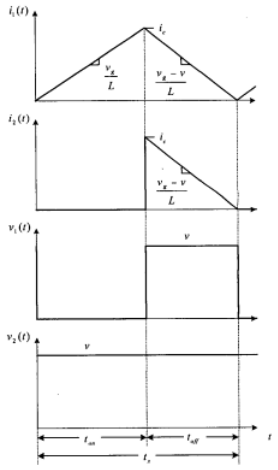

Figure 2.6: Boost converter operation in Boundary conduction mode[12]

Continuous Conduction Mode
Continuous conduction mode is the mode of operation in which the energy stored in the coil during the ON period of the switch never drops to zero. Also, the current in the inductor will never cross zero. In CCM mode, the output voltage depends on the PWM duty cycle (D). In simple terms, in the CCM mode control strategy, it is simple to adjust the duty cycle to compensate for the variation in the input voltage.

Also, based on the table 2.1, the inductor size chosen is relatively large, leading to fewer current ripples in the circuit. CCM mode is the optimal option for designing a real system that requires precise control over the output, as only one factor (the duty cycle) is required to regulate the output voltage.[42]

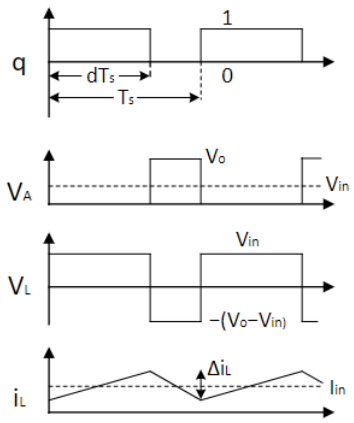

Figure 2.7: Boost converter operation in Continuous conduction mode[13]

Figure 2.7 shows current(i_L) and voltage(V_L) waveforms of an inductor used in Boost converter under CCM operation. During the switch (Q) ON period (dT_s), the inductor current is more significant than zero and increases linearly with a voltage across. During the switch OFF period, the current decreases until the switch is turned back ON again, and the voltage across the inductor is $V_{in} - V_{out}$.

As the average inductor voltage for one complete period is zero (this will be explained in more detail later on), we can say;

$$V_{in} * t_{on} + (V_{in} - V_{out}) * t_{off} = 0 \tag{2.6}$$

Here;

- V_{in} : input voltage to the boost converter
- V_{out} : output voltage from the boost converter
- t_{on} : ON period of the switch
- t_{off} : OFF period of the switch

Dividing both sides by the time period of one complete cycle (T_s) and rearranging items, we get the duty cycle;

$$D = \frac{V_{out} - V_{in}}{V_{out}} = \frac{t_{on}}{T_s} \tag{2.7}$$

Discontinuous conduction Mode

From table 2.1, we can observe that when the choice of inductor size is lower than the critical inductance value, the switching ripple in the inductor current or capacitor voltage is big enough, such that the current is not flowing continuously anymore. There is a time interval during which the current in the inductor goes zero even before the switch is turned ON.

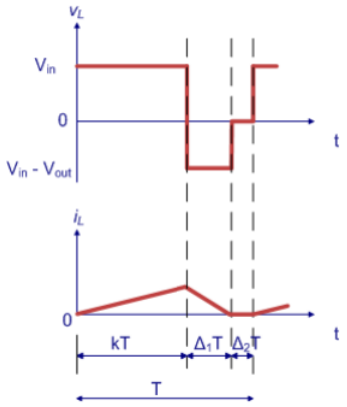

Figure 2.8: Boost converter operation in Continuous conduction mode[14]

Figure 2.8 shows the waveform of current and voltage of an inductor used in a boost converter operating under DCM operation Δ is the time period in which the current is zero before the switch turns ON. The volt-second balance equation of DCM is given as[14];

$$V_{\text{in}} * t_{\text{on}} + (V_{\text{in}} - V_{\text{out}}) * T_{\text{s}} * \Delta = 0 \tag{2.8}$$

rearraing the above eqation gives the duty cycle(D) in DCM operation [14];

$$D = \Delta * \frac{V_{\text{out}} - V_{\text{in}}}{V_{\text{in}}} \tag{2.9}$$

Inductor present in the converter stores energy in proportion to the square of the current flowing through it. To keep a uniform power throughout the converter, the inductor currents need to be higher in DCM than in CCM. This causes losses in the circuit operating under DCM. As the inductor does not fully releases the stored energy at the output in DCM, it creates a ringing effect at the output leading to noise in the circuit [43].

2.4.2. SEPIC Converter

SEPIC converter stands for single-ended primary-inductor converter. It is another type of DC-DC converter that permits to convert of a large range of DC input voltage into a stable output voltage. Its advantage over a conventional buck-boost converter is the same input/output voltage polarity, higher efficiency, and a capacitor that isolates both sides from each other during failure/cascading events.

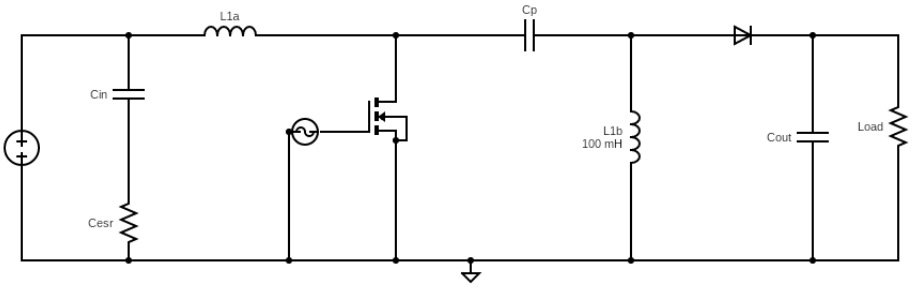

Figure 2.9: SEPIC converter design[15]

A typical SEPIC converter is shown in figure 2.9. The circuit contains two inductors, two capacitors, one MOSFET switch, and an uncontrolled switch which will be turned ON or OFF based on the voltage across it. Figure 2.10 shows the operation of the SEPIC converter in CCM mode.

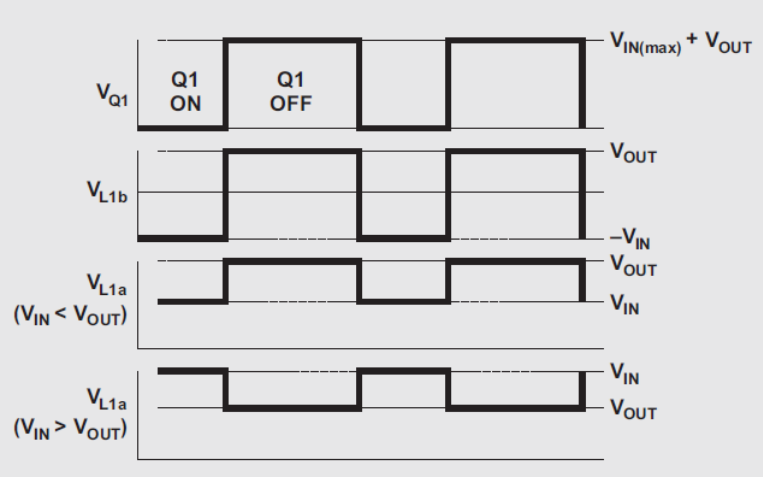

Figure 2.10: SEPIC converter under CCM operation[15]

It is vital to analyze the circuit at DC to understand the voltage at different circuit nodes. When Q1 is OFF, the voltage across L_{1b} is V_{out}. AS C_{in} is charged till V_{in}, the voltage across switch Q1 is $V_{in}+V_{out}$, which makes the voltage across L_{1b} V_{out}. When Q1 is turned ON, capacitor C_p gets charged to V_{in}. Now C_p and L_{1b} are in parallel, thus the voltage across L_{1b} is $-V_{in}$. The observation of current flow in different components in the circuit is shown in the figure. When the switch is ON, energy is stored in L1 by the input signal, and energy is stored in L_{1b} by the capacitor C_p. When the switch is OFF, current in L_{1a} now flows through C_p, Diode D, and C_{out} to the load. During this time, C_{out} and C_p get charged to supply current during the switch OFF period. More information regarding the duty cycle can be found in [44].

2.4.3. CUK converter

CUK converter is another PFC converter used to step up or down the input voltage to the desired required value. It is a special type of converter where the output voltage is of opposite polarity with respect to the input voltage. Capacitor C_{CUK} acts as the primary energy storage element, transferring energy from the input side to the output. The advantage of a CUK converter is that the input current and the output current are ripple free.[45]

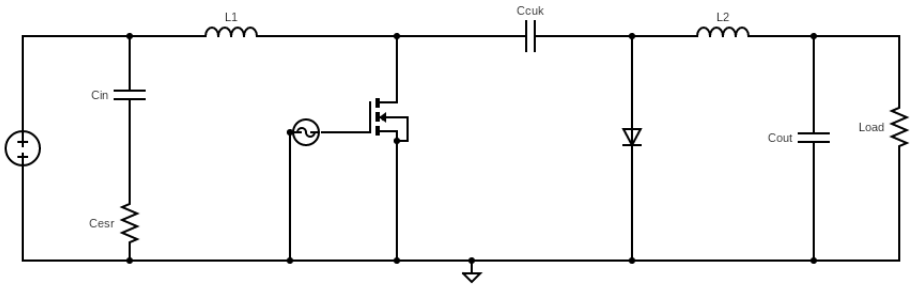

Figure 2.11: CUK converter design[16]

Figure 2.11 shows a conventional CUK converter with the same number of elements as the SEPIC converter. The only difference with the SEPIC converter is the position of the diode and inductor are interchanged. Using an inductor at both the input and output sides helps in reducing the input and output current ripple.
During the switch ON period, the diode is open, and the inductor L_1 is charged by the input source while the inductor L_2 is charged by capacitor C_{CUK}. the output current is provided by L_2. In the next cycle, the switch is turned OFF, L_1 discharges across C_{CUK} and charges it. while L_2 discharges through the

Load. Using Voltage-second balance rule [16]:

$$V_{\text{OUT}} = -V_{\text{IN}} * \frac{D}{1-D} \tag{2.10}$$

2.4.4. Switching losses in Converters

Switches are an integral part of a converter as it determines the amount of power transferred at the converter's output. Based on power transmission, there are two types of DC-DC converters, a linear converter, and a switched converter. As the name suggests, a linear converter uses resistive components to regulate the output. A switching converter known as an SMPS (switch mode power supply) regulates the converter's output by dynamically changing its ON and OFF time period. Duty cycle is a term associated with switches and means the switch on the time period in its complete switching cycle. The conventional DC-DC converter operates under a hard-switching technique where a PWM wave signal is used as a gate driver for the switch. Whenever the PWM wave signal is higher than the threshold voltage of the gate driver, the switch is turned ON, and when the PWM wave signal is lower than the threshold voltage of the gate, the switch turns OFF. Ideally, the behavior of the switching cycle should be identical to the waveform of the PWM generator. Still, the semiconductor switch is delayed in turning ON and OFF due to its parasitic capacitance. There is a transient in the switch cycle waveform when it's turned ON and OFF. This leads to high switching losses during the turn ON and OFF period. Switching Frequency greatly influences the switching losses of the switch(hard-switching). The higher the switching frequency, the more will be the switching losses. Thus, a soft-switching technique needs to be adopted to limit the losses in the switch. Figure 2.12 showcases the voltage/current switching cycle in hard-switching and soft-switching modes. In a hard-switching operation, the current start rising during the switching OFF period irrespective of the voltage value and thus results in power loss(orange shaded region). While in soft-switching operation, the switching occurs when either voltage/current goes zero causing minimal power losses. Soft-switching techniques use a resonant tank across the switch, forcing the switch to turn ON and OFF[46]. More detail on this is discussed in appendix **??**.

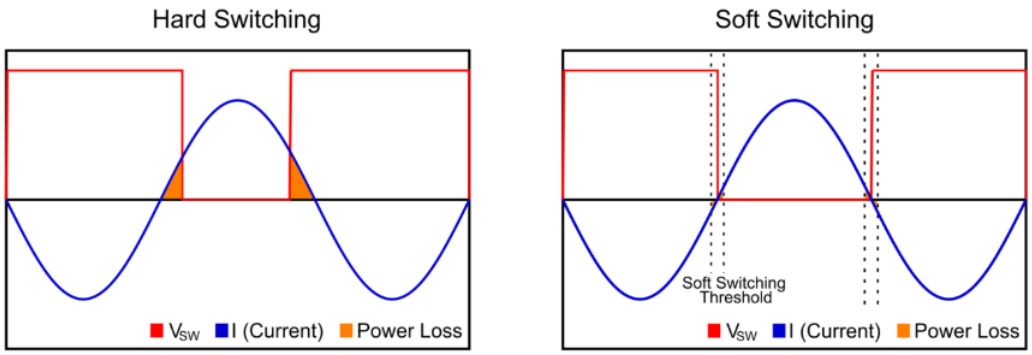

Figure 2.12: Comparison of hard-switching and soft switching operation [17]

2.5. Inductor

An inductor is a passive element that stores energy in a magnetic field when current flows through it. It consists of two terminals and a wire which is insulated and is looped around either air (left-figure 2.13) or a core material (ferromagnetic material) (right-figure 2.13) which can enhance the magnetic fields of the coil.

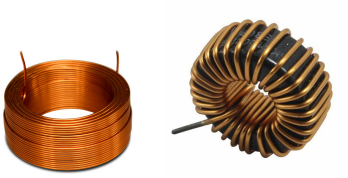

Figure 2.13: Air-coil(left) & Core-coil(right)

Before understanding the working principle of an inductor, let's focus first on understanding the behaviors of a straight wire conducting current. When a DC current flows through the conductor, magnetic fields are generated around it. The strength of these magnetic fields depends upon the amount of current flowing through the conductor. the direction of the magnetic field lines can be analyzed using Fleming's right-hand rule.

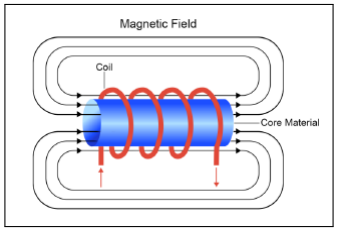

Figure 2.14: Straight wire carrying DC current[18]

When an AC current flows, it causes the generation of varying magnetic fields. These varying magnetic field lines cause changes in magnetic flux, inducing an electromotive force (EMF) in the coil. According to Lenz's law, the induced current due to varying magnetic fields will be in the opposite direction to the original current flow, thus restricting the flow of the original current in the coil. This ability to oppose a change in the electric current is referred to as the coil's inductance. The S.I. unit of inductance is Henry (H). The equation 2.11 shows the measuring of inductance.[18]

$$L = \frac{\mu_r \mu_0 \times A_M}{L_M} \times N^2 \tag{2.11}$$

Here;

- μ_r : relative permeability(core)
- μ_o : permeability of vacuum (4*π*10^-7)
- A_M : cross-section area of the coil
- L_M : Coil length
- N: number of turns

As can be seen in Equation 2.11, multiple factors influence the inductance value of a coil, like the number of turns in the coil, the coil's length, the coil, the cross-section area of the coil, and the material used for the coil. Using a core in the coil affects the magnetic field lines of the coil. Ferromagnetic materials are the most commonly used core material which increases the coil's magnetic field, thus increasing the coil's inductance.

2.5.1. Electrical Performance

Under a sinusoidal steady-state condition, the current in the inductor lags the voltage by a phase shift of 90^0. Assuming a sinusoidal voltage source of V_{in}*sin(ωt) to an R-L circuit, the voltage across the inductor will be

$$V_{\text{Source}} = V_{\text{in}} * sin(\omega * t) = -L * \frac{di}{dt} \tag{2.12}$$

reshuffling the above equation and integrating both sides gives us the current in the inductor;

$$i = (\frac{V_{\text{in}}}{\omega * L}) * sin(\omega * t - \frac{\pi}{2}) \tag{2.13}$$

Now, if we compare equation 2.12 & 2.13, we observe the phase difference between inductor voltage and current where current lags by 90^0

The inductor does not perform correctly when the current flowing in is outside the inductor's peak current range. The ripple current (ΔI_L) is the amount of current change during the Switch ON and OFF cycle. Figure 2.15 shows the inductor current ripple waveform.

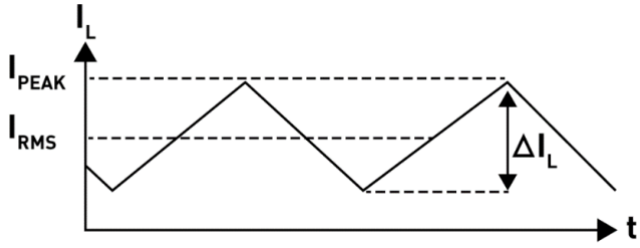

Figure 2.15: Inductor Current Ripple Waveform[19]

The best way to analyze an inductor is by understanding the Inductor Volt-second balance. Figure 2.16 shows an inductor's charging and discharging state. In area A, the inductor is continuously charged under a positive voltage storing energy. In contrast, in area B, the inductor is being discharged under the influence of negative voltage, thus releasing energy.

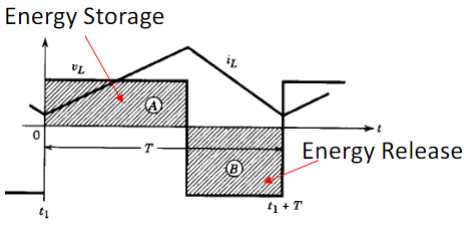

Figure 2.16: Inductor Volt-second Balance

Under a Quasi- steady state the inductor voltage v_L and inductor current i_L,

$$v(t+T) = v(t)$$
$$i(t+T) = i(t)$$

This shows that the final voltage value will be equal to the initial voltage over one complete cycle. Now we can transform the above equation into:

$$i_L = i_L(t_1) + \frac{1}{L} * \int_{t_1}^{t} v_L(t)\, dt \tag{2.14}$$

The voltage waveform across the inductor is reapting after every T time period, subsituting $t = t_{1+T}$ in eqaution 2.14, the inductor under steady-state condition results in

$$\frac{1}{T} \int_{t_1} t_1 + T v_L\, dt \tag{2.15}$$

Thus equation 2.15 shows that under steady-state conditions, the average inductor voltage equals zero. Also, from figure 2.16, it is seen that areas A and Area B are equal. Thus we can conclude that the net change of magnetic flux linkage in the inductor over one time period is zero.

2.5.2. Planar Coils

Recent advancement in power electronics has shown the development of microchips, also known as integrated circuits (ICs). Due to their advantages, like low power consumption, lower power losses, meager cost, and extremely small size have made them an optimal choice for circuit design. Today, almost every piece of electronic equipment is installed with an IC chip consisting of active (transistors) and passive (inductors) components equipped on a very small semiconductor substrate. Inductive power transfer (IPT) is an application widely used for contactless power transfer within a near field. Compared to capacitive power transfer, which works under the principle of electrostatic induction, IPT relies on magnetic induction via a magnetic field for transferring power [47]. Being this small, the planar coils used in the circuit are very small thin-film inductors. This opens up the possibility of using the IC chips for radio frequency applications which requires smaller inductance value. Although the topology of the inductor coil design varies according to the application, all of them have the same working principle. [48] has shown five different topologies of planar inductor coils spiral, tapered, non-spiral, meander, and fractal. The performance of these inductors was characterized mainly by their three important feature;

1. Inductance Value: how well it can handle the current ripples in the circuit.
2. Quality Factor: an important characteristic that defines the performance capability of the inductor.
3. Selft-resonating frequency (SFR): determining the operating frequency band of the inductor.

Based on the expermient[49], spiral topology showed the best inductance value measured at radio frequency among other topologies with a reasonably good Q-factor. Further research done by [50] on square planar coil showed how the coil's inductance value depends on the number of turns present in the coil. The equation 2.16(also known as Wheeler's approximation) gives the inductance value of a square planar coil [51].

$$L_S = \frac{\mu_0 \cdot n^2 \cdot d_{\text{avg}} \cdot c_1}{2} \cdot \left(\ln\left(\frac{c_2}{\Delta}\right) + c_3 \cdot \Delta + c_4 \cdot \Delta^2\right) \tag{2.16}$$

Here;

- μ_o : permeability of vacuum (4*π*10^-7)
- n: number of turns in a coil
- d_{dout} : outer diameter
- d_{in} : inner diameter)
- d_{avg}: 0.5*(d_{dout}+d_{in})
- Δ : (d_{out}-d_{in})/(d_{out}+d_{in})
- c1, c2, c3 & c4 : layout coefficient (varies with shape of planar coil)

2.5.3. Quality factor

The Q value is a parameter that illustrates the quality of an inductor. Inductors allow a relatively easy flow for direct current but act as resistors for alternating current. This nature of the inductor is known as inductive resistance/inductance. The higher the frequency of the alternating current, the higher the resistance. Although a coil is a conductor, the wire windings of the coil carry a certain degree of resistance in them. The ratio between this resistance and the frequency-dependent inductance is called the loss factor, and inversing gives us the inductor's quality factor. Depending upon the frequency of the current flow, the Q factor varies accordingly. So, higher Q values mean fewer losses and better use of inductors.

$$Q = \frac{2 * \pi * f * L}{R} \tag{2.17}$$

Here;

- f: frequency
- L: Inductance
- R: DC resistance component

2.6. Loss Mechanism in Inductor

The power loss of an inductor is defined by a basic equation:

$$P_{\text{loss}}(Inductor) = P_{\text{Core}} + P_{\text{dcr}} + P_{\text{acr}} \tag{2.18}$$

Here,

- P_{Core} : core losses provided by the core material present in the inductor
- P_{dcr} : loss caused by DC resistance
- P_{acr} : loss caused by AC resistance

2.6.1. Resistive losses

The resistance of a wire is given by the equation:

$$R = \frac{\rho * L}{A} \tag{2.19}$$

here;

- R : resistance of the wire
- ρ : resistivity of the wire material
- L : length of the wire
- A : cross-section area of the wire

Integrating a planar coil onto the surface of a solar cell will increase the total series resistance (solar cell series resistance + coil geometry resistance). The thickness of the planar coil does not have a big influence on the inductance value but majorly affects the DC resistance of the coil [52]. From equation 2.19, we can see that the resistance is inversely proportional to the cross-section area of the wire. Thus there is a trade-off between choosing the thickness level of the inductor and the cross-section area. To have a lower DC resistance in the coil, the thickness of the coil is needed to be small, but again doing so, the width of the coil must be increased to maintain the cross-section area of the coil. Going forward this way will introduce eddy currents in the coil. These eddy currents are proportional to the width of the wire[53]. The principle of eddy currents is based on electromagnetic induction. When a conductor is placed in a time-dependent magnetic field, the induced electric field generates eddy currents on the surface of the conductor. These eddy currents themselves generate a magnetic field that opposes any changes of the exciting field[54].

2.6.2. Skin-Effect

As previously discussed in the section on DC resistance, the other major type of resistance in inductors is caused by AC. One of those is due to a phenomenon known as the skin effect. In the skin effect, the alternating current tends to travel on the boundary of the conductor rather than at the center.

$$\delta = \sqrt{\frac{\rho}{\pi f_o \mu_r \mu_o}} \tag{2.20}$$

here;

- δ = skin depth
- ρ = resistivity
- f_o = signal frequency
- μ_r = relative permeability

- μ_o = permeability of free space (4*π*10^-7)

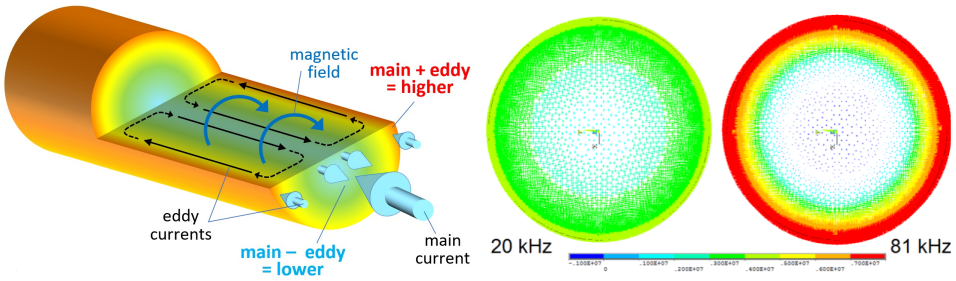

Figure 2.17: (a) skin effect phenomenon due to eddy current[20] & (b) skin effect dependency on frequency [21]

δ is a point at which the current density in the conductor reaches 37% to its value at the surface [21]. Skin depth largely depends on the material used for the conductor and the operating frequency. The principle behind the skin effect involves inducing eddy currents within the same conductor where the current flows. As the magnetic fields are present near the axis of the conductor, the eddy currents are produced in such a way that at the axis of the conductor, they are opposite in direction to the main current flow while in the same direction at the surface of the conductor (figure 2.17a) [20]. Thus at the edges, the eddy currents add up with the main current increasing the current density, while in the center, it opposes the flow of the main current, lowering the current density in the middle. This skin depth(region of current density) is inversely proportional to the signal frequency; hence with higher frequency, the skin depth is reduced, meaning the current density is much higher at the edge of the conductor than at the center (figure 2.17b). Table 2.2 is created using a skin depth calculator 2.17a. This table illustrates the effect of frequency on skin depth. Increasing the frequency reduces the skin depth, thus allowing more resistance in the conductor.

Table 2.2: Skin depth measurement at different frequencies

Frequency(Hz)	skin depth(mm)
1	65.200
100	6.520
1000	2.062
5000	0.922
10k	0.652
50k	0.291
100k	0.206
200k	0.145
300k	0.119
400k	0.103
500k	0.092

2.6.3. Proximity Effect

The proximity effect is the phenomenon when two or more conductors carrying alternating currents are placed near each other; then, their magnetic fields interact with each other. This interaction results in the redistribution of current inside the conductor, causing a non-uniform current density flow and increasing the resistance.

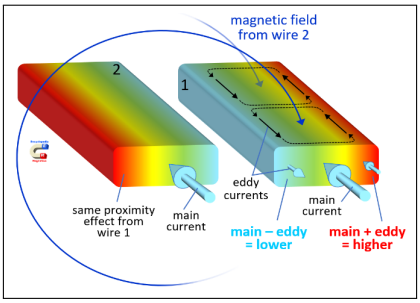

Figure 2.18: Proximity effect due to eddy current [20]

Similarly to the skin effect, the proximity effect also is caused due to the generation of eddy currents in the current-carrying conductor. However, the generation of eddy currents is influenced by the magnetic field lines of other nearby conductors. Figure 2.18 shows that eddy currents are generated in the body under the influence of an adjacent conductor's magnetic field. Now the direction of current flow in the adjacent conductor matters very much. If the current of the adjacent conductors is in the same direction, then the magnetic fields of the halves of the conductor adjacent to each other seem to cancel each other, thus reducing the current density in that half. While if the current in the adjacent conductors is in the opposite direction, the magnetic fields of the halves of the conductor adjacent to each other tend to add up, increasing the current density in that half while reducing it in the other halves [20]. Hence we see figure 2.19.

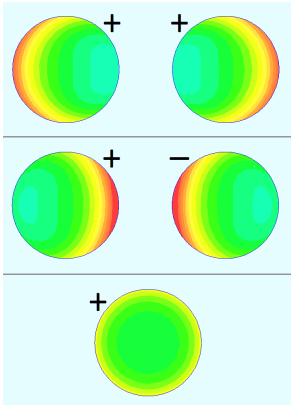

Figure 2.19: Proximity effect[20]

3

Simulation Method

This chapter will discuss the approach taken to answer the research sub-questions(section 1.6). Section 3.1 will give a brief discussion of the software used to design and simulate different converter topologies, while section 3.2 will discuss COMSOL Multiphysics software and the procedure of using it to design the planar coils

3.1. DC-DC Converter - Design and Simulations

Designing a converter requires a careful approach. There are several factors involved while designing a DC-DC converter to ensure optimal and efficient performance :

1. Input and output voltage level: knowing these values beforehand helps in deciding the converter's topology for design
2. Load's current: current requirement from the loads greatly influences the type of switch and inductors needed in the circuit.
3. Converter's efficiency: It is important to consider the operational efficiency of the converter as it affects the power losses during its operation.
4. Non-ideal behaviors: Critical to understand the non-ideal characteristics of components like switches, inductors, capacitors, and diodes, as their parasitic behaviors will have an influence on the performance of the converter.

One of the factors, the input voltage signal, is an essential parameter for designing the converter. Thus, a commercial PV module (Appendix E.3) is selected, and its electrical characteristics are used for design purposes. The converter designed for this PV module must be able to take a range of input voltages that necessarily contain the PV module's MPP and voltage deviations due to irregular irradiance. Also, the converter must be flexible in varying its duty cycle to perform MPPT for the PV module. There are certain assumptions made for the converter's design purpose:

- The converter is operating at 100% efficiency and a fixed duty cycle of 0.5.
- The solar cell (string) connected at the input of the converter is working at MPP
- The converter operates on a string of 10 series connected solar cells.
- All components in the converter are working ideally

Based on the above assumptions, the table 3.1 is drawn showcasing the electrical parameters of a string containing ten cells. A single solar cell's electrical parameters (appendix E.2) are used to derive the table 3.1

Table 3.1: String parameters

	String of 10 Cells
V_{MPP}(V)	6.33
I_{MPP}(A)	6.0800
P_{MPP}(W)	38.46

From the critical inductance equation 2.5, it is clear that the size of the inductor used in a converter is influenced by the converter's operating frequency(F_{sw}) and the amount of current ripple(ΔI_L) needed at the output. Thus, the ideal rule of thumb is keeping the current ripple value between 20% and 40% of the maximum load current [8]. To utilize the solar cell self-inductance, the lowest feasible inductor size for the converter's design is required. To achieve that, the F_{SW} and ΔI_L values must be high. Knowing that the maximum value of ΔI_L can be 40% of the inductor current ripple, and the F_{SW} value is limited by the fact that higher switching frequency leads to more switching losses. Table 3.2 shows the design parameters for sizing the inductor used in the DC/DC converter. This thesis work will study the inductor sizing for different switching frequencies (f_{SW}).

Table 3.2: Design parameters

	Parameter
f_{SW}	100 kHz
ΔI_L at 40%	2.432A
Duty Cycle(D)	0.5

Now, based on the above electrical parameters, different converter topologies like Boost, CUk, and SEPIC converters can be designed using software known as PLECS. It is software that is primarily used in power electronics engineering. It simplifies the modeling and simulation of power systems, including power sources, converters, and loads. The simulations are the result of a set of experiments performed on the schematic model in order to realize the real system behavior. PLECS uses an ordinary differential equation (ODE) solver. To understand the operation PLECS, assume a box where an input signal is provided and an output signal can be observed. The box contains many internal state variables that store information about past values and influence current behavior. This box contains physical model equations for the model, like Kirchoff's current and voltage laws. If the model contains only ideal elements, it's solved with steady-space equations.
PLECS has a comprehensive library covering the electrical, mechanical, and thermal aspects of power conversion systems. A PLECS user can capture any power electronic circuits on a schematic editor.
So, three types of products come under PLECS software[55]:

1. PLECS Blockset: This is a unique tool that is used by Simulink as an extension. It is present as a circuit block in Simulink, and the user can use it as a schematic editor. Later, with the help of a Simulink solver, simulations are performed (solving equations built-in solver).

2. PLECS Standalone: It is an autonomous software toolkit for time-domain simulations. It uses its own dedicated solvers for modeling and computing complex electrical circuits present in a single environment(no need for Simulink).

3. PLECS Coder: This tool kit generates C code from a PLECS model. Thus allowing the use of the code, which can be compiled to execute on the simulation host or a separate target like an embedded control platform or a real-time digital simulator.

An important remark about PLECS software is the power semiconductors present in the library are based on ideal switch implementation and, therefore, not recommended for non-ideal modeling applications. Thus, this software is primarily used in this project only to study the ideal operation of different converter topologies. To study the non-ideal case, a different type of software is used.
The schematic of the boost converter is realized in fig3.1. The schematic consists of an ideal MOSFET switch controlled by an external signal. A diode is also present, which closes as soon as the voltage across it is positive and opens when the current passing through it is negative. Both the diode and switch can be found in the library "Electrical-> Power Semiconductor". These components are ideal

and thus have a zero-resistance and infinite-off resistance. Although, it is possible to add a forward voltage in the diode.
The switch is made to be controlled by an external signal. A PWM generator(square wave) is used as an external signal. Such that the switch will be close to a non-zero PWM signal and open when the signal goes zero. By now, the schematic of the boost converter is realized like fig3.1.

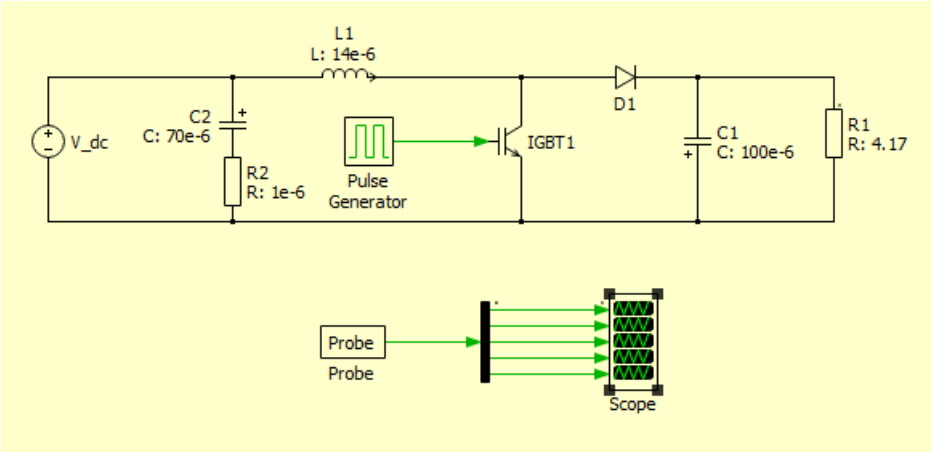

Figure 3.1: Boost Converter

This converter in Figure 3.1 uses an inductor with a size a bit higher than the critical inductance value (using equation 2.5). Thus making the converter operate at CCM. From figure 3.1, it can be observed that the converter uses an LC filter(L1 & C2) at the front side to dampen the input ripples in current and voltage. And at the end, use a capacitor (C1) big enough to handle the output current ripple (ΔI_L). A resistor is used to depict the load value. It is measured using the assumption that the efficiency of the converter is 100%, meaning the input and output power are the same.
Figure 3.2 shows the waveform of the Boost converter's operation. The IGBT voltage shows the switching cycle of the converter. V_{DC} is the source voltage at 6.33V, and R1 is the load voltage at 12.6V. From the inductor L1 current waveform, the charging and discharging of the inductor based on the switching period (IGBT voltage) can be observed. Also, it is essential to mention that the inductor current is not crossing zero and has an average of 6.08 with 40% ripple, thus making the converter operate in continuous conduction mode.

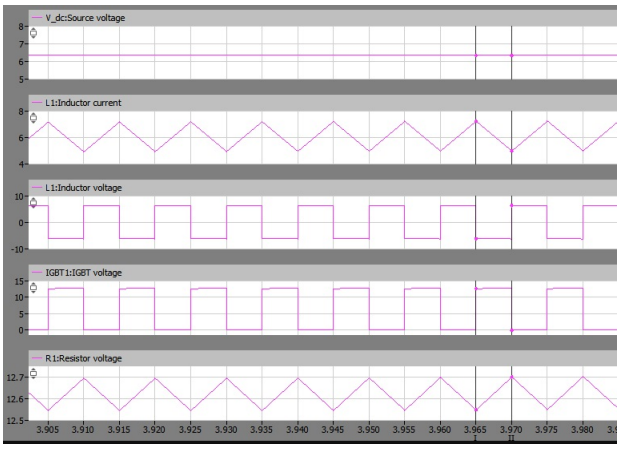

Figure 3.2: Boost Converter Waveform

3.2. Planar Coil - Design and Simulations

Now to answer the 2nd subquestion mentioned in section 1.6, it is important to simulate the planar coil designs. After studying different types of planar coils in section 2.5.2, it was realized that the square

spiral planar coils are the optimal coil design choice for generating high inductance.
Designing a planar coil requires consideration of several factors that may affect its optimal performance and efficiency. Some of them are:

1. Inductance requirement: inductance needed by an electric circuit will affect the design of the coil like the number of turns in the coil, the shape of the coil, and the spacing between the turns.
2. Circuit's operating frequency: Due to skin effect-related power losses, the planar coil design needs to be adjusted accordingly to reduce the skin effect
3. Resistance in the coil: as discussed in section 2.6, there are loss mechanisms in an inductor that can degrade its performance.

Voorn[56] proposed a set of planar coil designs modeled in COMSOL multiphysics software. He proposed planar coil designs with different coil turns and later observed the inductance and coil resistance generated in them. However, in his observations, the coils generated very high coil resistance (for 4 turn coil, the coil generated nearly 100mΩ) causing high power losses if integrated with solar cells. Nonetheless, there is further room for optimization in the design of these coils. This thesis will optimize the planar coil models by adding a gap in the middle of the geometry and by varying different parameters of the geometry.

COMSOL MULTIPHYSICS software is chosen to perform the simulations. This software is used to simulate designs, devices, and processes across all the fields of engineering and scientific research. It is also capable of simulating single-physics models. The model builder tool, available in the modeling workflow, is used for designing different geometries, material properties, and physics which describe a specific phenomenon for computation and evaluating results. COMSOL MULTIPHYSICS is based on the finite element method(FEM), which discretizes the partial differential equations (PDE) into smaller, discrete parts [57].

3.2.1. Geometry

Planar coils can be designed in many shapes and sizes depending on the required inductance. Depending upon the structure of a planar coil design, the inductance values differ. [49] and [58] discussed the inductance value obtained from different structures of the planar coil. Out of all the structures, the square planar coil resulted in a higher inductance value but at the same time with significant coil resistance. Figure 3.3 shows the layout of a square spiral coil with the parameters:

- t : the thickness of the coil
- s : spacing between the coil turns
- g : size of the gap at the center of the coil
- L : length of the coil
- N : no. of turns in the coil
- w : width of one single wire in the coil

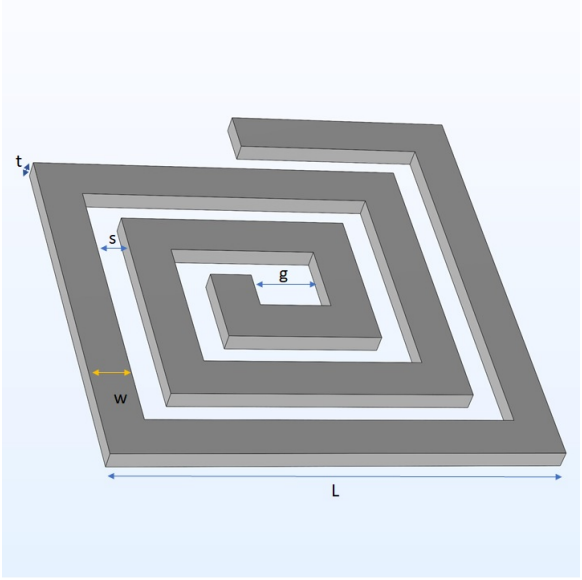

Figure 3.3: Coil Geometry

Length of the coil(L)
For screen-printing the planar coil of the back of the solar cell, the planar coil will take up the whole space of the cell (complete boundary); thus, the geometry (length & breadth) of the solar cell shall match the planar coil design. The Maxeon3 solar cell(referE.2) has a dimension of 12.5 X 12.5 cm^2, the length of the square planar coil is kept at 12.5cm.

Spacing(s)
Spacing between turns in a planar coil or also called coil spacing, refers to the distance between the adjacent turns in the coil. This parameter plays a vital role in determining the electrical characteristics of the coil. Thus, using a feature present in COMSOL multiphysics known as parametric sweep, the spacing parameter of the coil desing is varied to determine a planar coil design with optimal results. The function of parametric sweep is to run one specific parameter several times while keeping other parameters fixed.

Gap of the coil(g)
A hollow section is created in the center of the coil (as seen in the figure 3.2.1). Equation 3.1 is used to define gap parameter values for planar coil designing. Fixing the length and spacing parameter for any given number of turns in the coil, varying the gap parameter will inversely affect the width of the wire (refer appendix B tableB.2).

$$g = L - 2 * w * N - (N - 1) * 2 * s \tag{3.1}$$

width of the wire(w)
The width is another critical parameter that needs significant attention while designing a planar coil, as it is directly associated with power losses due to the skin effect. The coil structure is designed in such a way that the width of the coil is the only dependable value while the user sets all other parameters. The equation which determines the width of the coil at any given instance is:

$$w = \frac{L - g - (N - 1) * 2 * s}{2 * n} \tag{3.2}$$

This equation tells that at fixed L, g, and N values, the width of the wire will change due to varying spacing. Hence, the COMSOL model always creates a planar coil that encloses the entirely given area for the given spacing and gap parameters. For more information, refer to appendix B table B.3, which shows the wire's width change for the varying spacing parameter. The table is created for different numbers of turns in the coil but at a fixed length.

Thickness of the coil(t)
Awuah et al.[59] performed experiments on a planar spiral coil with varying thicknesses and observed that the resistance in the coil decreases when the thickness increases. It is also supported by the fact that when increasing the thickness of the coil, the cross-sectional area of the coil is increased, which in turn will reduce the DC resistance of the coil. For this thesis work, the planar coil is designed and studied with a thickness of 400μm. This thickness level is relatively higher than the standard thickness achieved using metallization techniques during the fabrication of solar cells [60]. However, 400μ is the lowest thickness level for the planar coil that can generate accurate results, as further decreasing the thickness resulted in high computational time for the COMSOL to generate results with the same accuracy.

Number of turns in coil (N)
The last parameter is the number of turns present in the coil. This parameter greatly influences the inductance value and the resistance generated in the coil. In this thesis, coils up to 5 turns are studied (figure 3.4).

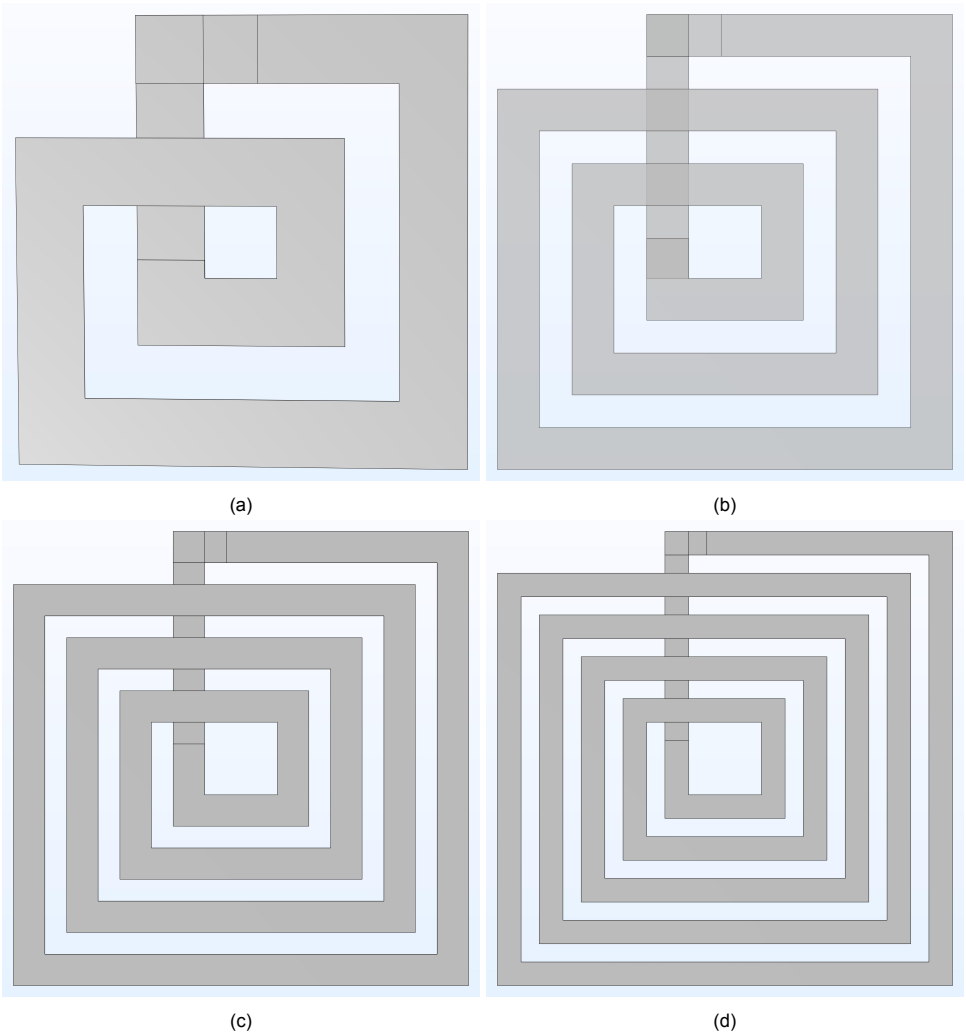

Figure 3.4: Planar coil design with several Turns: (a) 2-turn coil (b) 3-turn coil (c) 4-turn coil (d) 5-turn coil

3.2.2. Coil Structure
The geometry tab of COMSOL Multiphysics is where the coil architecture is created. There are five different levels to the design as a whole.

1. Coil Layer

The coil layer is designed using a polygon plane geometry. The polygon takes 2-D coordinates for designing the structure. Each turn of the coil has its own set of structure coordinates. An extend-feature of COMSOL geometry is used to apply the thickness to the coil, making the coil structure 3-D. Table 3.3 is used t design the 3-D coil structure of 2-5 turns coil in separate COMSOL. The xw and yw are the X-Y coordinates of the polygon plane geometry used. Similarly, the geometry of the coil with 2-Turns and 4-Turns can be referred from appendix B, table B.1.

Table 3.3: Show the polygon coordinates of the 3-turn Coil and 5-turn coil. The coordinates xw and yw represent the coordinates points of a polygon on XY plane

3-Turn			5-Turn	
xw	yw		xw	yw
-L/2+3*w+2*s	L/2 -2*s-3*w		-L/2+5*w+4*s	L/2 -5*s-5*w
-L/2+3*w+2*s	-(L/2 -2*s-3*w)		-L/2+5*w+4*s	-(L/2 -4*s-5*w)
-(-L/2+3*w+2*s)	-(L/2 -2*s-3*w)		-(-L/2+5*w+4*s)	-(L/2 -4*-5*w)
-(-L/2+3*w+2*s)	L/2 -2*s-3*w		-(-L/2+5*w+4s)	L/2 -4*s-5*w
-L/2+2*w+1*s	L/2 -2*s-3*w		-L/2+4*w+3*s	L/2 -4*s-5*w
-L/2+2*w+1*s	-(L/2 -1*s-2*w)		-L/2+4*w+3*s	-L/2+4*w+3*s
-(-L/2+2*w+1*s)	-(L/2 -1*s-2*w)		-(-L/2+4*w+3*s)	-L/2+4*w+3*s
-(-L/2+2*w+1*s)	L/2 -1*s-2*w		-(-L/2+4*w+3*s)	L/2 -3*s-4*w
-L/2+w	L/2 -1*s-2*w		-L/2+3*w+2*s	L/2 -3*s-4*w
-L/2+w	-(L/2 -1*w)		-L/2+3*w+2*s	-(L/2 -3*w-2*s)
-(-L/2+w)	-(L/2 -1*w)		-(-L/2+3*w+2*s)	-(L/2 -3*w-2*s)
-(-L/2+w)	L/2 -1*w		-(-L/2+3*w+2*s)	(L/2 -3*w-2*s)
-L/2+2*w+2*s	L/2 -1*w		(-L/2+3*w+2*s)	L/2 -3*w-2*s
-L/2+2*w+2*s	L/2		-L/2+2*w+s	-(L/2-2*w-s)
L/2	L/2		L/2-2*w-s	-(L/2-2*w-s)
L/2	-L/2		L/2-2*w-s	L/2-2*w-s
-L/2	-L/2		-L/2+w	L/2-2*w-s
-L/2	L/2-s		-L/2+w	-L/2+w+s
L/2-w-s	L/2-s		L/2-w	-L/2+w+s
L/2-w-s	-(L/2-s-w)		L/2-w	L/2-w
-(L/2-w-s)	-(L/2-s-w)		-L/2+5*w+5*s	L/2-w
-(L/2-w-s)	L/2-2*s-2*w		-L/2+5*w+5*s	L/2-w-s
L/2-2*w-2*s	L/2-2*s-2*w		L/2	L/2
L/2-2*w-2*s	-L/2+2*s+2*w		L/2	-L/2
-L/2+2*s+2*w	-L/2+2*s+2*w		-L/2	-L/2
-L/2+2*s+2*w	L/2 -2*s-3*w		-L/2	L/2-w-s
			L/2-w-s	L/2-w-s
			L/2-w-s	-L/2+w+s
			-(L/2-w-s)	-L/2+w+s
			-(L/2-w-s)	L/2-2*w-2*s
			L/2-2*w-2*s	L/2-2*w-2*s
			L/2-2*w-2*s	-L/2+2*w+2*s
			-(L/2-2*w-2*s)	-L/2+2*w+2*s
			-(L/2-2*w-2*s)	L/2 -3*s-3*w
			L/2-3*w-3*s	L/2 -3*s-3*w
			L/2-3*w-3*s	-L/2+3*w+3*s
			-(L/2-3*w-3*s)	-L/2+3*w+3*s
			-(L/2-3*w-3*s)	L/2 -4*s-4*w
			L/2-4*w-4*s	L/2 -4*s-4*w
			L/2-4*w-4*s	-L/2+4*w+4*s
			-(L/2-4*w-4*s)	-L/2+4*w+4*s
			-(L/2-4*w-4*s)	L/2 -5*s-5*w

2. Coil Vertices
Figure 3.5 shows the vertices plane added to the coil geometry. These vertices are an integral part of the coil design as they create an extension for a closed-loop coil structure. The vertices are created using the help of a new work plane, where again, with the help of polygon coordinates, a square geometry is created.

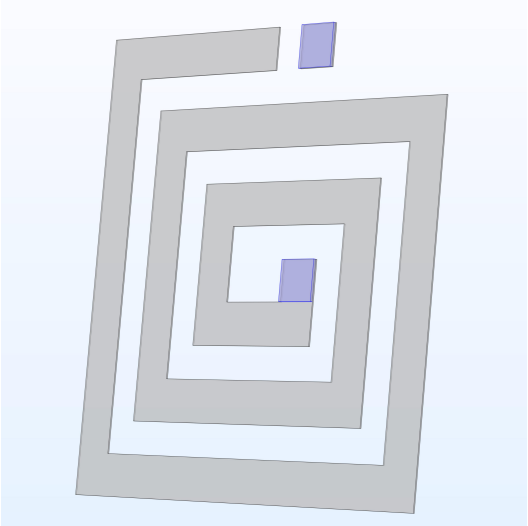

Figure 3.5: Coil Vertices

3. Coil Via
The planar coil structure is designed in a closed loop structure to comply with Maxwell's equations. Thus the vertices of the coil are connected through a terminal termed a Via. The purpose of making a closed-loop coil structure will be discussed in the section. The Via is created similarly to the vertices by creating a new work plane geometry and using polygon coordinates to form the Via terminal as figure 3.6

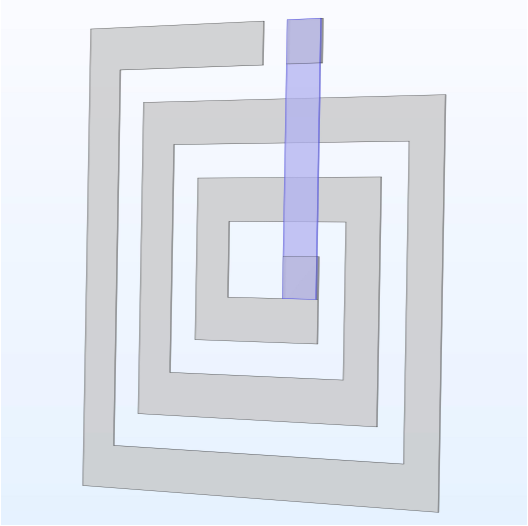

Figure 3.6: Coil Via

4. Insulation Inlet
This geometry is created for current excitation in the coil loop structure. As in a loop, there is no beginning and ending. For the design purpose, to study the inductance and resistance of the coil, a current needs to be flown in the coil. Thus intersection geometry (figure 3.7) is created in the coil where we can excite current for our study.

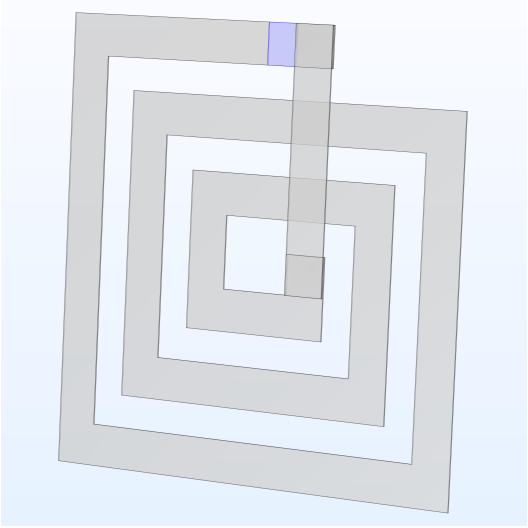

Figure 3.7: Coil Inlet

5. Air Domain
As one of the focuses of this thesis is to observe the inductance generated in the planar coil, an air domain is created around the planar coil to compute the magnetic field lines generated by the coil. The air domain is a spherical-shaped domain around the coil that perfectly incorporates the circular magnetic field lines generated by the coil. Figure 3.8 shows the spherical air domain around the coil.

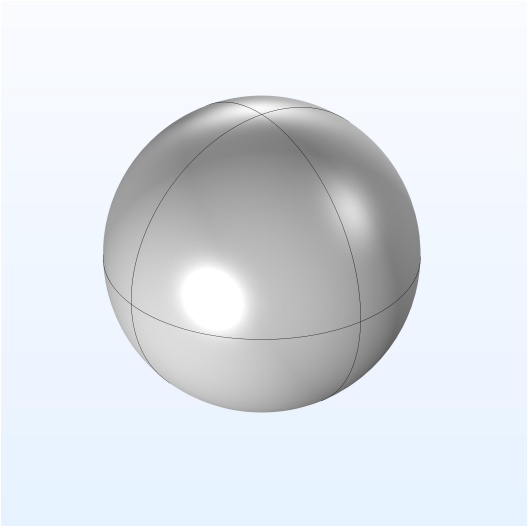

Figure 3.8: Air Domain

The inductance of a coil can be measured using equation 3.3. It can be observed from the equation that the inductance is directly proportional to the magnetic energy density (W_m) [61].

$$L = 2 * \frac{W_m}{I^2} \tag{3.3}$$

W_m for an inductor is defined as the energy stored in the magnetic field over an appropriate volume. This volume is the region around the coil. Hence, increasing the computation volume around the coil will result in more accurate inductance results. Although, computationally, it's not possible to define a sphere that can incorporate the magnetic field strength completely as it will significantly increase the computation time of the model. Thus a unique tool available in COMSOL Multiphysics is used to solve this issue. Since the magnetic field lines stretch to a very large distance from the model, an infinite element domain(IED) is introduced at the outer edge of the air domain. As the magnetic field lines

generated by the coil vary slowly with radial distance from the center of the domain, the finite element of the model is stretched in the radial direction in such a way that the boundary conditions present outside the IED domain can be applied to a very large distance from the region of interest(figure 3.9)[62]. The IED can be found in the definition tab of the component branch in the model. IED uses a preset value of pole distance (= dGeomChar m) and physical width(=1e3*dGeomChar m) values and are not interfered with for this model. These values allow us to compute a relatively small air domain to still simulate the magnetic energy density as if it were an infinite air domain.

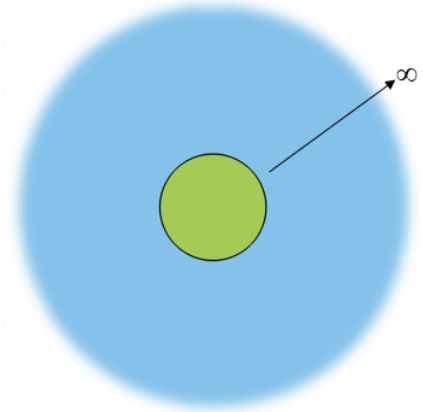

Figure 3.9: Region of interest (green) is within a region of infinite extent[22]

3.2.3. Materials

Materials tool available in COMSOL Multiphysics allows the user to assign material types to different layers in their model. In this model, the coil layer - coil geometry, vertices, Vias, and the inlet need to be assigned a metallic material to conduct the electric current and allow the flow of magnetic fields around. The material tool can be added to the component branch of the COMSOL geometry. After adding the material tool, copper material is added and assigned to the complete coil layer(including geometry, vertices, vias, and inlet). Assuming that the surrounding of the coil is air, the air domain (spherical volume around the coil) is assigned the material air.

3.2.4. Physics

When building a model in COMSOL and simulating it, one of the most important steps is to define the physics for computation. This includes choosing relevant physics for the model, adding the physical conditions and constraints, and assigning the physics to the geometric entities [63]. COMSOL Multiphysics provides plenty of physics interfaces to use. For this thesis, the important parameters that need to be studied are the coil inductance and coil AC resistance. Thus, the magnetic field (mf) is the most suitable physics for the model. This physics can be found under AC/DC > Electromagnetic fields. A magnetic field (M.F.) interface measures the magnetic field strength and current distribution in and around the coil. This interface solves the ”Maxwell’s equations, which are formulated using the magnetic vector potential and scalar electric potential as the dependent variables”[64]. One of the first nodes available in the M.F. interface is Ampere’s law node. The interpretation of Ampere’s Law from Maxwell’s equations is that the flowing electric current generates a magnetic field that encircles the current. Due to changing electric flux density, it gives rise to a magnetic field that circles the electric flux field. Thus Ampere’s law magnetic vector potential is added to all domains of the model.
The next node is the magnetic insulation which, when added as a boundary condition, ”sets the tangential component of the magnetic potential to zero at that boundary”[65]. This node is applied at the outer layer of IED, thus confining the magnetic field lines into the air domain as seen in figure 3.10

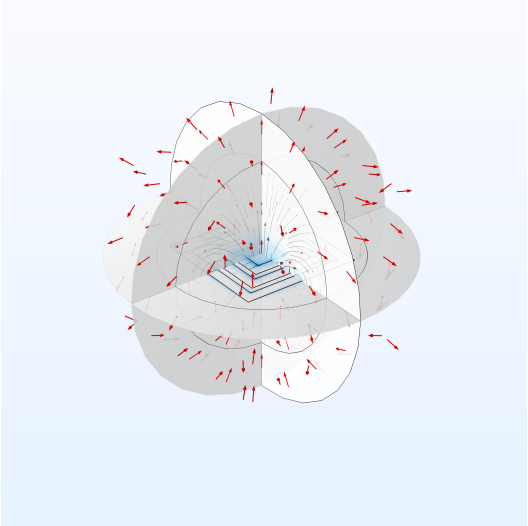

Figure 3.10: Magnetic field(red) generated by the coil in the air domain, confined due to magnetic insulation by IED

Another interesting feature available in this interface is the Coil node which, when applied, directs the COMSOL that the model created in the geometry node is a coil. The coil node consists of a sub-branch known as geometry analysis which selects a boundary in the model and assigns it as input to current excitation. For this purpose, the inlet square layer was added to the model such that its boundary (in figure 3.11) can be used as a current excitation zone.
Another essential node in the interface is the 'Gauge Fixing for A-field'. This node is necessary when vector(curl)shaped functions are used (Ampere's law). This "node enforces the guage be 0 by adding a potential variable Ψ"[66]. This allows the COMSOL solver to identify a unique and numerically stable solution when computing an equation that requires the magnetic vector potential.

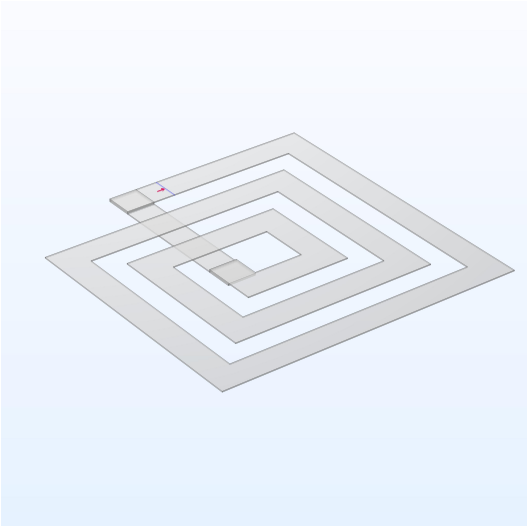

Figure 3.11: Current excitation in the inlet layer

3.2.5. Meshing

After designing the geometry model and assigning the physics to it, the next important step is to build the mesh. As discussed in section 3.2, COMSOL Multiphysics is based on the Finite element method, where the model is segregated into smaller elements, and each element is solved using partial differential equations (PDEs). Later, all the solutions obtained from the solving individual elements are combined to form one global solution. Meshing is the process of dividing the model into small elements. The mesh used in the models plays a major role in deciding how the model is solved, as it accounts for certain factors as[67]:

- dividing of the model's geometry
- type of element's shape after dividing the model
- size, density, and number of elements present in the model
- the quality of the element. expressed as 0 & 1, O being a low-quality element and 1 being high quality

These factors directly influence the computation of a problem, affecting the solver's time to solve the equations, the memory required to solve the equations, and the accuracy of the global solution. COMSOL software provides two types of meshing the model:

1. **Physic-controlled mesh** where the software automatically does it for the model. However, it allows the user to set the size of the elements generated. It generally provides nine different element sizes ranging from extremely coarse (large element size- poor quality) to extremely fine (very small size- good quality). Depending upon the size of the elements, the computation time and accuracy of the solution are determined. A smaller element size results in higher granularity meaning more elements and more solutions, thus resulting in an accurate global solution. However, the trade-off is a very large computation time and the need for a larger memory system. So, based on multiple experiments, it was founded that Finer element size is a good option for element size as it resulted in a good, usable solution with reasonable computation time.
2. **User-controlled mesh** allowing the user to build a custom mesh manually. This is done by changing the meshing sequences like size and distribution. And the mesh elements. In 3D meshing, the mesh elements can be divided into tetrahedrons. Hexahedrons, pyramids, and prisms. For this thesis's model, the user-controlled method opts as it allows a wider range of size and distribution to play with for determining the optimal size of the element, considering the computation time and the system's memory constraints. As the model is designed in 3D and the spacing/gap between the coil turns are varied due to changing thickness of the width of the coil (refer to equation 3.2 to see the width dependency on spacing and gap size), it gets difficult for the meshing algorithm to mesh in case of parametric sweeping. So the entire coil geometry meshes with a minimum element size of 0.2 such that at a very lower width of the coil, the mesh is sufficient enough to converge the solution (figure 3.12a). As the air-domain size is large, thus meshing it with similar conditions creates a very large amount of element, making it near impossible to compute; thus, the air domain is meshed separately using a tetrahedral shape and with a fine element size (figure 3.12b).

Figure 3.12a shows a user-controlled meshing done for the planar coil geometry. As the planar coils consist of 5 different layers, the surface of every single layer has been meshed separately with different textures to achieve accurate results, and later on, the function of *swept* has been used to mesh the entire model (3-D). A *Free Quad* mesh texture is applied on the coil geometry with a maximum element size of 0.2. In contrast, a *Free tetrahedral* texture is used to mesh the air domain with a predefined *fine* element size (Figure 3.12b).

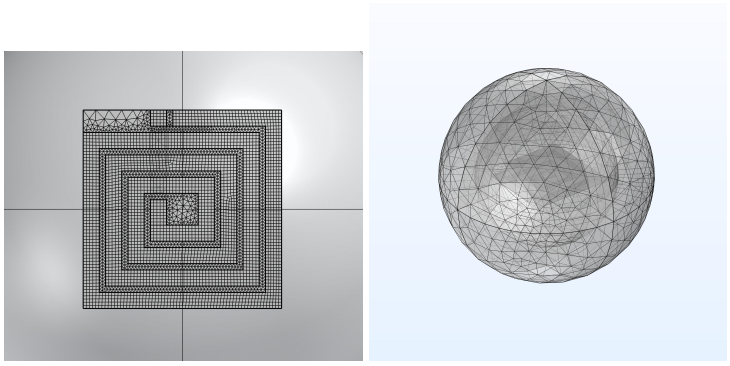

(a) (b)

Figure 3.12: Meshing of the model : (a) Coil geometry meshing (b) Air-domain meshing

3.2.6. Study

Selecting, adding, and running a specific study for a model is necessary in order to get results. Determining the appropriate study for a specific modeling scenario is vital to understand the analysis objectives for this model; the objective is to study the coil's resistance and inductance so that it can be integrated into the back of the solar cell. It is important to study the effectiveness of the planar coil for the inductor current ripples and how it will impact the coil's inductance and resistance.

In COMSOL Multiphysics, there are a plethora of predefined study types that can be used to study the model. However, for this model, a frequency domain study is conducted. This study is used when the model is subjected to conditions that vary with time. In the model, the current excited at the inlet square is varied with a frequency ranging from 1Hz to 500kHz. This range is selected based on the calculation of skin depth. As mentioned earlier, the skin effect increases with higher frequency, resulting in much higher AC resistance.

4

Utilising solar cell self-inductance

This chapter will discuss the findings from the converter and planar coil designs.

4.1. Conventional DC-DC Converter's passive element sizing

Figure 3.1 shows the circuit diagram of a conventional boost converter designed in PLECS software. The schematic uses passive elements like capacitors and inductors in its circuit. To perform a sub-module MPPT, the converter needs to be converting energy either at the cell level or at the string of cells level within the module.
To perform sub-module MPPT and replace the bypass diode, a converter needs to be connected to a string of cells. This way, if one or more cells on the string get partially shaded, rather than completely bypassing the string, the converter will operate the string at its MPP. To design the converter for a string of cells, a PV module with 13x8 cells was chosen (appendixE.1). The module contains 8 columns and 13 rows of cells Table 4.1 shows the electrical parameter of the string with 13 series connected cells. As all the 104 cells in the module are connected in series, V_{MPP} of the string will be 13 times 1/104th of V_{MPP}(module). But the I_{MPP} value will be the same for module and cell as the cells are connected in series.

Table 4.1: String of 13 Cells- Parameters

	1-cells
V_{MPP}(V)	8.22
I_{MPP}(A)	6.08
P_{MPP}(W)	50.0

In section 2.4.1, the critical inductance of a converter was explained with equation 2.5. The literature study found that all three topologies of the converter - Boost, CUK, and SEPIC- use the same critical inductance formulae. Observing the equation of critical inductance carefully, the inductance is inversely proportional to the converter's switching frequency(F_{sw}). Using the equation 2.5, table 4.2 is formed. This table shows the critical inductance requirement of the converter at different switching frequencies, with a fixed duty cycle at 0.5 and a current ripple at 40%.

Table 4.2: Critical Inductance for 13 cells

13 Cells	
F_{sw}(Hz)	Critical Inductance(H)
1	1.69
100	16.9m
1k	1,69m
5k	338μ
10k	169μ
20k	84.5μ
50k	33.8μ
80k	21.1μ
100k	16.9μ
150k	11.3μ
200k	8,45μ
500k	3,38μ

From the table 4.2, it can be observed that with increasing switching frequency. the inductance requirement by the converter is lower and lower (equation 2.5). Comparing the critical inductance requirement of the converter(table 4.2) to the solar cell self-inductance of 0.65μH (section:1.5.1- as all the cells are connected in series, their individual inductance of 50 nH will add up), the string overall inductance does not satisfy the critical inductance requirement of the DC-DC converter. This proves that a conventional DC/DC boost converter cannot be partially designed using only solar cell self-inductance.

The critical inductance equation (2.5) shows that if a very high switching frequency(2.7MHz) is used, then the cell's string can provide the required critical inductance for the converter's design. This will cause high losses in the system, as increasing frequency will result in heavy switching losses, especially for hard-switching converters [68], [69]. However, the limited operating frequency of the converter can be overcome by performing a zero-voltage/current soft-switching(ZV/CS). Thus different classes of converter topology known as resonant converters can become useful due to their ability to perform ZV/C soft-switching. A few preliminary results are shown in appendix A where it can be observed that using a resonant converter with multiple LC resonant tanks gives the possibility of integration of the converter onto a solar cell. However, the complex circuit design created a major drawback to fully exploiting this topology of the converter. Therefore, rather than changing the converter's topology, the solar cell's inductance is boosted by integrating a planar coil into it.

4.2. Increasing solar cell inductance- Planar coil

To increase the inductance value of a single solar cell, planar coils can be added as a layer on a solar cell. Fukuda et al.,[70] discussed different methods like screen-printing, photolithography, and electro-plating for adding planar coils depending upon their thickness. Although, by adding the planar coil, a certain amount of inductance can be generated on the cell, the coil's resistance will also be added to the cell, which will degrade the cell's yield. Thus in this study, the planar coil models proposed in [56] are optimized such that the planar coil generates a high inductance value with low resistance. The proximity and skin effect are the major cause of AC resistance in the planar coil. As the coil is compact and small, both of these effects play a dominant role in degrading the coil's electrical performance. Thus one by one, both of these effects will be suppressed by optimizing the coil designs. Having a fixed area on the solar cell (MAXEON3), the coil parameters like spacing and gap size can be varied for a limited coil width. Figure 4.1 and Figure 4.2 show the effect on the width of the wire when the spacing parameter and gap parameters are increased.

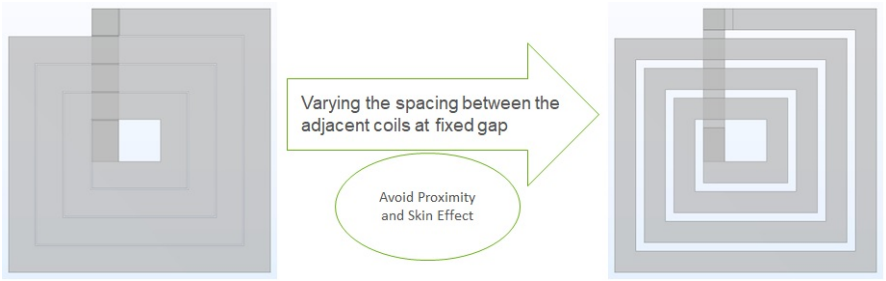

Figure 4.1: Varying spacing while fixing gap

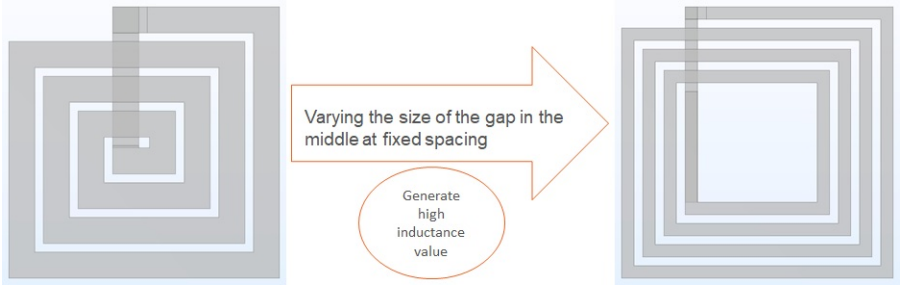

Figure 4.2: Varying gap while fixing the spacing

The following subsections will discuss the results obtained by varying the parameters.

4.2.1. Varying spacing (s)

Increasing the spacing value results in separation between the coil turns (refer fig4.1). Ac resistance losses like proximity effects play a dominant role when current-carrying conductors are placed near each other. TableB.3(Appendix B) is made using the equation 3.2. This table shows how the width of the coil is dependent on the spacing coil parameter. Increasing the spacing decreases the width parameter. However, the width cannot be physically negative; thus, spacing can only be increased till the least positive width value for all different turn coils. This limit provides an ample range of spacing values for the parametric sweep.

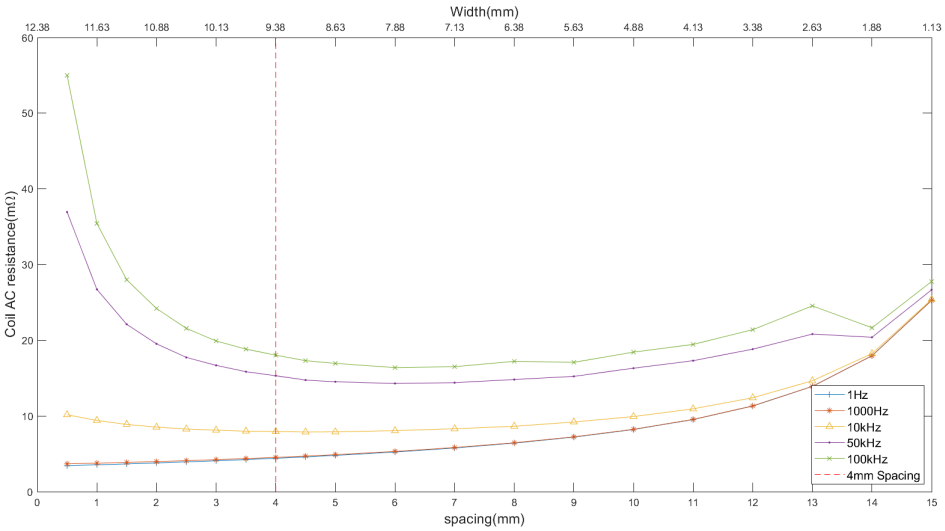

Figure 4.3: AC coil resistance(mΩ) for varying Spacing in a 4-Turn coil at fixed 2cm gap size

Figure 4.3 shows the simulation results of a 4-Turn coil. The graph shows the AC resistance value(Y-

axis) of the coil for different frequencies at varying spacing levels(bottom X-axis). The top X-axis shows the coil width value for the designated spacing values. Here are two trends to observe

- Focusing on the frequency, it can be observed that with the increasing frequency, the AC resistance increases, and this is mainly due to the skin effect where at high frequency, the current density shifts towards the edges of the wire, restricting the current to a small part of total cross-sectional area and thus increasing the resistance of the coil [71].
- focusing on the spacing(X-Axis), with increasing spacing, initially, the AC resistance at high frequencies (100kHz, 200kHz, and 500kHz) drops down. Presumably, this occurs because when the spacing increases, the distance between the wires increases, which eventually reduces the resistance caused by the proximity effect. Thus at lower spacing, for high-frequency signals, the proximity effect is dominant. This decreasing resistance trend can be seen till 4mm spacing (width=9.38mm). After this, the resistance remains quite at a similar level where the skin effect seems to be dominant. But after 9mm spacing (width = 5.63mm), the resistance increases mainly due narrowing width of the coil(DC resistance). As the width decreases due to increasing spacing, the DC part of the resistance will play the dominant role (equation 2.19).

Similarly, figure 4.4 shows the results of the Coil inductance value(Y-axis) for different frequency levels at varying spacing(X-axis). Similarly to the previous graph, this graph also has a top X- axis which represents the decreasing width value for increasing spacing. Two observations can be made from the graph;

- for lower spacing values up to 4mm(width = 9.38mm), with higher frequency, the inductance value of the coil decreases. Most likely, the skin and proximity effect forces the current to flow at the edges of the coil, changing the distribution of magnetic field lines and hence, affecting the self-inductance of the coil [72].
- for spacing values beyond 4mm, it can be observed that the coil's inductance increases linearly. It is likely that as the adjacent wires in the coil are carrying current in the same direction, increasing the distance between them allows adding the magnetic field lines. Hence, the magnetic field strength increases, increasing the overall inductance of the coil.

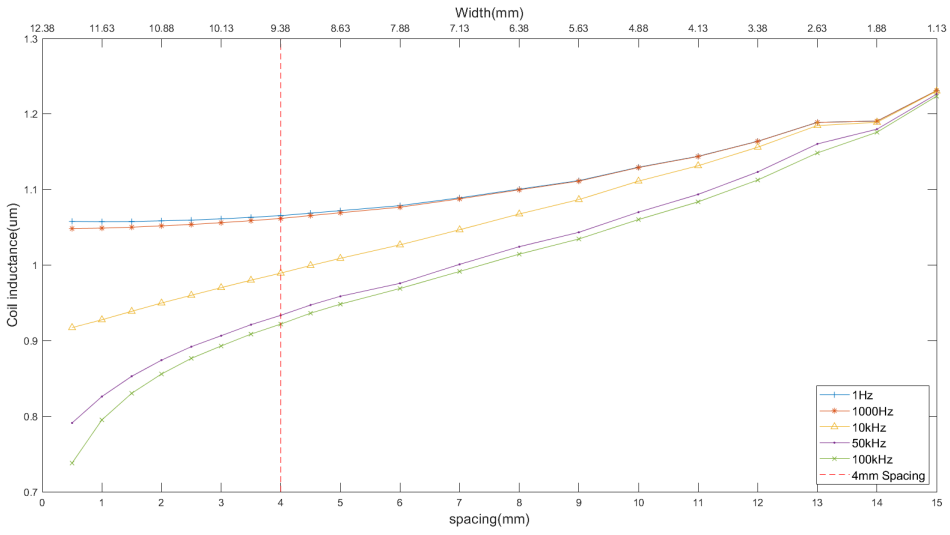

Figure 4.4: AC coil inductance(μH) for varying Spacing in a 4-Turn coil at fixed 2cm gap size

Conclusion

Varying the spacing parameter of the coil resulted in increased inductance value and lower AC resistance. Figure 4.5 shows the quality factor of the coil at varying spacing parameters. Quality factors as high as 38 can be observed for planar coils with spacing parameter s=9mm (width = 5.63mm).

However, the quality factors tend to be decreasing at higher spacing values mainly because at higher spacing, the width of the wire gets narrow, increasing the DC resistance in the coil.
Thus, it can be concluded that fixing the coil spacing at 4mm will dampen the proximity effect in the coil. A high-quality factor planar coil for frequencies 100kHz, 50kHz, and 10kHz is observed with coil parameters s = 9mm, g = 2cm, and width =5.63mm. Further, reducing the width significantly increases the resistance in the coil. Hence, fixing the spacing at 4mm and further reducing the width to 5.63mm by varying the gap parameter might result in planar coil designs with a much higher quality factor.

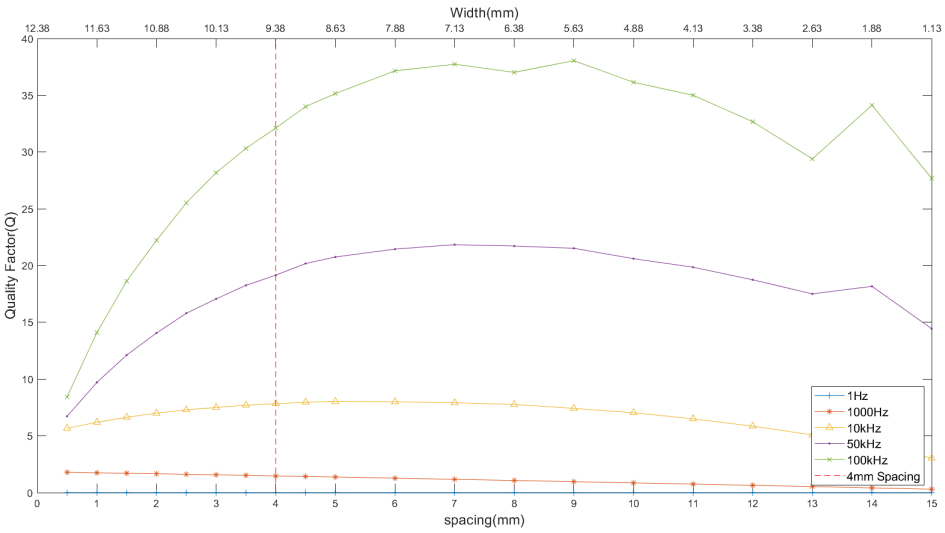

Figure 4.5: Q-factor Spacing between the coils(mm) for varying Spacing in a 4-Turn coil at fixed 2cm gap size

4.2.2. Varying gap-size(g)

Figure 4.2 is an illustration of changing the gap size of a planar coil. From equation 3.2, it can be realized that changing the gap size affects the width of the coil, similar to changing spacing. TableB.3(Appendix B) showcase the changing width size due to varying gap parameter of the planar coil. Similar to the spacing variation, the width of the coil decreases with increasing gap size of the coil. However, there is a limit to the increment of the gap size.

- width values cannot be non-positive values. Hence gap can only be increased till the least positive width value
- the least width of the coil is set at 5mm as below this width, fine meshing resulted in very high simulation time. Also, below 5mm width, the quality factor reduced significantly, as observed when varying spacing parameters.

Under these two limits, a wide range of gap sizes is created for the parametric sweep.

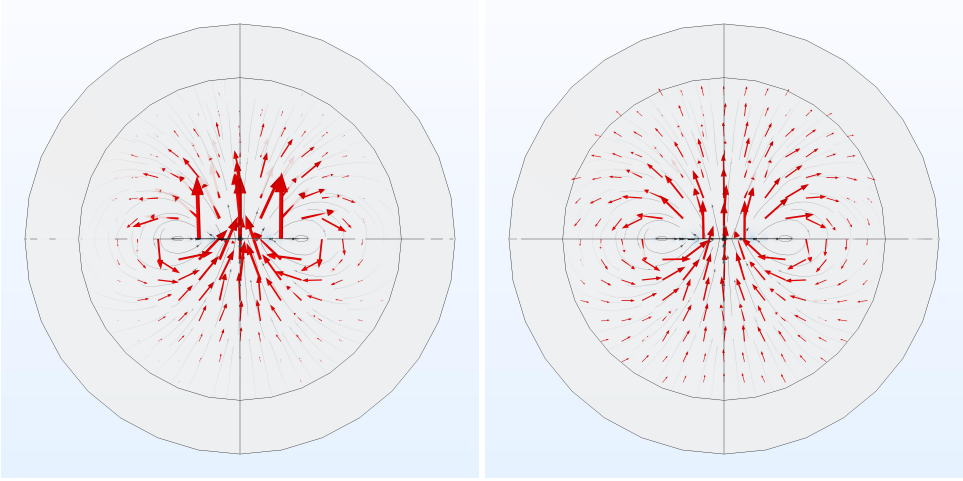

(a) (b)

Figure 4.6: Magnetic field lines of a 4-Turn planar coil with fixed s = 4mm and frequency of 500kHz for gap parameters (a) g = 2cm (b) g = 5.5cm

Figure 4.6 shows the distribution of magnetic field lines around the planar coil at gap parameters 2cm and 5.5cm. It can be observed in Figure 4.6a that when the gap size in the middle of the planar coil is small, the density of magnetic field lines is more concentrated towards the middle section. As the direction of current in adjacent parallel wires is the same, the magnetic field lines of each of them will add up, and thus the magnetic field lines density will be higher near the edges of the gap. If the gap is small, the magnetic field density at the gap's edge has less influence over the outermost wires in the coil. However, if we observe Figure 4.6b (also refer to Figure 4.2 to see the change in the model structure when the gap is increased), the edges of the gap are now much closer to the outermost wires because of the decreasing width. The wire now experiences a higher density of magnetic field lines through its cross-section, and hence it will influence the overall inductance generated in the coil. We can observe this effect on the planar coil through simulation results in Figure 4.7, where the inductance in the coil increases with increasing gap size. This increment in the inductance value is very large and can be verified with results from Figure 4.4 at a fixed width of 6.63mm. 4-Turn planar coil with coil parameter s = 8cm and g = 2 cm generates an inductance of 1.05μH at 100kHz (Figure 4.4 varying spacing), while with parameter s = 4mm and g = 5cm, the coil generates 1.62μH inductance at same frequency. Thus there is an inductance boost of 154% at 6.63mm width.

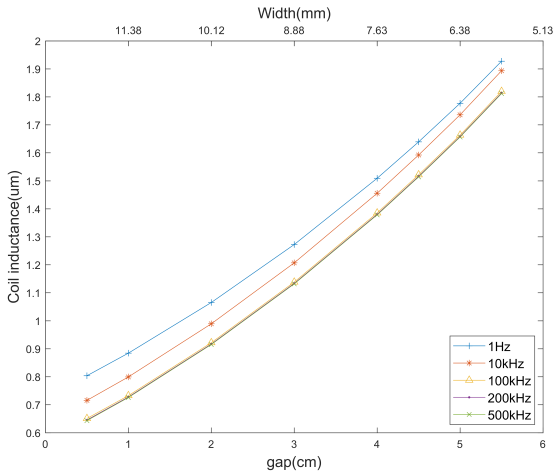

Figure 4.7: AC coil inductance(μH) for varying gap parameter in a 4-Turn coil at fixed spacing = 4mm

Figure 4.8 shows the influence of varying gap parameters on the Coil's resistance value. With increasing gap and parallelly decreasing the width of the wire, the skin effect should be weakened.

However, the coil resistance increases with the gap increment. It might be possible that, in this case, the series resistance of the coil dominates the skin effect. Nonetheless, due to a large boost of inductance in the coil, the quality factor of the planar coil has increased drastically (comparing results of Figure 4.5 and Figure 4.9 for 6.83mm width of the wire at 100kHz, the Q factor increased from 7 to 38)

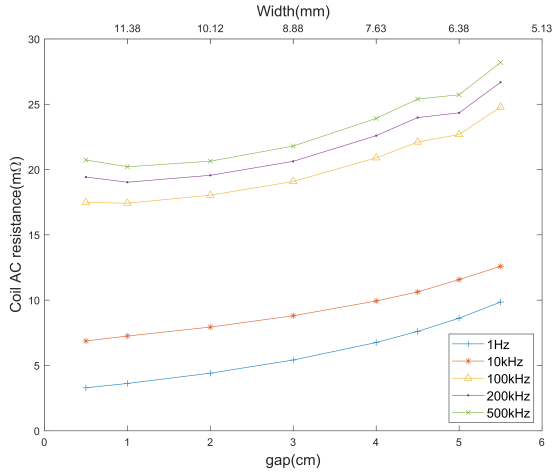

Figure 4.8: AC coil resistance(mΩ) V/s gap in coil(cm) for 4-Turn coil

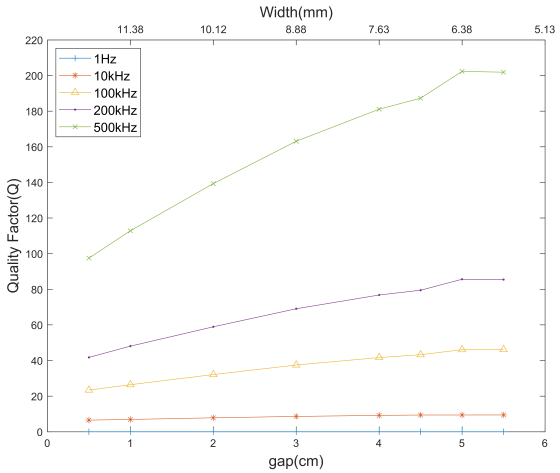

Figure 4.9: Coil Q-factor V/s gap in coil(cm) for 4-Turn coil

Conclusion
After fixing the spacing of the planar coil at 4mm to dampen the proximity effect, the gap size parameter of the planar coil is increased. Through the simulation, it was established that due to an increase in gap size, the coil inductance increases drastically. At the same time, the coil resistance has also increased due to changing size of the width. However, the increment in coil inductance outweighs the increment in coil resistance. It could be examined by analyzing the Q-factor of the coil, which was much higher than the Q-factor measured while varying spacing. This behavior of varying spacing and gap size in the coil can result in obtaining an optimal planar coil design with the highest quality factor and least coil resistance generation.

4.2.3. Different coils turns (N)
After determining the effect of spacing and gap size on coil performance, the next step is to examine the behavior of coils with different numbers of turns.

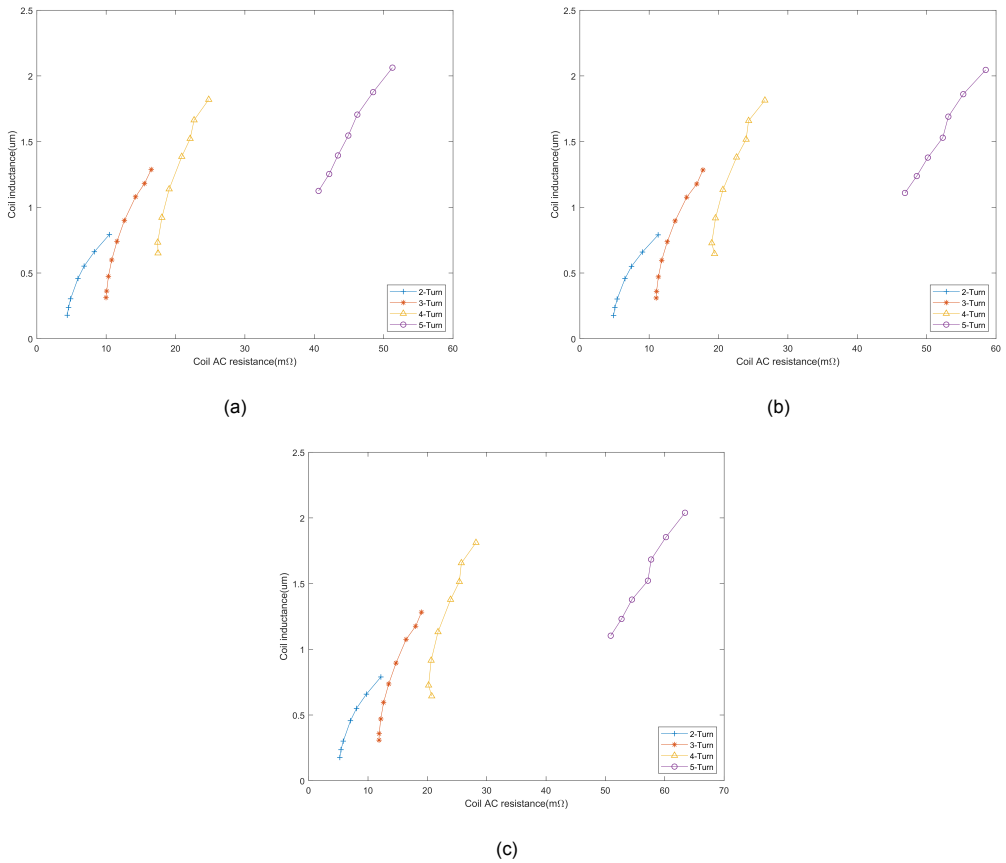

Figure 4.10: Coil Inductance (μH) V/s Coil AC Resistance(mΩ) at (a) 100kHz, (b) 200kHz, & (c) 500kHz

Figure 4.10 shows the simulation observations for 2, 3, 4, and 5-turn coils. The X-axis represents the coil AC resistance, and Y-axis represents the coil inductance value. The three graphs are plotted for different frequencies (100kHz, 200kHz, and 500kHz). The data are generated by fixing the spacing at 4mm and varying the gap size in the planar coil. Thus, numerous combinations of different gap sizes and the number of turns are possible for designing a planar coil. Appendix D shows all the possible combinations of planar coils with different turns and gap sizes. Comparing these results, it was observed that planar coils with large gap sizes and fewer turns can generate the same amount of inductance but with lower resistance values. This means that increasing the number of turns in a coil, the quality factor of that coil declines, and it can be observed in Figure 4.10, where a 5-Turn planar coil generates a large amount of coil resistance in comparison to lower turns coil while generating a similar amount of inductance.

4.3. Conclusion

To determine the possibility of utilizing the solar cell's self-inductance, the first condition checked was whether it could be used for designing a conventional DC-DC converter. To verify that, a conventional boost converter design was opted due to the position of the inductor at the front section of the circuit, which makes it easy to integrate the solar cell inductance with the converter. For designing the converter on a string with multiple cells, it was realized that the solar cell inductance was not sufficient for the design of the converter. If the converter's switching frequency is kept very high (> MHz), it is possible to design the converter with the cell's inductance. However, traditional converters are not suitable for high switching frequencies due to their hard switching operation mode, which results in very high switching losses for high switching frequencies. Thus, rather than utilizing the solar cell's self-generated inductance, if the inductance on the cell is increased by adding a planar coil, it might be suitable to design a conventional DC-DC boost converter.

To increase the solar cell inductance, a planar coil must be added as a layer on the back of the

solar cell. Adding the planar coil will increase the inductance of the solar cell. However, it will also add resistance, which will cause power losses. Thus, a planar coil needs to be designed to provide a high inductance value with minimum AC resistance. To achieve this, various parameters of the coil design are varied. Firstly, the spacing between the coil turns is varied to minimize the AC resistance generated in the coil. It was established that up to 4mm spacing, the proximity effect was dominant in causing AC resistance. But after 4mm, the skin effect and coil geometry caused resistance in the coil. Hence, the spacing was fixed at 4mm to diminish the proximity effect, thereby lowering the coil's AC resistance. Later, the gap size present in the middle of the coil is varied to achieve a high inductance value. Through multiple simulations, it was found that with a large gap size, the coil's inductance can be boosted up to 154% (for a wire width of 6.63mm) with a minimal increase in coil AC resistance. This resulted in designing planar coils with high-quality factors (up to 38 at 100kHz for the same-width wire). However, increasing the turns present in the coil showed that coils with a higher number of turns are less effective at achieving the required inductance at minimum resistance.

Thus, it was concluded that the DC-DC boost converter could be partially integrated into a solar cell if the solar cell inductance is boosted by adding a planar coil on its back surface. Many planar coil designs with varying parameters (number of turns, spacing between the coils, and gap size) showed promising results for DC-DC converter design. However, in the next chapter, optimal planar coil designs will be determined for the application of partial designing of DC/DC boost converter.

5

Suitability check for solar cell integration

This chapter will discuss the best possible selections of planar coil designs based on their inductor value and efficiency. The selected planar coil designs will be suitable for partial designing DC/DC converters on solar cells for applications like sub-module MPPT.

5.1. Selection of optimal planar coil designs

For sub-module MPPT application, the DC/DC converter must be operated efficiently. Adding the planar coil onto the solar cell will boost its inductance value. However, at the same time, the cell's series resistance will be increased by adding the coil resistance. Hence the total resistance will get increase and eventually cause power losses. Equation 5.1 shows the power loss caused by the planar coil.

$$P_{\text{Loss}} = I^2{}_{\text{RMS}} * (R_{\text{coil}}) \tag{5.1}$$

An optimal planar coil design must generate the lowest possible resistance for minimal power losses. Thus defining a term, inductor efficiency% (η_{L}) which is defined as:

$$\eta_{\text{L}} = \frac{(P_{\text{MPP}} - P_{\text{Loss}})}{P_{\text{MPP}}} * 100 \tag{5.2}$$

This equation will determine the efficiency of the planar coil designs for the power transfer operation. A planar coil with higher η_{L} will contribute highly to the overall efficiency of the DC/DC converter. Which most likely will make the sub-module MPPT more applicable.

The criteria to follow for deciding the optimal choice of planar coil designs are as follows;

- The inductance generated by the planar coil must be higher than the inductance requirement by the converter operating for given cells on the string.
- The resistance of the planar coil must be as small as possible to result in minimal power losses
- In the case of sub-module MPPT application on a string of cells, adding one or multiple planar coils in the string will provide the required inductance for the DC/DC converter design. Each cell will be equipped with only one planar coil; thus, the number of planar coils chosen will equal or less than the number of cells in the string. Each planar coil's inductance and resistance values will add up as the cells are series connected in the string.
  - Having less number of planar coils on the string will result in lower overall fabrication costs.
  - In a string, having multiple planar coils placed next to each other will have an adverse effect on their coil performance. Therefore having a lower number of planar coils in the string is better. However, the results obtained in this thesis do not consider the magnetic effect of two planar coils placed adjacent.

For higher granularity, the DC-DC converter can be either added to 1 cell or to a string that contains more than one series connected solar cells. Based on the number of cells in the string, the critical inductance of the converter will differ, and hence the planar coil design and quantity will also change. The chosen PV module (appendix-E, FigE.3) consists of a 13 X 8 combination of cells all connected in series. Thus, keeping the cell connection structure in mind, different cases are being studied in the following subsections.

5.1.1. Planar coil- 1 cell

For a DC-DC converter to operate on a single cell, it requires a critical inductance value of:

Table 5.1: Inductance requirement of converter for 1 solar cell

1 Cell Power = 3.846W	
F_{sw}(Hz)	Inductance Requirement(H)
100k	1,25μ
200k	0.645μ
500k	0.255μ

On comparing table**??** & table5.1, it can be observed that there is a difference of 50nH inductance value between the two. When integrating a DC-DC converter onto a solar cell, the cell's self-inductance (assumed to be 50nH) will contribute to the inductance requirement of the converter, and the additional requirement will be fulfilled by adding the planar coil. Thus apart from single-cell self-inductance ($50nH$), the table5.1 shows the additional inductance requirement for supporting the design of DC-DC boost converter. The planar coil must provide these inductance values.

Figures 5.1 show the coil inductance (Y-axis) and coil resistance value (X-axis) of a single planar coil design with multiple turns (2, 3, 4, 5). The red-dotted lines depict the required inductance values by the converter (values from table5.1) at all three operating switching frequencies (100kHz, 200kHz & 500kHz). The ideal choice for a coil design is when the planar coil generates the minimum required inductance value (above the red dotted line) and, simultaneously, the least producing coil resistance (towards the left side). Table 5.2 shows the best possible planar coil designs with different numbers of turns, which matches the critical inductance requirement of a converter operating on a single cell. The table also demonstrates the Power loss factor of the planar coil at different switching frequencies.

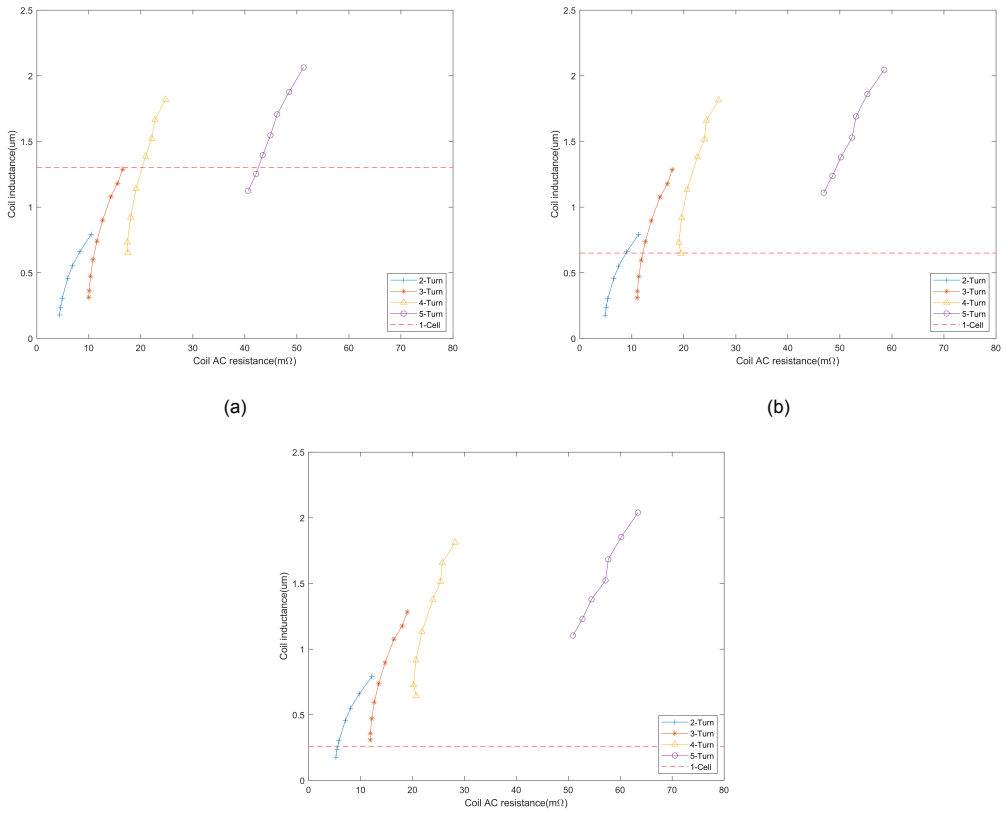

Figure 5.1: Inductance (μH)(Y-Axis) and AC Resistance(mΩ)(X-axis) of a single planar coils with different number of turns at(a) 100kHz, (b) 200kHz, & (c) 500kHz

Table 5.2: Optimal Planar coil choices for 1 cell at different switching frequencies of the converter

1 Cell		**Best Inductor Combination**				
f_{SW}(Hz)	Critical Inductance(uH)	Number of Coils for each Turns	L (uH)	R (mΩ)	P_{Loss} (W)	Inductor Efficiency(η_L)
100k	1,25	2Turn	NA	NA	NA	NA
		1-3turn	1,3	16,50	0,15	95,98
		1-4Turn	1,4	20,90	0,20	94,91
		1-5Turn	1,4	43,40	0,41	89,43
200k	0,645	1-2turn	0,7	9,03	0,08	97,80
		1-3turn	0,7	12,61	0,12	96,93
		1-4Turn	0,7	19,03	0,18	95,37
		1-5Turn	1,1	46,88	0,44	88,59
500k	0,255	1-2turn	0,3	5,83	0,05	98,58
		1-3turn	0,3	11,86	0,11	97,11
		1-4Turn	0,6	20,74	0,19	94,95
		1-5Turn	1,1	50,90	0,48	87,61

For 100KHz switching frequency, the critical inductance requirement by the converter is 1.25μH. Observing the plot in figure5.1a, no 2-Turn coil can generate the minimum required inductance. While a 3-Turn planar coil with a spacing of 4mm between the coil turns and a gap size of 7cm generates 1.26μH inductance which is more than the requirement for the converter. This planar coil design has an efficiency of 95.98%. However, if we check for higher turn coils (4 and 5), we can see from the table 5.2 the coil's efficiency is reducing with increasing turns.

For 200kHz switching frequency, the critical inductance requirement by the converter is 0.645μH. From the plot in figure5.1b, it can be seen that a single 2-Turn coil with a spacing of 4mm between the coil and a gap size of 8cm produces 0.661μH inductance which is sufficient enough for designing the converter. This planar coil design has an efficiency of 97.8%.

For 500kHz switching frequency, the critical inductance requirement of the converter is 0.255μH. From the plot in figure5.1c, it can be observed that a single 2-Turn coil with a spacing of 4mm between the coil turns and a gap size of 4cm is an optimal choice for designing a converter. This planar coil design has an efficiency of 98.58%.

Thus, this study found that choosing a planar coil consisting of fewer turns results in high inductor efficiency% (η_L).

5.1.2. Planar coils- 5 cells

If we consider a string containing 5 solar cells connected in series, the converter operating on them would require critical inductance of:

Table 5.3: Inductance requirement of converter for a string of 5 series connected cells

Total power of string of 5 cells = 19.231W	
F_{sw}(Hz)	Critical Inductance(H)
100k	6.25μ
200k	3.01μ
500k	1.05μ

The string of 5 solar cells generates self-inductance of 0.25μH. As each solar cell in the string generates a self-inductance of 50nH, adding all of them (due to series connection) will result in an overall inductance of $250nH/0.25\mu$H in the string. Apart from this, the additional inductance required for the converter to operate on the string of cells is calculated in table 5.3. Figures 5.2 show plots of Coil inductance (Y-axis) and Coil resistance(X-axis) for multiple planar coils with various turns (2, 3, 4, and 5) at frequencies of 100kH, 200kHz, and 500kHz. The red dotted line marks the critical inductance values from table5.3. These values set a limit for choosing the optimal coil designs and their quantity on the string.

Table 5.4 shows the best coil combinations for different quantities of coils in the string. As the string contains 5 cells, thus upto 5 planar coils can be used to generate the desired amount of inductance with high efficiency. Based on the string's critical inductance requirement(number of cells), the best planar coil design has been shown in the table.

Table 5.4: Optimal Planar coil choices for 5 cells at different switching frequencies of the converter

String of 5 Cells		Best Coil Combination						
F_sw (Hz)	Critical Inductance (uH)	Number of Coils	Type of planar coil Design (spacing =4mm)		L (uH)	R (mOhm)	Ploss (W)	Inductor Efficiency(%)
			Number of Turns	gap(cm)				
100k	6,25	1	NA	NA	NA	NA	NA	NA
		2	NA	NA	NA	NA	NA	NA
		3	NA	NA	NA	NA	NA	NA
		4	**4-Turn**	**5.0**	**6.66**	**90.73**	**0.85**	**95,58**
		5	4-Turn	4.0	6.92	104.50	0.98	94,91
200k	3.01	1	NA	NA	NA	NA	NA	NA
		2	**4-Turn**	**4.5**	**3.03**	**47.96**	**0.45**	**97,66**
		3	3-Turn	6.0	3.23	46.22	0.43	97,75
		4	2-Turn	9.0	3.16	45.20	0.42	97,80
		5	2-Turn	8.0	3.30	45.16	0.42	97,80
500k	1,05	**1**	**3-Turn**	**4.5**	**1.08**	**16.41**	**0.15**	**99,20**
		2	2-Turn	7.0	1.10	16.12	0.15	99,22
		3	2-Turn	6.0	1.37	21.13	0.20	98,97
		4	2-Turn	4.0	1.21	23.32	0.22	98,86
		5	2-Turn	3	1.178	27.25	0.26	98,67

For 100kHz switching frequency, the required critical inductance of the converter is 6.25μH. No three quantities of planar coil design could generate enough inductance for converter design. Increasing the quantities of the coil in the string further, it was observed that using 4 of 4-Turn coil with gap size =5cm satisfied the inductance generation criteria with the highest possible efficiency of 95.58% at 100kHz.

For 200kHz, the critical inductance requirement is 3μH. No single coil alone can generate enough inductance for the converter's design. Using more than one planar coil in the string with a unique design did show promising results by fulfilling the inductance criteria. Observing table 5.4, using higher quantities of planar coil, the 'N' parameter of the coil is reduced. From previous observations, having lower turns increases the efficiency of the coil. So, the ideal choice of planar coil combination would be using 5 of 2-Turns coil, which generates enough inductance for the converter's design at the highest efficiency of 97.8%. However, accounting for the coil's fabrication cost, lower quantities of the coil with suitable inductance generation would be a better consideration. Thus, using 2 of 4-Turns coil with gap parameter 4.5cm generates an inductance of 3.03μH, suitable for the converter's design at an efficiency of 97.66%.

For 500kHz, the critical inductance requirement is 1.05μ. Using a single 3-Turn coil with a gap parameter of 4.5cm will generate an inductance of 1.08μH, enough for the converter's partial design. This planar coil design has an efficiency of 99.2%.

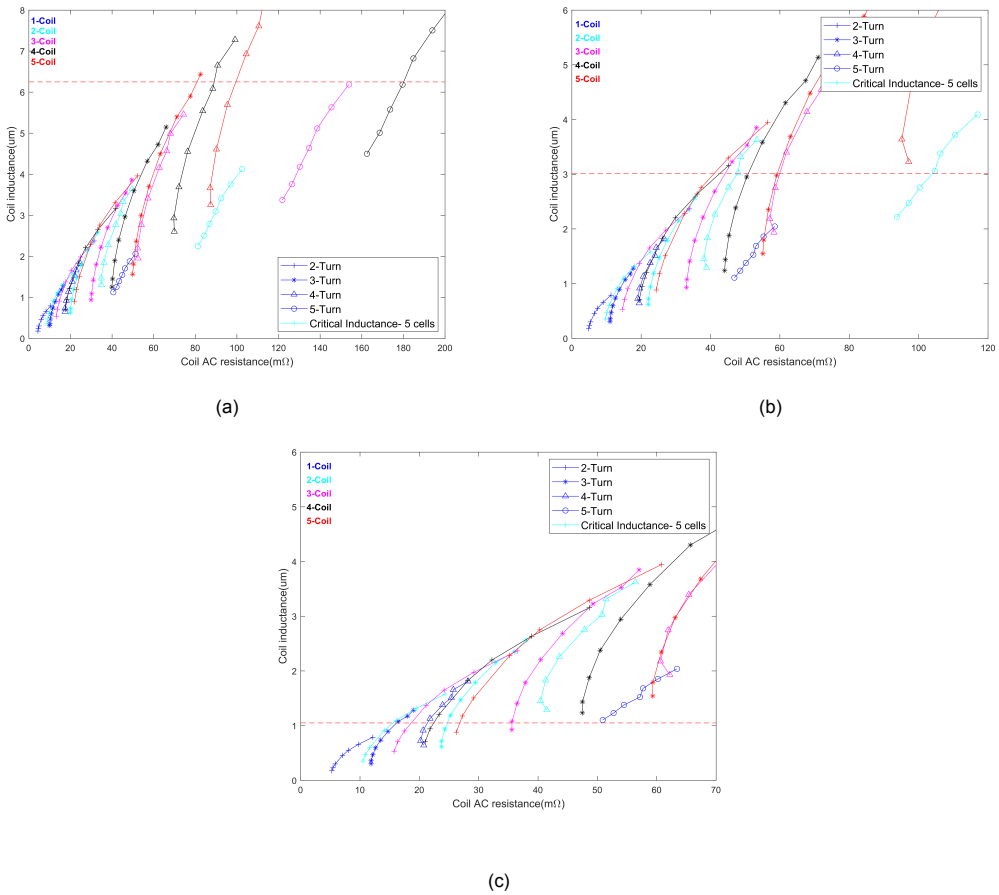

Figure 5.2: For a string of 5 series connected cells, Inductance and resistance values of multiple planar coils (colored data) with different coil parameters: varying gap and number of turns(shapes) at a frequency of (a)100kHz (b) 200kHz (c) 500kHz

5.1.3. Planar coils- 8 cells

Assuming that the commercial PV panel chosen for this thesis work has a string with 8 cells connected in series. Thus for a converter to operate for this string of cells, the required inductance value is :

Table 5.5: Inductance requirement of converter for a string of 8 series connected cells

Total power of string of 8 cells = 30.769W	
F_{sw}(Hz)	Critical Inductance(H)
100k	10.01μ
200k	4.80μ
500k	1.68μ

The string of 8 cells generates a self-inductance of 0.4μH where each solar cell contributes 0.05μH. Table 5.5 shows the additional inductance value required to design the converter for the string. The planar coil must deliver this inductance value while generating the least amount of AC coil resistance to avoid power losses. Table 5.6 presents the selections of multiple planar coil designs which generate more than the minimum inductance required for the converter design. The data in the table has been derived from figure 5.3. This figure shows the plot of Coil Inductance (Y-axis) and Coil resistance (X-axis) for multiple planar coils consisting of various turns (2, 3, 4, and 5). A red dotted line is also plotted in the graph, representing the minimum inductance requirement for the converter's design for different switching frequencies (100kHz, 200kHz, and 500kHz). Using this red line, it gets easier to find the optimal planar coil design generating minimum inductance requirement and loss ac coil resistance.

Table 5.6: Optimal Planar coil choices for 8 cells at different switching frequencies of the converter

String of 8 Cells		Best Coil Combination						
F_sw (Hz)	Critical Inductance (uH)	Number of Coils	Type of planar coil Design (spacing =4mm)		L (uH)	R (mOhm)	Ploss (W)	Inductor Efficiency (%)
			Number of Turns	gap(cm)				
100k	10.06	3	NA	NA	NA	NA	NA	NA
		4	NA	NA	NA	NA	NA	NA
		5	5-Turn	3.5	10.31	256.40	2.40	92.20
		6	**4-Turn**	**5.5**	**10.92**	**148.70**	**1.39**	**95.47**
		7	4-Turn	4.5	10.65	154.70	1.45	95.29
200k	4.8	**3**	**4-Turn**	**5.0**	**4.98**	**73.02**	**0.68**	**97.78**
		4	3-Turn	7.0	5.28	72.25	0.68	97.80
		5	3-Turn	6.0	5.38	77.03	0.72	97.66
		6	3-Turn	5.0	5.38	82.45	0.77	97.49
		7	2-Turn	9.0	5.53	79.11	0.74	97.59
500k	1.68	**3**	**2-Turn**	**8.0**	**1.98**	**29.19**	**0.27**	**99.11**
		4	2-Turn	6.0	1.83	28.18	0.26	99.14
		5	2-Turn	6.0	2.28	35.22	0.33	98.93
		6	2-Turn	4.0	1.80	34.99	0.33	98.94
		7	2-Turn	4.0	2.11	40.82	0.38	98.76

The required critical inductance for the converter's design for 100kHz switching frequency(figure5.3a) is 10.06μH. A 6 of 4Turn coil with a gap size of 5.5cm is the best planar coil combination among others as even though using a lesser quantity coil like 5 of 5Turns coil should be considered due to fabrication cost, the efficiency reduces by 3%, which can degrade the performance of converter during sub-module MPPT applications.

Similarly, for 200kHz, 3 of 4-Turn coil with a gap size of 5cm is the best combination for the partial design of the converter into the solar cell. This combination uses the lowest requirement of coil quantities while at the same time having an efficiency of 97.78%.

The required critical inductance for the converter's design for 500KHz switching frequency(figure5.3c) is 1.68μH. Using 3 of 4-Turns coils, each coil designed with a fixed geometry of s = 4mm and g = 0.5 cm, the overall inductance generated in the string is 2.17μH, enough to design the converter.

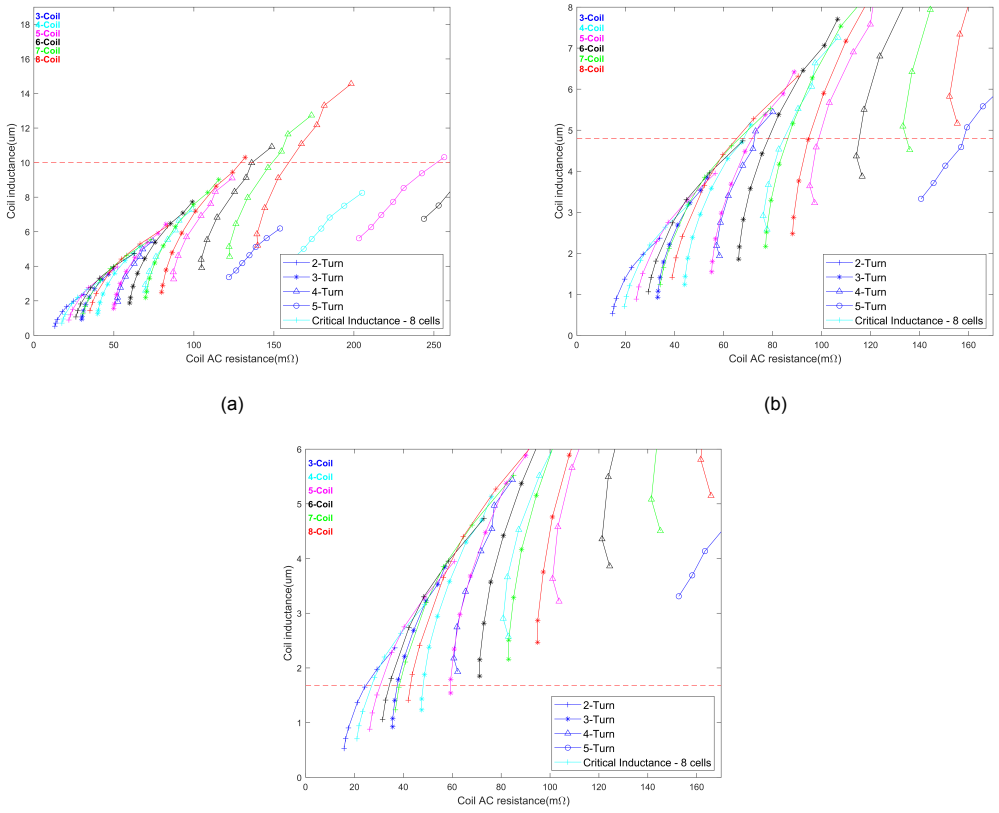

Figure 5.3: For a string of 8 series connected cells, Inductance and resistance values of multiple planar coils (colored data) with different coil parameters: varying gap and number of turns(shapes) at a frequency of (a)100kHz (b) 200kHz (c) 500kHz

5.1.4. Planar coils- 13 cells

Assuming now that a string contains 13 cells connected in series, a converter operating for it would require a critical inductance of:

Table 5.7: Inductance requirement of converter for a string of 13 series connected cells

Total power of string of 13 cells = 50W	
F_{sw}(Hz)	Critical Inductance(H)
100k	16.25μ
200k	7.80μ
500k	2.73μ

The self-inductance from each series connected solar cell in the string will contribute to the overall self-inductance generated in the string = 0.65μH. It is not sufficient to design the converter purely by using the inductance in the string. Hence, planar coils are required, which can provide the additional inductance required for the converter design. Table 5.7 displays the additional inductance requirement for the converter's design at three different switching frequencies. This inductance must be provided by adding the planar coil to the solar cell while generating the least coil resistance to avoid power losses.

Table 5.8: Optimal Planar coil choices for 13 cells at different switching frequencies of the converter

String of 13 Cells		Best Inductor Combination						
F_sw (Hz)	Critical Inductance (uH)	Number of Coils	Type of planar coil Design (spacing =4mm)		L (uH)	R (mOhm)	Ploss (W)	Inductor Efficiency (%)
			Number of Turns	gap(cm)				
100k	16.25	4	NA	NA	NA	NA	NA	NA
		5	NA	NA	NA	NA	NA	NA
		6	NA	NA	NA	NA	NA	NA
		7	NA	NA	NA	NA	NA	NA
		8	**5-Turn**	**3.5**	**16.50**	**256.40**	**2.40**	**95.20**
		9	4-Turn	5.5	16.38	223.00	2.09	95.82
		10	4-Turn	5.0	16.64	226.80	2.12	95.75
200k	7.8	4	5-Turn	3.5	8.18	234.10	2.19	95.62
		5	**4-Turn**	**7.0**	**8.30**	**121.70**	**1.14**	**97.72**
		6	4-Turn	4.0	8.28	135.60	1.27	97.46
		7	3-Turn	6.5	8.24	118.00	1.10	97.79
		8	3-turn	6.0	8.61	123.30	1.15	97.69
		9	3-Turn	5.0	8.07	123.70	1.16	97.68
		10	2-turn	9.0	7.89	113.00	1.06	97.88
500k	2.73	**4**	**2-Turn**	**9.0**	**3.16**	**48.65**	**0.46**	**99.09**
		5	2-Turn	8.0	2.75	40.30	0.38	99.25
		6	2-Turn	6.0	2.74	42.27	0.40	99.21
		7	2-Turn	6.0	3.20	49.31	0.46	99.08
		8	2-Turn	6.0	3.651	56.35	0.53	98.94
		9	2-Turn	6.0	4.11	63.4	0.59	98.81
		10	2-Turn	4.0	3.01	58.31	0.55	98.91

Table5.8 shows the best selections of planar coil designs for different quantities of coils used in the string. The type of planar coil design and their quantities are calculated using the plots in figure5.4. The graphs show Coil inductance (Y-axis) and Coil resistance (X-axis) values for multiple planar coil designs. The red dotted line is used as a marker/threshold, representing the converter's critical inductance requirement.

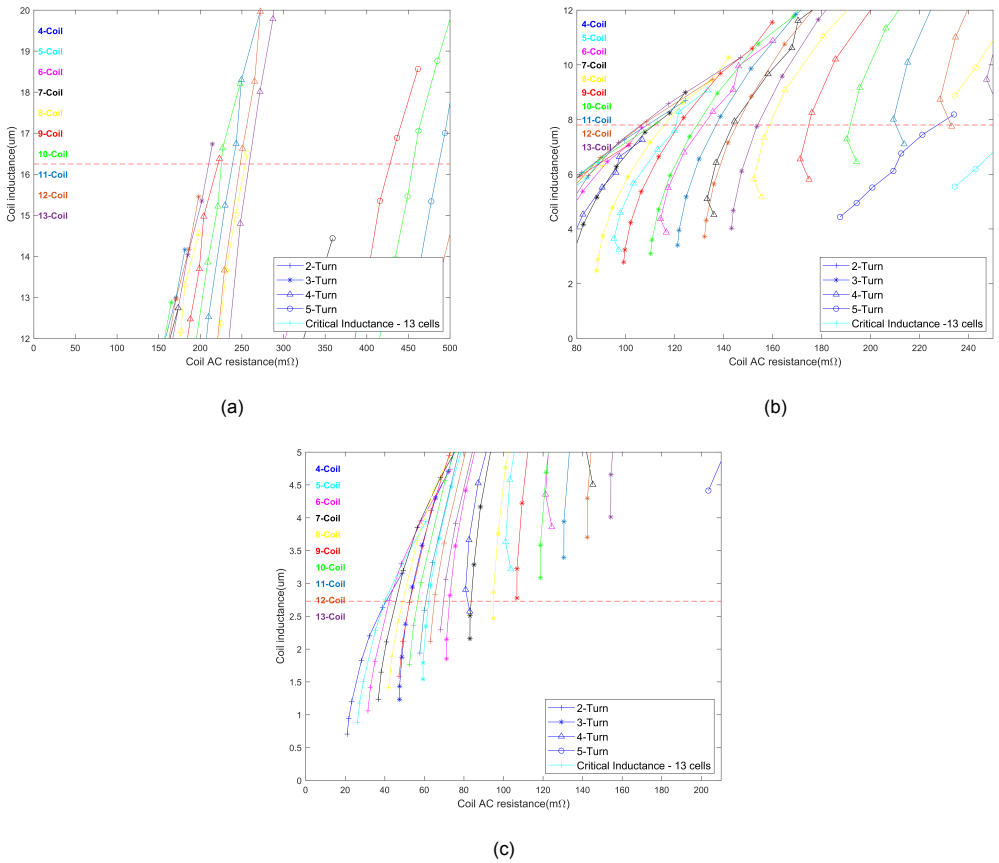

Figure 5.4: For a string of 13 series connected cells, Inductance and resistance values of multiple planar coils (colored data) with different coil parameters: varying gap and number of turns(shapes) at a frequency of (a)100kHz (b) 200kHz (c) 500kHz

For 100kHz switching frequency (figure 5.4a), the critical inductance requirement of the converter's design is 16.25μH. Using 5 of 4-Turn planar coils with gap parameter = 7cm, the overall inductance generated in the string is 16.50μH which satisfies the inductance requirement. This combination also has the least number of planar coils used in the string, thus making it a good choice considering the overall fabrication cost.

For 200kHz switching frequency (figure5.4b), the critical inductance requirement for the converter's design is 7.6μH. Although 4 of 5-Turn combination of planar coil uses a lower number of planar coils for the string, due to the use of a higher turn coil geometry, the overall efficiency is 95.62%. On the other hand, using one extra quantity of coil with a different structure(4Turn coil with a gap size of 7cm), the efficiency is increased by 2%, which might be beneficial during the converter's sub-module MPPT operation.

For 500kHz switching frequency (figure5.4c), the critical inductance requirement for the converter's design is 2.73μH. The best combination of planar coil was 4 of 2-Turn coils with gap parameter = 9cm.

5.2. Conclusion

For the partial design of the boost converter at the cell level, the string of solar cells needs to provide the required critical inductance. As the solar-cell self-inductance was insufficient for the converter's design, a planar coil with an optimal coil design is needed to boost the inductance of the solar cell. It was important to study the granularity of the converter inside the module. Thus few cases were studied where the converter was partially designed and operated on the string of multiple series-connected solar cells (5, 8, and 13) at different frequencies (100kHz, 200kHz, and 500kHz). Hence, in this chapter study, various combinations of planar coil designs are shown, which are suitable for partially designing DC/DC boost converter.

The optimal choice of planar coil combinations is based on the coil's capacity to generate the min-

imum critical inductance requirement for boost converter design while generating the least coil resistance to prevent power losses. Thus, the optimal planar coil model has the highest inductor efficiency (η_L) among all other planar coil combinations. However, accounting for the aspect of the coil's cost-effectiveness for fabrication, different planar coil combinations may be much more cost-effective than the optimal planar coil combinations. As the critical inductance requirement for the converter's design will vary according to the number of solar cells in the string, the need for planar coil quantities will vary. Thus, the best combination of planar coils has been selected for different quantities of planar coil needed in the string. This criterion will trim down the planar coil combinations, which are not cost-effective for fabrication.

After showcasing all the prominent combinations of the planar coil, a significant conclusion drawn from the results is that combinations with fewer quantities of coils sometimes work at slightly lower efficiency when compared to the optimal combinations. However, due to fabrication cost constraint, the combination with lesser coils are preferred over optimal choices by compensating slight drop in efficiency. For example, for a converter operating on a string of 13 cells at 200kHz, the optimal planar coil combination will be using 10 of 2-Turn coils with a gap size of 9cm. This combination results in an efficiency of 97.88%, which is the highest among all other possible combinations in this case. However, using a ten-planar coil is not cost-effective. Thus a different planar coil combination, which uses 5 of the 4-Turn coil with a gap size of 7cm, the efficiency of this combination is 97.72%. Although the planar coil combination has slightly lower efficiency, having half of the coil quantity compared to the optimal combination significantly improves fabrication cost-effectiveness.

Thus to conclude the study of this chapter, the best possible combination of planar coil designs is established for each string consisting of 5, 8, or 13 cells. However, all the planar coil models are designed for a thickness of 400μm. This thickness level is very high compared to the achievable thickness through the metallization technique while fabricating solar cells. Thus further research needs to be done on designing the planar coil models with lower thickness values, enabling them for solar cell integration.

6

Conclusion & Future Work

For the application of sub-module MPPT, the feasibility of partially designing a DC/DC boost converter onto a string of solar cells was studied in this thesis. In this chapter, the principal findings of this thesis project are summarised by the research questions posed in section 1.6. The main conclusion drawn from this thesis work is presented in section 6.1, followed by a few recommendations provided regarding further research on power electronics integration and studying different classes of DC-DC converters in area 6.2.

6.1. Thesis Conclusion

The primary objective of this study was to find a DC-DC converter design that works well with solar cells by using the cell's self-inductance as a design parameter. Traditional converter topologies like the Boost converter, CUK converter, and SEPIC converter were chosen due to the position of the inductor in their circuit design, which makes them a favorable choice for solar cell integration by utilizing their self-inductance. It was determined through the research that the inductor design equation is the same for all three of the DC-DC converters considered. For designing the converter, parameters like V_{in} and I_{in} are chosen from the datasheet of the commercially available PV cell, the Maxeon GEN3 solar cell. To perform maximum power point tracking at the sub-module level, it was assumed that the converter had been operated for a string of 13 series connected solar cells. The critical inductance required by the boost converter to operate is calculated using the solar cell's datasheet, a constant duty cycle of 0.5, and a current ripple of 40% for switching frequencies (from 1 Hz to 500 kHz). From the calculations, it was observed that for a string of 13 cells, the converter inductance requirement at 500 kHz switching frequency is 3.38μH which is very large in comparison to the total self-inductance generated in the string-0.65μH (sum of self-inductance of each cell). Thus, it was concluded that by only using the self-inductance of solar cells, it is not possible to partially design a DC/DC boost converter onto a solar cell. However, analytically it was possible to match the converter's inductance requirement with the solar cell self-inductance at a very high switching frequency (in MHz); traditional SMPS converters like Boost converter operate under the principle of hard-switching, which limits their switching frequency operation to a few 100s kHz.

The second research question was to investigate a planar coil design that can increase the solar cell inductance value and make it suitable for the conventional DC/DC boost converter's integration. Numerous planar coil layouts have been the subject of intensive investigation. Most of these analyses concluded that the coil's efficiency drops significantly because of the large amount of AC resistance it generates with the inductance. This thesis deals with optimizing the planar coil models designed in COMSOL Multiphysics to achieve inductance values suitable for converter design while generating the least coil resistance. A 3-dimensional planar coil with a gap in the center surrounded by a spherical air domain is built in COMSOL Multiphysics. The simulation results of this software determine the inductance and resistance values generated in the sphere. The planar coil is designed with coil parameters like length, width of the wire, spacing between the turns in the loop, gap size, and number of turns in the coil. A major finding from this study was that at high frequencies, factors like skin effect and parasitic effect play an important role by increasing the coil's resistance. Hence, dampening these effects

became necessary for designing planar coils with low resistance generation. The proximity effect in the coil is strong when the spacing between adjacent wires is small. Thus to dampen this effect, the spacing parameter of the coil is increased. Using parametric sweep in COMSOL Multiphysics, the spacing of the coil is increased while fixing other parameters like length, gap, and number of turns. Simulation results showed that the proximity effect in the coil almost completely disappeared at 4mm spacing, and skin effects became the major factor for the coil's resistance. With further increasing the spacing parameter or reducing the width of the coil, the skin effect remained dominant until the width of the wire reached 5.63mm. Further reducing the width, the DC resistance in the coil becomes dominant. At the same time, the coil's inductance kept increasing for increasing spacing because, with large spacing, the magnetic field density between the wires increased, increasing the inductance. This resulted in a good quality factor coil design with a width parameter between 9.83mm and 5.63mm. The quality factor can further be improved by increasing the inductance value within this width region. One of the most effective ways to do it is by increasing the gap parameter at fixed spacing. The planar coil models were then simulated for increasing the gap at 4mm fixed spacing. The simulation results showed that increasing the gap size boosted the inductance value by 154% (in comparison to increasing spacing). This eventually boosted the quality factor of the coil from 7 (max with varying spacing) to 38 (max with varying gap) at 100kHz. Thus, it was concluded that the DC-DC boost converter could be partially integrated into a solar cell if the solar cell inductance is boosted by adding a planar coil on its back surface. Many planar coil designs with varying parameters (number of turns, spacing between the coils, and gap size) showed promising results for DC-DC converter design.

The final research question was to identify the best combinations of planar coil designs for partial integration of a DC/DC boost converter into a solar cell. For the high granularity, the DC/DC converter is designed to operate (at frequencies = 100kHz, 200kHz, and 500kHz) for a string containing multiple series connected solar cells(5, 8, and 13). An optimal choice of planar coil combination should generate an inductance higher than the required critical inductance of the converter's partial design while also generating the least possible coil resistance for lower power losses. Thus, based on the string size(number of solar cells), the critical inductance of the coil will vary. For this thesis, it was assumed that only one planar coil can integrate into a solar cell. So, it was found that many combinations of planar coil design can fulfill the inductance requirement by either using a single planar coil or more than one in the string. However, considering the cost-effectiveness of fabricating the coil, different planar coil combinations might be best suitable for converter-solar cell partial integration. After obtaining all the best possible combinations of planar coils, it was observed that coils with fewer turns in their geometry had higher efficiency than those with high turns. Another observation was that by compromising a slight decrease in efficiency, using a suitable combination consisting of fewer coils is much more cost-effective than the optimal choice of coil combinations. For example, it was founded that for a string of 13 cells, 10 of 2-Turn coils satisfied all the criteria as well with an efficiency of 97.88%, which is the highest among all other combinations for this string size. Similarly, another combination- 5 of 4-Turn coils- satisfied all the criteria. However, this coil combination showed an efficiency of 97.72% though using half of the quantities used before. Thus this makes this coil combination more cost-effective for fabrication than other ones. This compromise with overall efficiency is applicable for a small percentage (<1%) as opting for planar coil design with low efficiency might degrade the performance of sub-module MPPT.

Thus, it was concluded in this thesis work that using only the solar cell self-inductance is not sufficient for partial integration of a conventional DC/DC boost converter onto a c-Si solar cell. Additional planar coil designs are shown, which can boost the inductance of the solar cell, making it suitable for converter integration. However, the proposed planar coils are designed with a thickness of 400μm due to computational constraints. In the PV industry, the metallization techniques used while fabricating a solar cell achieve a lower thickness. Therefore, further optimization of the planar coil design would be required for a lower-thickness coil.

6.2. Recommendation for Further research work

In this section, a few recommendations are put forward since these options could not be explored more within the time frame of this thesis project.

6.2.1. Other Converter Topologies

The first research topic was answered by focusing exclusively on the conventional topology of the converter (Boost, CU,k, and SEPIC). The resonant boost converter, however, stands out among the many different converter topologies due to its ability to execute zero voltage/current soft switching (ZVS/ZCS). This soft-switching allows the converter to operate at very high frequencies (in MHZ), thus reducing the size of passive components like inductors. Appendix **??** shows preliminary results obtained while studying and designing a resonant boost converter. However, resonance in a circuit brings a lot of complexity as exceptional control and gate drivers are required to stabilize the whole course. Thus, an intensive study in the resonant field might directly integrate the converter onto the solar cell without any planar coils.

6.2.2. Experimental model validation

The results from this thesis showed some best combinations of planar coil design. However, the results are obtained from a software simulation. Thus, it is essential to validate these results to measure their accuracy. This can be done by performing a real-time validation experiment on any planar coil combinations shown in this thesis. Thus, comparing the experiment results to the software-generated will give vital information about the meshing granularity needed in the planar coil simulation to generate accurate results.

6.2.3. Extre fine meshing of the COMSOL's planar coil models

Results from COMSOL simulations are susceptible to the meshing dimension of the underlying model. Due to the limited computational capacity of the system used for this thesis, the COMSOL model's meshing granularity was limited. Consequently, a system with high computational power will generate results with higher accuracy.

6.2.4. Using Magnetic plates with planar coil

This thesis demonstrated several optimized planar coil designs that produce sufficient inductance value with low resistance. However, it was found that converter operation on string with multiple cells (5, 8, and 13) needed more than one planar coil on the string. This might cause a high total fabrication cost. Thus, one way to reduce the use of many coils on the string is by using planar coil models with additional magnetic layers. Single planar coil inductance can be boosted using a magnetic layer on either top/bottom or both sides. The magnetic layer will influence the magnetic coupling between the layer and coil, hence might increase the inductance of the coil. Thus, a further study on optimizing the planar coil design by adding a magnetic layer might reduce the number of coils needed on the string for the converter's operation.

6.2.5. Using solar cells with larger surface area

As stated earlier, the planar coil models used in this thesis work are designed at 400μm thickness which is very high as per solar cell metallization standards. Thus, a planar coil with far lesser thickness must be designed to integrate into a solar cell. However, reducing the thickness correspondingly would require a higher-width wire for lower DC resistance in the coil. As the width of the planar coils proposed in the thesis has a lower value due to a larger gap size, using a solar cell with a large surface area might provide enough for large-width optimal planar coil designs. Thus further research on the effects of the cell's surface on a planar coil design might help reduce the coil's thickness.

Bibliography

[1] Hannah Ritchie, Max Roser, and Pablo Rosado. Energy. *Our World in Data*, 2022. https://ourworldindata.org/energy.

[2] Nadarajah Kannan and Divagar Vakeesan. Solar energy for future world:-a review. *Renewable and Sustainable Energy Reviews*, 62:1092–1105, 2016.

[3] Florida's Premier Energy Research Center at the University of Central Florida. Cells, modules, panel, and array. https://energyresearch.ucf.edu/consumer/solar-technologies/solar-electricity-basics/cells-modules-panels-and-arrays/.

[4] David A van Nijen, Patrizio Manganiello, Miro Zeman, and Olindo Isabella. Exploring the benefits, challenges, and feasibility of integrating power electronics into c-si solar cells. *Cell Reports Physical Science*, page 100944, 2022.

[5] Alaa A Ismail and Amgad A El-Deib. Dc/ac conversion topologies for photovoltaic applications. In *2023 IEEE Conference on Power Electronics and Renewable Energy (CPERE)*, pages 1–6. IEEE, 2023.

[6] Romênia G Vieira, Fábio MU de Araújo, Mahmoud Dhimish, and Maria IS Guerra. A comprehensive review on bypass diode application on photovoltaic modules. *Energies*, 13(10):2472, 2020.

[7] Kamran Ali Khan Niazi, Yongheng Yang, and Dezso Sera. Review of mismatch mitigation techniques for pv modules. *IET Renewable Power Generation*, 13(12):2035–2050, 2019.

[8] Brigitte Hauke. Basic calculation of a boost converter's power stage. *Texas Instruments, Application Report November*, pages 1–9, 2009.

[9] Christiana Honsberg and Stuart Bowden. Standar solar spectra. https://www.pveducation.org/pvcdrom/appendices/standard-solar-spectra.

[10] Rick Ivins. Optimizing I-V curve tracing activities, 2022. https://www.purepower.com/blog/optimizing-iv-curve-tracing-activities.

[11] Smets, Arno HM, Jäger, Klaus, Isabella, Olindo, Swaaij, René ACMM, Zeman, and Miro. *Solar Energy: The physics and engineering of photovoltaic conversion, technologies and systems*. UIT Cambridge, 2015.

[12] Jingquan Chen, Robert Erickson, and Dragan Maksimovic. Averaged switch modeling of boundary conduction mode dc-to-dc converters. In *IECON'01. 27th Annual Conference of the IEEE Industrial Electronics Society (Cat. No. 37243)*, volume 2, pages 844–849. IEEE, 2001.

[13] Sciamble. Boost converter-continuous conduction mode(ccm), 2022. https://sciamble.com/resources/pe-drives-lab/basic-pe/boost-converter.

[14] S Masri and PW Chan. Design and development of a dc-dc boost converter with constant output voltage. In *2010 international conference on intelligent and advanced systems*, pages 1–4. IEEE, 2010.

[15] Jeff Falin. Designing dc/dc converters based on sepic topology. *Texas Instruments Incorporated*, 2008.

[16] *LM2611 1.4MHz Cuk Converter*. National Semicondutor Corporation, 2002.

[17] Robert CN Pilawa-Podgurski, Anthony D Sagneri, Juan M Rivas, David I Anderson, and David J Perreault. Very-high-frequency resonant boost converters. *IEEE Transactions on Power Electronics*, 24(6):1654–1665, 2009.

[18] Sven Spohr. *Understanding Power Inductor Parameters*, 2022.

[19] Mohan N Undeland, Wiliam P Robbins, and N Mohan. Power electronics. *Converters, Applications, and Design*, page 763, 1995.

[20] Stan Zurek. Proximity effect, 2022. https://e-magnetica.pl/proximity_effect.

[21] AL Williams. Skin effect in the game, 2017. https://hackaday.com/2017/11/22/skin-effect-in-the-game/.

[22] COMSOL Multiphysics. Geometry and mesh setup for modeling regions of infinite extent, . https://www.comsol.de/support/learning-center/article/Geometry-and-Mesh-Setup-for-Modeling-Regions-of-Infinite-Extent-52791.

[23] Yanfeng Shen, Huai Wang, Frede Blaabjerg, Xiaofeng Sun, and Xiaohua Li. Analytical model for llc resonant converter with variable duty-cycle control. In *2016 IEEE Energy Conversion Congress and Exposition (ECCE)*, pages 1–7. IEEE, 2016.

[24] John Chrsity. Emerging market economies- the bric, 2022. https://www.thebalancemoney.com/top-emerging-market-economies-1979085.

[25] Jeff Tollefson. Scientists raise alarm over 'dangerously fast' growth in atmospheric methane, 2022. https://www-nature-com.tudelft.idm.oclc.org/articles/d41586-022-00312-2.

[26] Frederica Perera and Kari Nadeau. Climate change, fossil-fuel pollution, and children's health. *New England Journal of Medicine*, 386(24):2303–2314, 2022.

[27] Ehsanul Kabir, Pawan Kumar, Sandeep Kumar, Adedeji A Adelodun, and Ki-Hyun Kim. Solar energy: Potential and future prospects. *Renewable and Sustainable Energy Reviews*, 82:894–900, 2018.

[28] Vijay Devabhaktuni, Mansoor Alam, Soma Shekara Sreenadh Reddy Depuru, Robert C Green II, Douglas Nims, and Craig Near. Solar energy: Trends and enabling technologies. *Renewable and Sustainable Energy Reviews*, 19:555–564, 2013.

[29] David L. Chandler. Explaining the plummeting cost of solar power, 2018. https://news.mit.edu/2018/explaining-dropping-solar-cost-1120.

[30] Christophe Ballif, Franz-Josef Haug, Mathieu Boccard, Pierre J Verlinden, and Giso Hahn. Status and perspectives of crystalline silicon photovoltaics in research and industry. *Nature Reviews Materials*, 7(8):597–616, 2022.

[31] Armin Richter, Ralph Müller, Jan Benick, Frank Feldmann, Bernd Steinhauser, Christian Reichel, Andreas Fell, Martin Bivour, Martin Hermle, and Stefan W Glunz. Design rules for high-efficiency both-sides-contacted silicon solar cells with balanced charge carrier transport and recombination losses. *Nature Energy*, 6(4):429–438, 2021.

[32] Mark Elliott, Michael McIntyre, Joseph Lathan, and Steven Tidwell. Partial shading abatement through cell level inverter system topology. In *2015 IEEE 42nd Photovoltaic Specialist Conference (PVSC)*, pages 1–5. IEEE, 2015.

[33] Alivarani Mohapatra, Byamakesh Nayak, Priti Das, and Kanungo Barada Mohanty. A review on mppt techniques of pv system under partial shading condition. *Renewable and Sustainable Energy Reviews*, 80:854–867, 2017.

[34] Soubhagya K Das, Deepak Verma, Savita Nema, and RK Nema. Shading mitigation techniques: State-of-the-art in photovoltaic applications. *Renewable and Sustainable Energy Reviews*, 78: 369–390, 2017.

[35] David A. van Nijen, Mirco Muttillo, Rik Van Dyck, Jef Poortmans, Miro Zeman, Olindo isabella, and Patrizio Manganiello. Revealing capacitive and inductive effects in modern industrial c-si photovoltaic cells trough impedance specroscopy. 2023.

[36] Girish Kumar Singh. Solar power generation by pv (photovoltaic) technology: A review. *Energy*, 53:1–13, 2013.

[37] Wafa Hayder, Aicha Abid, and Mouna Ben Hamed. Steps of duty cycle effects in po mppt algorithm for pv system. In *2017 International Conference on Green Energy Conversion Systems (GECS)*, pages 1–4. IEEE, 2017.

[38] Ashish Pandey, Nivedita Dasgupta, and Ashok K Mukerjee. A simple single-sensor mppt solution. *IEEE Transactions on Power Electronics*, 22(2):698–700, 2007.

[39] Azadeh Safari and Saad Mekhilef. Simulation and hardware implementation of incremental conductance mppt with direct control method using cuk converter. *IEEE transactions on industrial electronics*, 58(4):1154–1161, 2010.

[40] S Sivakumar, M Jagabar Sathik, PS Manoj, and G Sundararajan. An assessment on performance of dc-dc converters for renewable energy applications. *Renewable and Sustainable Energy Reviews*, 58:1475–1485, 2016.

[41] Juan C Hernandez, Lars P Petersen, and Michael AE Andersen. A comparison between boundary and continuous conduction modes in single phase pfc using 600v range devices. In *2015 IEEE 11th International Conference on Power Electronics and Drive Systems*, pages 1019–1023. IEEE, 2015.

[42] Zachariach Peterson. Continuous conduction mode in an smps: What is it and why it matters, 2021. `https://resources.altium.com/p/continuous-conduction-mode-smps-what-it-and-why-it-matters`.

[43] All About Ciruits. Discontinuous conduction mode of simple converters, 2015. https://www.allaboutcircuits.com/technical-articles/discontinuous-conduction-mode-of-simple-converters/: :text=Having

[44] Wei Gu and Dongbing Zhang. Designing a sepic converter. *Excellent design guidelines, national semiconductor in application note*, pages 1–6, 2008.

[45] Ned Mohan, Tore M Undeland, and William P Robbins. *Power electronics: converters, applications, and design*. John wiley & sons, 2003.

[46] Muhammad H Rashid. *Power electronics handbook*. Butterworth-heinemann, 2017.

[47] Xiaotong Du, Chengmin Li, and Dražen Dujić. Design and characterization of pcb spiral coils for inductive power transfer in medium-voltage applications. *IEEE Transactions on Power Electronics*, 37(5):6168–6180, 2021.

[48] Fares Tounsi, Mohamed Hadj Said, Margo Hauwaert, Sinda Kaziz, Laurent A Francis, Jean-Pierre Raskin, and Denis Flandre. Variation range of different inductor topologies with shields for rf and inductive sensing applications. *Sensors*, 22(9):3514, 2022.

[49] Wanchun Tang, Yaning Zhu, and Y Leonard Chow. Inductance calculation of spiral inductors in different shapes. In *2005 Asia-pacific Microwave Conference Proceedings*, volume 5, pages 3–pp. IEEE, 2005.

[50] Monica Zolog, Dan Pitica, and Ovidiu Pop. Characterization of spiral planar inductors built on printed circuit boards. In *2007 30th International Spring Seminar on Electronics Technology (ISSE)*, pages 308–313. IEEE, 2007.

[51] Andreia Faria, Luís Marques, Carlos Ferreira, Filipe Alves, and Jorge Cabral. A fast and precise tool for multi-layer planar coil self-inductance calculation. *Sensors*, 21(14):4864, 2021.

[52] Rabia Melati, Azzedine Hamid, Lebey Thierry, and Mokhtaria Derkaoui. Design of a new electrical model of a ferromagnetic planar inductor for its integration in a micro-converter. *Mathematical and Computer Modelling*, 57(1-2):200–227, 2013.

[53] Minh Huy Nguyen and Handy Fortin Blanchette. Optimizing ac resistance of solid pcb winding. *Electronics*, 9(5):875, 2020.

[54] Lourdes Abdilla, Louis Zammit Mangion, and Charles V. Sammut. Eddy current sensing using planar coils. *IEEE Instrumentation Measurement Magazine*, 15(6):14–18, 2012. doi: 10.1109/MIM.2012.6365537.

[55] PLEXIM. Plecs products, 2023. https://www.plexim.com/products/plecs.

[56] Jim Voorn. Feasibility study on the implementation of planar inductors onto c-si solar cells through numerical simulations. http://repository.tudelft.nl/.

[57] COMSOL Multiphysics. About comsol, 2018. https://www.comsol.com/company.

[58] K Kawabe, H Koyama, and K Shirae. Planar inductor. *IEEE Transactions on Magnetics*, 20(5): 1804–1806, 1984.

[59] Charles Marfo Awuah, Patrick Danuor, Jung-Ick Moon, and Young-Bae Jung. Novel coil design and analysis for high-power wireless power transfer with enhanced q-factor. 2023.

[60] Abasifreke Ebong and Nian Chen. Metallization of crystalline silicon solar cells: A review. *High Capacity Optical Networks and Emerging/Enabling Technologies*, pages 102–109, 2012.

[61] Han Cui, Khai DT Ngo, Jim Moss, Michele Hui Fern Lim, and Ernesto Rey. Inductor geometry with improved energy density. *IEEE Transactions on Power Electronics*, 29(10):5446–5453, 2013.

[62] COMSOL Multiphysics. Infinite element domain, . https://doc.comsol.com/5.5/doc/com.comsol.help.comsol/comsol_ref_definitions.12.116.html.

[63] COMSOL Learning Center. Adding the physics, . https://www.comsol.com/learning-center/assigning-physics-to-a-model-geometry-in-comsol-multiphysics.

[64] COMSOL Multiphysics. Magnetic fields interface, . https://doc.comsol.com/5.5/doc/com.comsol.help.comsol/comsol_ref_acdc.17.67.html.

[65] COMSOL Multiphysics. Magnetic insulation, . https://doc.comsol.com/5.5/doc/com.comsol.help.comsol/comsol_ref_acdc.17.74.html.

[66] COMSOL Multiphysics. Gauge fixing for a-field, . https://doc.comsol.com/5.5/doc/com.comsol.help.acdc/acdc_ug_magnetic_fields.08.018.html.

[67] COMSOL Learning Center. Building the mesh, . https://www.comsol.com/learning-center/building-the-mesh-for-a-model-geometry-in-comsol-multiphysics.

[68] Praful V Nandankar, Prashant P Bedekar, and Prashant Kumar V Dhawas. Variable switching frequency control for efficient dc-dc converter. *Materials Today: Proceedings*, 51:515–521, 2022.

[69] TDK Lambda Americas. Dc-dc converter switching frequencies – fixed or variable?, 2022. https://www.us.lambda.tdk.com/resources/blogs/20220425.html: :text=DC

[70] Yasutaka Fukuda, Tetsuo Inoue, Tetsuhiko Mizoguchi, Shigeru Yatabe, and Yoshihito Tachi. Planar inductor with ferrite layers for dc-dc converter. *IEEE Transactions on Magnetics*, 39(4):2057–2061, 2003.

[71] T. Editors of Encyclopaedia Britannica. skin effect, 2018. https://www.britannica.com/science/skin-effect.

[72] Joseph George Coffin. *The influence of frequency upon the self-inductance of coils*. Number 37. Acad., 1906.

[73] Jingying Hu, Anthony D Sagneri, Juan M Rivas, Yehui Han, Seth M Davis, and David J Perreault. High-frequency resonant sepic converter with wide input and output voltage ranges. *IEEE Transactions on Power Electronics*, 27(1):189–200, 2011.

[74] Ali Bughneda, Mohamed Salem, Mohammad Alhuyi Nazari, Dahaman Ishak, Mohamad Kamarol, and Salah Alatai. Resonant power converters for renewable energy applications: A comprehensive review. *Frontiers in Energy Research*, 10:185, 2022.

[75] Analog Devices. Ltspice, 2023. `https://www.analog.com/en/design-center/design-tools-and-calculators/ltspice-simulator.html`.

A

Resonant Boost Converters - Preliminary Results

Many advancements have been made in power electronics to improve power devices and to new converter topologies and control technologies. Conventional pulse width modulation converters were used for switch mode power supply (SMPS). The power switches have to cut off the load current when switching between turning 'ON' and 'OFF' under hard switching conditions(stressful switching behaviors). During this hard switching, the power electronics must withstand high voltage and current simultaneously, leading to increased switching losses. Thus to reduce the switching losses, resonant tanks (figure A.1) can be added to the converter, generating sinusoidal voltage and current waveforms. This results in achieving zero-voltage/current switching (ZVS/ZCS). These switching conditions allow the converter to operate at a switching frequency of more than 1MHz leading to less switching losses and smaller passive components size. However, they show some desirable problems like higher V&I rating requirements for the devices and the use of an additional frequency modulator for output regulation. This makes the circuit design and control complex.[46]

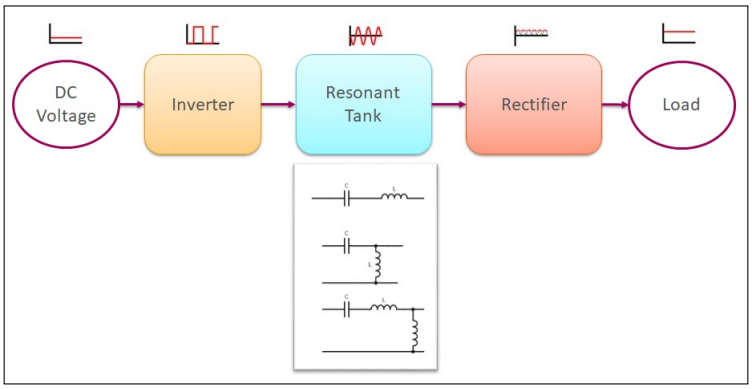

Figure A.1: DC-DC Resonant Converter

Soft-switching was designed to replace the traditional hard switching in SMPS. These soft-switched converters combined the benefits of conventional PWM converters and resonant converters. Soft-switched converters utilized the resonance in a controlled manner, thus removing the transient spikes in V & I waveform. This converter allowed the resonance to occur moments before and during the transition of the switch between ON-OFF, thus creating the conditions of ZVS and ZCS.[73]

Before the introduction of modern power switches, thyristors were used in power electronic circuits. Thyristors require a commutation circuit which consists of an LC resonance circuit, forcing the current to zero in the OFF state. Recent advancements have seen GTOs and IGBT replace thyristors and provide better V&I handling capabilities and controllability for high switching speed[46].

A resonant switch is a sub-circuit that consists of resonant inductors and capacitors. Based on the voltage/current control, its classified into two types a zero current resonant switch (ZC switch) and a zero voltage resonant switch (ZV switch).

The objective of the ZC switch is to control the switch current waveform using the L-C subcircuit in order to create zero current conditions for the switch to turn 'OFF.' When the switch is "ON, the current in the switch rises from zero and then oscillates in the resonance tank of L-C. Later, the switch can be turned 'OFF' during the next zero current.[46]. The objective of the ZV switch is to control the switch voltage waveform using the L-C resonant tank in order to create zero-voltage conditions for the switch to turn 'ON.'[46].

In the last few decades, many soft-switching converters have been developed. These converters have made the power semiconductors (switches, diodes) operate at higher frequencies, thus requiring smaller-sized passive elements. This consequently resulted in higher performance and better efficiency. Many families of resonant converters like quasi-multi resonant converters, resonant-transition converters,s and resonant power converters (RPCs) [74]. For this thesis, the main focus is given to the resonant power converter topology as it uses less amount of electrical elements. RPCs have grown in popularity in industrial use due to their benefits, like minimal switching losses, high power density, and requiring smaller passive elements, making them ideal for use for MEMS & NEMS applications.

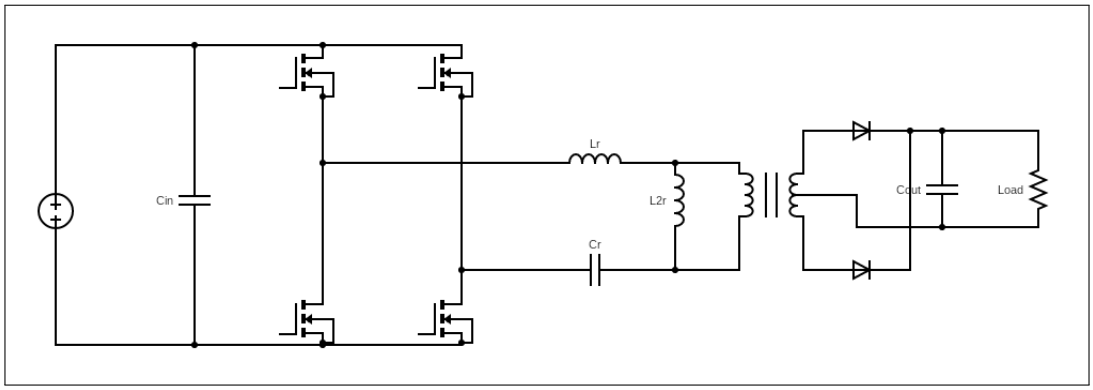

Figure A.2: LLC resonant tank DC-DC converter[23]

Figure A.2 portrays a conventional design of an LLC resonant converter. This topology uses a full-bridge inverter which converts the PV DC voltage to an AC signal. This AC signal is transferred to an LLC resonant tank which steps up/down the voltage level. Later, the elevated AC voltage signal is sent to a rectifier to transform it into a DC signal. The advantage of the LLC resonant tank is the variable duty-cycle control method, making it ideal for PV systems for MPPT algorithm- Duty cycle adjustment. However, this topology of the resonant converter is not suitable for partial integration into a solar cell as this resonant circuit does not have any inductor in the front section like a boost converter for direct series connection with solar cells. Thus, a different topology of the resonant circuit is investigated, which uses passive components L and C for inverter and rectifier operations.

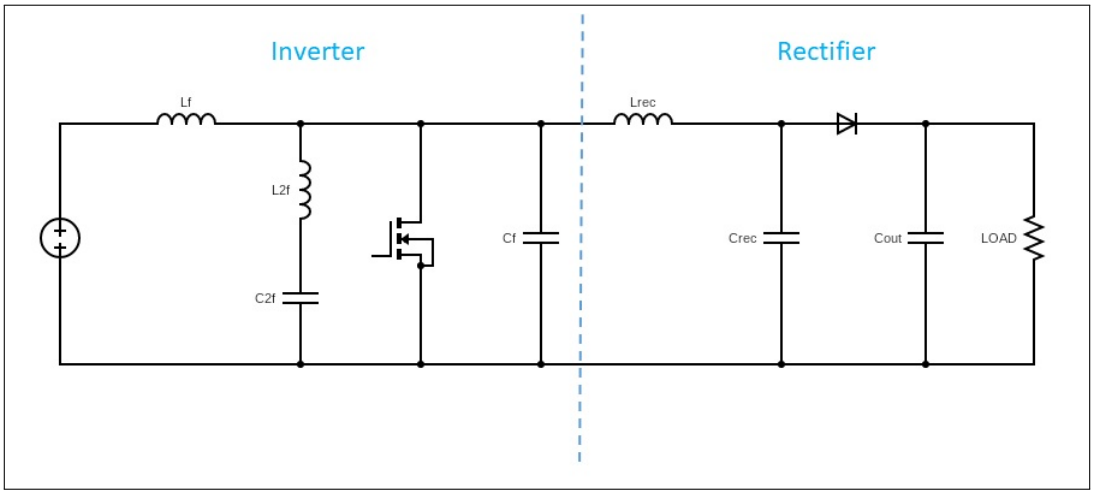

Figure A.3: schematic of resonant DC-DC converter[17]

Pilawa et al., [17] proposed a new resonant boost converter topology that uses pairs of passive elements to function as inverters and rectifiers. The converter for this work is designed to operate at a very high frequency (30-300MHz) and thus requires small-sized passive elements. The schematic of the converter is shown in figure A.3. This design uses a multi-resonant network- L_F, L_{2F}, C_F, and C_{2F}. This network transforms the input signal into a quasi-square/ trapezoid waveform across the drain-source to achieve zero-voltage switching. The square waveform will reduce the peak voltage stress across the switch to as low as two times of input signal. The tuning of the components used in multi-network circuits is done using the equations

$$L_F = \frac{1}{9 * \pi^2 * {F_{sw}}^2 * C_F}; L_{2F} = \frac{1}{15 * \pi^2 * {F_{sw}}^2 * C_F}; C_{2F} = \frac{15}{16} * C_F \tag{A.1}$$

C_F is the design factor for this topology as other components like L_F, L_{2F}, and C_{2F} are designed using it. The inverter is coupled with the rectifier, which uses an LC filter to transform the square pulse generated by the inverter into a DC signal. To utilize the solar cell self-inductance, it is important to design a DC-DC converter with compatible inductance requirements. From the previous section, it was seen that it becomes challenging to design a conventional DC-DC converter with an inductor requirement in the range of 50nH. To overcome this issue, a different type of converter topology is studied, a resonant converter that has the upper hand over conventional converters mainly due to the soft-switching technique. The resonant converter uses a resonant tank which allows the converter to perform soft-switching resulting in minimal switching losses. Due to this, the resonant converter is favorable for high switching frequency operations, which allows the designing of the converter with a small-sized inductor. In the following subsections, a resonant converter design suggested in [17] is realized. The resonant converter is designed for a string of 13 cells and thus uses the electrical parameters mentioned in table 4.1. **Sizing of the resonant converter** The resonant converter design proposed in [17] uses a two L-C resonant tank. Figure A.4 displays a schematic of a resonant boost converter circuit proposed by [17]. The main focus while using the converter is given towards the inductor 'L_1'. Equations A.1 are used to tune the size of all passive elements used in inverter design. The tuning equations show their dependency on the size of capacitor C_F. Thus, capacitor C_F is an important parameter for sizing other elements.

Resonant Converter Realization

A resonant converter is a complex circuit design that uses multiple resonant tanks. Due to the presence of resonant tanks, it is not a good choice to use ideal components for the design as it becomes difficult to realize the resonance waveform. Thus, the resonant converter is designed in a different software known LTspice. LTspice, also called Linear Technology Simulation Program with Integrated Circuit Emphasis, is a powerful simulator software used for schematic capture, waveform viewer with enhancements, and models for improving the simulations of electrical circuits. It is graphical schematic capture interface

allows the user to probe the schematics and produce simulations which can be further explored using a built-in waveform viewer [75].

LTspice consists of the library, which includes real-world components of active, passive, and semiconductor elements used in the electric circuit. This allows the feature of studying the no-ideal characteristics of power conversion electric circuits.

The converter design proposed in [17] uses a switching frequency of 110MHz, thus requiring very small-sized passive elements. But with high frequency, AC resistance due to skin effect plays a major role in power losses. Thus, a different-sized converter model is required at a lower frequency to diminish the skin effect.

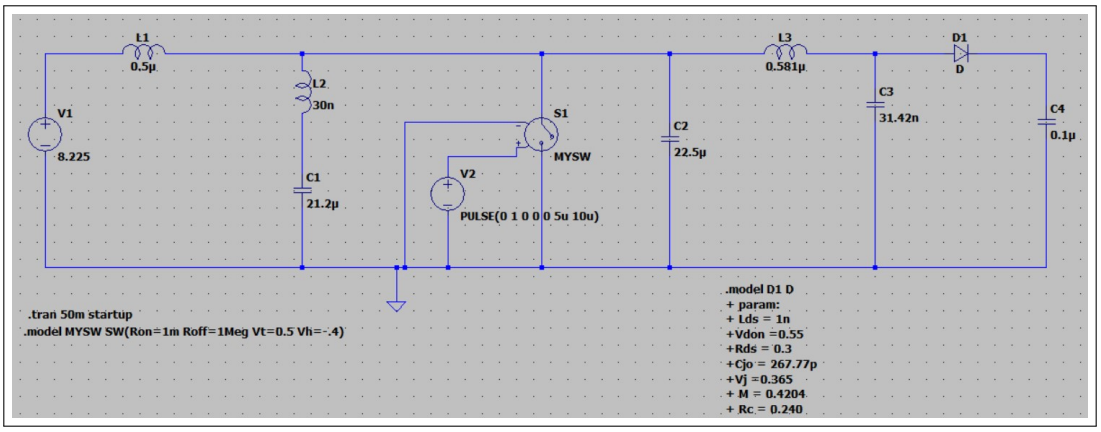

Figure A.4: Resonant Boost converter operating at F_{SW} of 100KHz

Figure A.4 shows a schematic of a resonant boost converter operating at F_{SW} of 100kHz. The same resonant boost converter proposed in [17] is designed but with table 3.1 parameters. LTspice software is used to understand the accurate reflection of the converter dynamics by using the non-ideal components in the circuit. The two resonant networks (L_F-C_F, L_{2F}-C_{2F}) enable the use of resonant gating and zero-voltage switching at 100kHz frequency. As discussed previously, a resonant converter is an interconnection of an inverter and rectifier; thus, both the sub-circuits, inverter, and rectifier are first designed separately and then inter-connected by impedance matching to result in the formation of the resonant boost converter.

Rectifier Design

The inverter is coupled to a resonant rectifier, as shown in figure A.1. The rectifier is designed first so that the substitution of the tuned rectifier for the inverter's load resistance can be done with the least effect on the inverter's performance [17]. Rectifier design is created in simulation programs such as SPICE. As the significant bulk of the circuit is present at the inverter side, at the rectifier input, two source model is used to mimic the output voltage produced by the inverter's drain-source terminals. Considering that the converter is 100% efficient, the input voltage is modeled by a sinusoidal source with the amplitude equal to the maximum of the inverter's drain-source voltage and DC off-set equal to V_{in}[17].

Several additional aspects, like inductors equivalent series resistance(ESR) and capacitance ESR/inductive behavior, were considered while designing the model to add accuracy to the simulation. This will help to capture the dynamics of rectifier operation. The sizing of the inductor and capacitor is done by fixing the center frequency (ω_o) at switching frequency F_{SW} (100kHz) and the impedance (Z) of 4.3Ω. Using the equations A.2, the values of L_1,C_1 and C_2.

$$F_{SW} = \frac{1}{2 * \pi * \sqrt{L * (C_1 + C_2)}}; Z = \sqrt{\frac{L}{C_1 + C_2}} \tag{A.2}$$

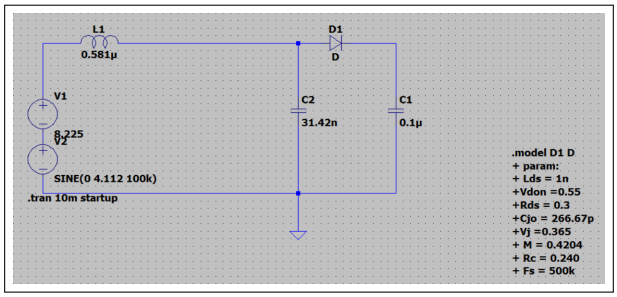

Figure A.5: schematic of resonant rectifier operating at F_{SW} of 500kHz

Inverter Design

The inverter needs to deliver the required AC power to the load resistance (Rectifier circuit). The inverter is designed the same as the figure A.3 and is shown in figure 1.6

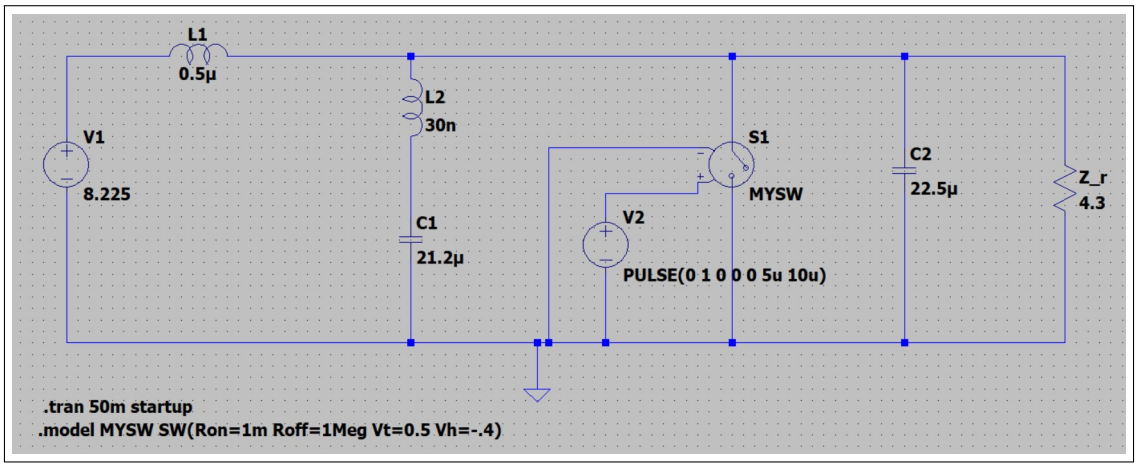

Figure A.6: schematic of resonant inverter operating at F_{SW} of 500kHz

Figure A.7 shows the voltage at the drain-source terminal of the inverter. It can be observed that the shape of the voltage is a trapezoid or square-like structure also at a lower peak (almost at 3.5 times in the source voltage). Also, the waveform reaches zero voltage values, making it capable of soft-switching.

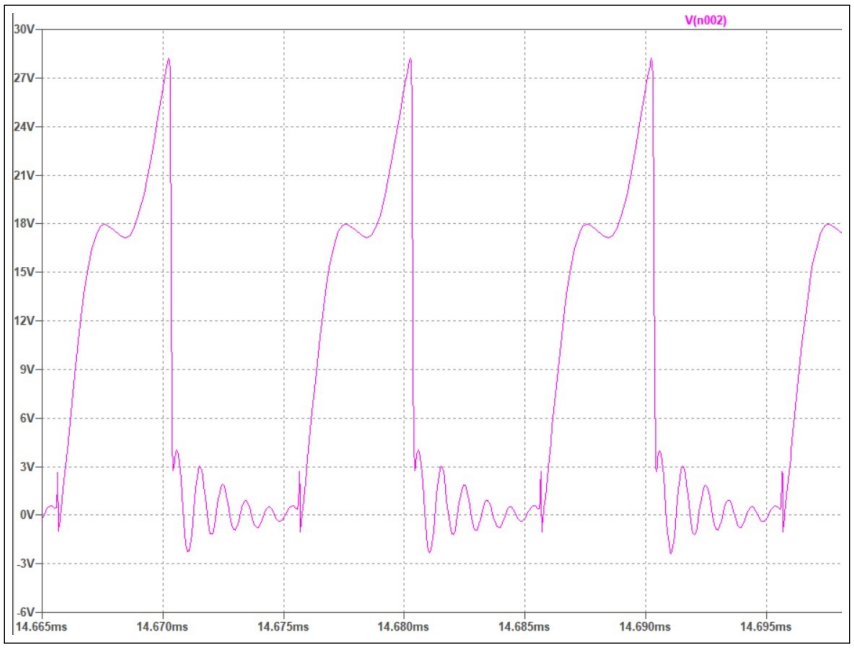

Figure A.7: waveform of drain-source voltage of an inverter

Final Converter realization

Once the inverter design is finalized, connecting the rectifier design with the inverter results in a total power loss to the desired power requirement. Figure A.4 shows the finalized resonant boost converter design. The drain-source voltage and output voltage of the resonant boost converter are shown in figure A.8a & A.8b. It is important to mention that this converter design does not comprise the use of a gate driver and a control strategy. To vary the duty cycle and reduce any current peaks at the switch terminal, it is important to use a gate driver and control as proposed by [17].

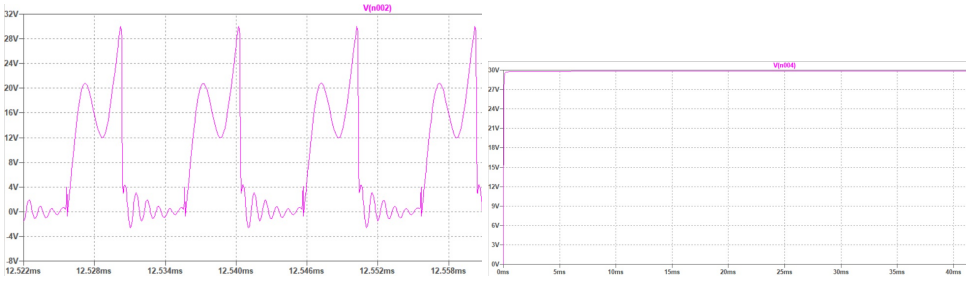

(a) (b)

Figure A.8: (a) Drain-source voltage of resonant converter at F_{SW} 500kHz (b) Output voltage of the resonant converter

B

Planar Coil - Geometry

Geometry of Coil with 2 and 4 turns

The following table B.1 shows the geometry of the 2Turn and 4Turn coils. The xw and yw represent the X-Y axis coordinates of the edges of the apology used to derive the structure.

Table B.1: Geometry of coil with 2Turns and 4Turns

2-Turn			**4-Turn**	
xw	*yw*		*xw*	*yw*
-L/2+2*w+s	L/2-2*w-2*s		-L/2+4*w+3*s	L/2 -4*s-4*w
-L/2+2*w+s	-L/2+2*w+s		-L/2+4*w+3*s	-(L/2 -3*s-4*w)
L/2-2*w-s	-L/2+2*w+s		-(-L/2+4*w+3*s)	-(L/2 -3*s-4*w)
L/2-2*w-s	L/2-2*w-2*s		-(-L/2+4*w+3*s)	L/2 -3*s-4*w
-L/2+w	L/2-2*w-2*s		-L/2+3*w+2*s	L/2 -3*s-4*w
-L/2+w	L/2+w		-L/2+3*w+2*s	-L/2+3*w+2*s
L/2-w	L/2+w		-(-L/2+3*w+2*s)	-L/2+3*w+2*s
L/2-w	L/2-w		-(-L/2+3*w+2*s)	L/2 -2*s-3*w
-L/2+2*w+2*s	L/2-w		-L/2+2*w+s	L/2 -2*s-3*w
-L/2+2*w+2*s	L/2		-L/2+2*w+s	-(L/2 -2*w-s)
L/2	L/2		-(-L/2+2*w+s)	-(L/2 -2*w-s)
L/2	-L/2		-(-L/2+2*w+s)	L/2 -2*w-s
-L/2	-L/2		-L/2+w	L/2 -2*w-s
-L/2	L/2-w		-L/2+w	L/2-w
L/2-w	L/2-w		L/2-w	L/2-w
L/2-w	-L/2+w		L/2-w	L/2-w
L/2-w+s	-L/2+w		-L/2+3*w+3*s	L/2-w
L/2-w+s	-L/2+2*w+s		-L/2+3*w+3*s	L/2
			L/2	L/2
			L/2	-L/2
			-L/2	-L/2
			-L/2	L/2-w-s
			L/2-w-s	L/2-w-s
			L/2-w-s	-L/2+w+s
			-(L/2-w-s)	-L/2+w+s
			-(L/2-w-s)	L/2-2*w-2*s
			L/2-2*w-2*s	L/2-2*w-2*s
			L/2-2*w-2*s	-L/2+2*w+2*s
			-(L/2-2*w-2*s)	-L/2+2*w+2*s
			-(L/2-2*w-2*s)	L/2-3*w-3*s

Table B.1 continued from previous page

2-Turn			4-Turn	
			L/2-3*w-3*s	L/2-3*w-3*s
			L/2-3*w-3*s	-L/2+3*w+3*s
			-(L/2-3*w-3*s)	-L/2+3*w+3*s
			-(L/2-3*w-3*s)	L/2 -4*s-4*w

Gap

Table B.2 shows the width's dependency on the coil's gap parameter. From equation 3.2, it can be realized at a fixed spacing of 4mm; with increasing gap parameters, the width of the coil reduces. This effect can be seen in all planar coils (with 3, 4, and 5 Turns). As physically it is not possible to have a negative value for width, the gap parameter is varied until the least positive width value is achieved. This is the parametric sweep in the simulation study.

Table B.2: with of the wire at different gap parameters

width(mm) for different turns at fixed s=4mm			
gap(cm)	3	4	5
0.5	17.33	12	8.8
1	16.5	11.38	8.3
1.5	15.67	10.75	7.8
2	14.83	10.125	7.3
2.5	14	9.5	6.8
3	13.17	8.88	6.3
3.5	12.33	8.25	5.8
4	11.5	7.63	5.3
4.5	10.67	7	4.8
5	9.83	6.38	4.3
5.5	9	5.75	3.8
6	8.17	5.13	3.3
6.5	7.33	4.5	2.8
7	6.5	3.88	2.3
7.5	5.67	3.25	1.8
8	4.83	2.63	1.3
8.5	4	2	0.8
9	3.17	1.38	0.3
9.5	2.33	0.75	-0.2
10	1.5	0.13	-0.7
10.5	0.67	-0.5	-1.2
11	-0.17	-1.13	-1.7

Width

Similarly to the gap, the spacing parameter of the coil is again inversely proportional to the width of the wire. Thus the table below shows the width of coils with 3, 4, and 5 turns at different spacings. The wire's width in the coil is essential for studying the skin effect.

Table B.3: with of the wire at different spacing parameters

width(mm) for different turns with fixed g=2cm			
spacing(mm)	3	4	5
0,5	17,17	12,75	10,1
1	16,83	12,38	9,7
1,5	16,5	12	9,3
2	16,17	11,63	8,9
2,5	15,83	11,25	8,5
3	15,5	10,88	8,1
3,5	15,17	10,5	7,7
4	14,83	10,13	7,3
4,5	14,5	9,75	6,9
5	14,17	9,38	6,5
5,5	13,83	9	6,1
6	13,5	8,63	5,7
6,5	13,17	8,25	5,3
7	12,83	7,88	4,9
7,5	12,5	7,5	4,5
8	12,17	7,13	4,1
8,5	11,83	6,75	3,7
9	11,5	6,38	3,3
9,5	11,17	6	2,9
10	10,83	5,63	2,5
10,5	10,5	5,25	2,1
11	10,17	4,88	1,7
11,5	9,83	4,5	1,3
12	9,5	4,13	0,9
12,5	9,17	3,75	0,5
13	8,83	3,38	0,1
13,5	8,5	3	-0,3
14	8,17	2,63	-0,7
14,5	7,83	2,25	-1,1
15	7,5	1,88	-1,5
15,5	7,17	1,5	-1,9
16	6,83	1,13	-2,3
16,5	6,5	0,75	-2,7
17	6,17	0,38	-3,1
17,5	5,83	0	-3,5
18	5,5	-0,38	-3,9
18,5	5,17	-0,75	-4,3
19	4,83	-1,13	-4,7
19,5	4,5	-1,5	-5,1
20	4,17	-1,88	-5,5
20,5	3,83	-2,25	-5,9
21	3,5	-2,63	-6,3
21,5	3,17	-3	-6,7
22	2,83	-3,38	-7,1
22,5	2,5	-3,75	-7,5
23	2,17	-4,13	-7,9
23,5	1,83	-4,5	-8,3
24	1,5	-4,88	-8,7
24,5	1,17	-5,25	-9,1
25	0,83	-5,63	-9,5
25,5	0,5	-6	-9,9
26	0,17	-6,38	-10,3
26,5	-0,17	-6,75	-10,7
27	-0,5	-7,13	-11,1
27,5	-0,83	-7,5	-11,5

C

Effect of mesh element size on results

Meshing is an important aspect when working with COMSOL software. Meshing helps in segregating the complete model into smaller elements which later are solved by the software using partial differential equations. Thus having more mesh elements of the model, the higher the accuracy of the output results.

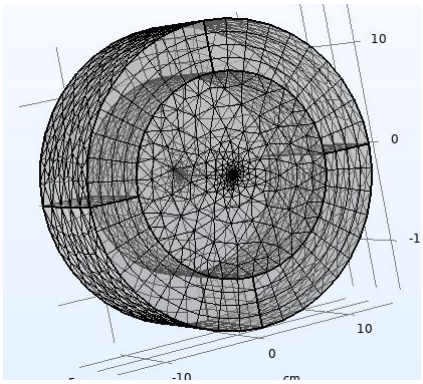

Figure C.1: Complete mesh of a single circular wire encapsulated inside a cylinder

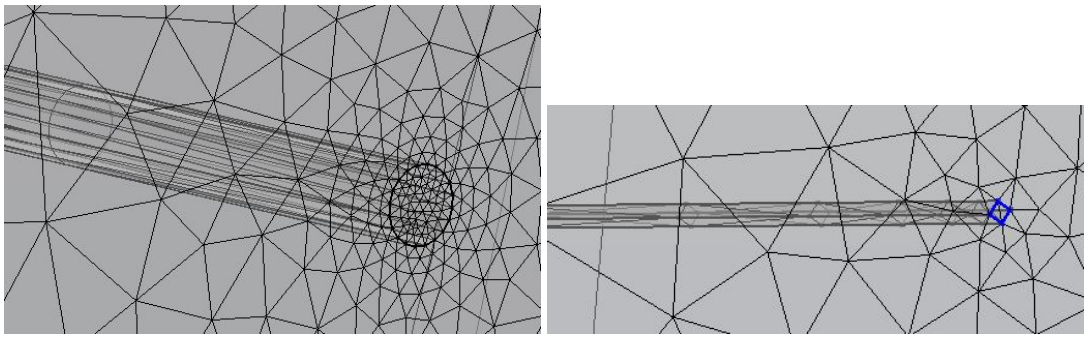

(a) (b)

Figure C.2: Meshing the face of the circular wire using (a) User-Controlled Mesh (b) Normal-controlled Fine mesh

To prove this, electrical parameters like the resistance and inductance of a straight current-carrying coil are studied in the frequency domain. Figure C.1 shows a fully meshed circular wire encapsulated inside a cylinder. The COMSOL meshing toolkit provides two types of meshing: User-controlled meshing, where mesh element size is decided by the user, and Normal-Controlled meshing, where the software itself meshes the model. Figure C.2a represents a user-controlled mesh of circular wire. Using various toolkits available in COMSOL's Mesh tab, an extremely fine-meshed model can be created where

the point of interest in the model has been heavily meshed to achieve accurate results. Whereas in normal-controlled meshing, there is a set of options pre-defined by the software for meshing the model. Figure C.2b shows a low-scaled meshing. Both methods generate the same mesh elements; however, unlike the user-controlled mesh, the normal-controlled mesh keeps the same mesh element size for the complete model. Thus decreasing the accuracy of the results.

Table C.1: Planar coil Inductance and resistance value at 0.2 maximum element size

0.2 maximum element size				
s (mm)	freq (Hz)	Coil resistance (DC) (mΩ)	Coil inductance (uH)	rising factor
0.4	1	3.4084	1.0581	
	1000	3.6589	1.0483	1.07
	10000	10.3325	0.9154	3.03
	100000	62.0363	0.7235	18.20
	500000	82.8672	0.6760	24.31
0.5	1	3.4305	1.0580	
	1000	3.6757	1.0484	1.07
	10000	10.1630	0.9173	2.96
	100000	54.9729	0.7380	16.02
	500000	71.3826	0.6991	20.81
1	1	3.5447	1.0574	
	1000	3.7656	1.0489	1.06
	10000	9.4018	0.9276	2.65
	100000	35.4329	0.7951	10.00
	500000	42.9318	0.7758	12.11
2.5	1	3.9339	1.0595	
	1000	4.0960	1.0537	1.04
	10000	8.2734	0.9600	2.10
	100000	21.6123	0.8764	5.49
	500000	25.2331	0.8673	6.41
4	1	4.4089	1.0655	
	1000	4.5273	1.0617	1.03
	10000	7.9423	0.9894	1.80
	100000	18.0956	0.9218	4.10
	500000	20.8841	0.9152	4.74
5	1	4.7894	1.0721	
	1000	4.8847	1.0693	1.02
	10000	7.8945	1.0090	1.65
	100000	16.9377	0.9483	3.54
	500000	19.2220	0.9425	4.01

Table C.1 and Table C.2 have been realized by simulating the circular wire with a maximum element size of 0.2 and 0.3, respectively. Comparing the results of the two tables, it can be observed that the values with element size 0.2 are higher than those with element size 0.3, especially at high frequencies where the point of interest, the skin effect, plays a significant role. Thus, this highlights that the effects from higher frequencies are more visible in the results by using a higher degree of meshing.

Table C.2: Planar coil Inductance and resistance value at 0.2 maximum element size

0.3 maximum element size				
s (mm)	freq (Hz)	Coil resistance (DC) (mΩ)	Coil inductance (uH)	rising factor
0.4	1	3.4009	1.0513	
	1000	3.6571	1.0419	1.08
	10000	11.3634	0.9036	3.34
	100000	59.3451	0.6762	17.45
	500000	71.2853	0.6432	20.96
0.5	1	3.4228	1.0510	
	1000	3.6738	1.0419	1.07
	10000	11.2198	0.9052	3.28
	100000	54.3311	0.6894	15.87
	500000	64.2367	0.6610	18.77
1	1	3.5369	1.0503	
	1000	3.7636	1.0422	1.06
	10000	10.3471	0.9152	2.93
	100000	38.1834	0.7512	10.80
	500000	44.0805	0.7344	12.46
2.5	1	3.9251	1.0510	
	1000	4.0900	1.0455	1.04
	10000	8.7938	0.9472	2.24
	100000	21.3584	0.8529	5.44
	500000	24.0998	0.8459	6.14
4	1	4.3983	1.0558	
	1000	4.5186	1.0523	1.03
	10000	8.4198	0.9757	1.91
	100000	17.3239	0.9014	3.94
	500000	19.2561	0.8965	4.38
5	1	4.7771	1.0597	
	1000	4.8743	1.0571	1.02
	10000	8.3672	0.9929	1.75
	100000	16.0076	0.9259	3.35
	500000	17.7145	0.9218	3.71

D

Inductance and Resistance values of Coil- 2, 3, and 5

This appendix shows the inductance and resistance values of the planar coil design achieved through simulation results. The following sections show the results of planar coils with 2-turns, 3-Turns, and 5-Turns (4-Turn is shown in the main text). All these results were used to obtain different planar coil combinations to answer the last research question in chapter 5. Each section displays the effect on the coil's electrical performance due to varying coil parameters like spacing and gap size.

Planar Coil with 2 Turns

Table D.1: Effect on the resistance and inductance of 2-Turn coil due to varying spacing between the coils(s)

s (mm)	freq (Hz)	Coil resistance (DC) (mΩ)	Coil inductance (uH)
0.4	1	0.7393	0.2406
	1000	0.9013	0.2271
	10000	2.9800	0.1691
	100000	8.1225	0.1275
	200000	8.7569	0.1256
0.5	1	0.7418	0.2409
	1000	0.9017	0.2275
	10000	2.9233	0.1703
	100000	7.5080	0.1312
	200000	8.0915	0.1296
0.75	1	0.7479	0.2412
	1000	0.9052	0.2283
	10000	2.8326	0.1714
	100000	6.6036	0.1369
	200000	7.1253	0.1355
1	1	0.7546	0.2421
	1000	0.9071	0.2295
	10000	2.6910	0.1750
	100000	6.2383	0.1434
	200000	6.7359	0.1420
1.25	1	0.7611	0.2428
	1000	0.9101	0.2305
	10000	2.6266	0.1770
	100000	5.8872	0.1474
	200000	6.3716	0.1462
1.5	1	0.7676	0.2434

Table D.1 continued from previous page

s (mm)	freq (Hz)	Coil resistance (DC) (mΩ)	Coil inductance (uH)
	1000	0.9134	0.2315
	10000	2.5770	0.1790
	100000	5.6546	0.1507
	200000	6.1122	0.1495
	1	0.7738	0.2436
	1000	0.9171	0.2321
1.75	10000	2.5795	0.1796
	100000	5.1967	0.1531
	200000	5.6085	0.1521
	1	0.7803	0.2440
	1000	0.9211	0.2329
2	10000	2.5440	0.1805
	100000	4.7944	0.1562
	200000	5.1777	0.1553
	1	0.7941	0.2453
	1000	0.9289	0.2348
2.5	10000	2.4527	0.1844
	100000	4.4733	0.1623
	200000	4.8396	0.1615
	1	0.8023	0.2461
	1000	0.9336	0.2360
2.8	10000	2.4103	0.1868
	100000	4.3949	0.1653
	200000	4.7668	0.1646
	1	0.8080	0.2466
	1000	0.9369	0.2367
3	10000	2.3759	0.1883
	100000	4.2654	0.1677
	200000	4.6132	0.1669
	1	0.8231	0.2480
	1000	0.9464	0.2387
3.5	10000	2.3075	0.1921
	100000	4.0703	0.1730
	200000	4.4106	0.1723
	1	0.8382	0.2492
	1000	0.9569	0.2404
4	10000	2.2968	0.1950
	100000	4.0112	0.1762
	200000	4.3346	0.1755
	1	0.8541	0.2506
	1000	0.9680	0.2423
4.5	10000	2.2729	0.1982
	100000	3.9148	0.1800
	200000	4.2169	0.1793
	1	0.8704	0.2521
	1000	0.9799	0.2443
5	10000	2.2500	0.2013
	100000	3.7632	0.1839
	200000	4.0499	0.1833

Table D.2: Effect on the resistance and inductance of 2-Turn coil due to varying gap size between the coil(g)

g (cm)	freq (Hz)	Coil resistance (DC) (mΩ)	Coil inductance (uH)
2	1	0.8129	0.2449
	10000	1.9664	0.1945
	100000	4.3835	0.1781
	200000	4.8665	0.1769
	500000	5.2460	0.1764
3	1	0.9897	0.3005
	10000	2.1261	0.2540
	100000	4.5792	0.2373
	200000	5.0626	0.2361
	500000	5.4503	0.2356
4	1	1.2117	0.3626
	10000	2.3348	0.3201
	100000	4.8725	0.3031
	200000	5.3865	0.3019
	500000	5.8309	0.3013
6	1	1.8888	0.5115
	10000	3.0242	0.4777
	100000	5.9315	0.4585
	200000	6.5155	0.4570
	500000	7.0442	0.4564
7	1	2.4434	0.6025
	10000	3.5948	0.5736
	100000	6.8267	0.5524
	200000	7.4591	0.5508
	500000	8.0577	0.5501
8	1	3.2977	0.7089
	10000	4.4585	0.6858
	100000	8.2941	0.6615
	200000	9.0315	0.6596
	500000	9.7308	0.6588
9	1	4.7838	0.8365
	10000	5.9061	0.8207
	100000	10.4540	0.7920
	200000	11.3008	0.7899
	500000	12.1626	0.7890

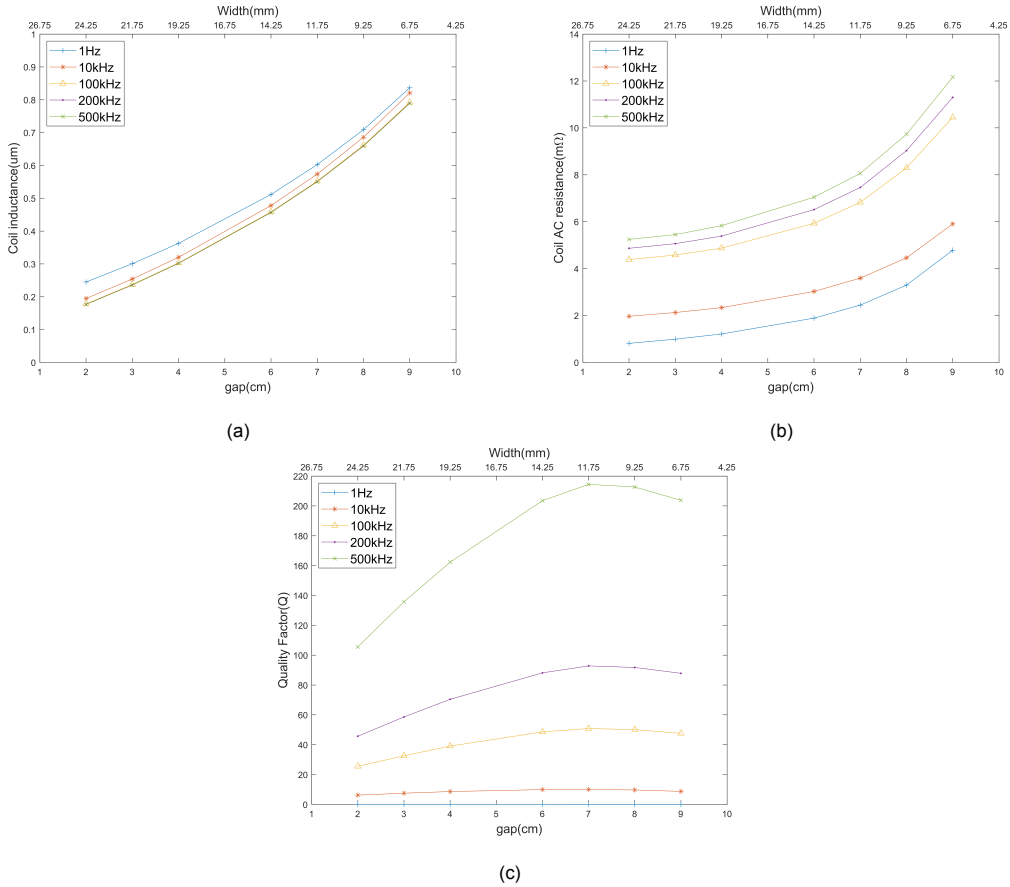

Figure D.1: 2Turn coil with varying gap size (a) Inductance (b) Resistance (c) Quality factor

Planar Coil with 3 Turns

Table D.3: Effect on the resistance and inductance of 3-Turn coil due to varying spacing between the coils(s)

s (mm)	freq (Hz)	Coil inductance (uH)	Coil resistance (AC) (mΩ)	Q-factor
0.5	1	0.5784	1.8396	0.00
	1000	0.5664	2.0531	1.73
	10000	0.4714	5.7892	5.12
	50000	0.4041	19.1975	6.61
	100000	0.3781	27.7274	8.57
	500000	0.3596	35.6720	31.67
1	1	0.5785	1.8816	0.00
	1000	0.5675	2.0800	1.71
	10000	0.4778	5.3830	5.58
	50000	0.4230	14.3024	9.29
	100000	0.4074	18.6702	13.71
	500000	0.3974	22.7851	54.80
1.5	1	0.5787	1.9252	0.00
	1000	0.5686	2.1099	1.69
	10000	0.4842	5.1150	5.95
	50000	0.4369	12.1056	11.34
	100000	0.4252	15.1704	17.61
	500000	0.4180	18.2392	72.00
2	1	0.5792	1.9705	0.00
	1000	0.5700	2.1430	1.67

Table D.3 continued from previous page

s (mm)	freq (Hz)	Coil inductance (uH)	Coil resistance (AC) (mΩ)	Q-factor
	10000	0.4902	4.9371	6.24
	50000	0.4476	10.9128	12.89
	100000	0.4378	13.3898	20.54
	500000	0.4319	15.9076	85.30
2.5	1	0.5800	2.0179	0.00
	1000	0.5715	2.1787	1.65
	10000	0.4963	4.7846	6.52
	50000	0.4576	10.0410	14.32
	100000	0.4490	12.1992	23.13
	500000	0.4438	14.4891	96.23
3	1	0.5809	2.0674	0.00
	1000	0.5731	2.2175	1.62
	10000	0.5020	4.6788	6.74
	50000	0.4659	9.4609	15.47
	100000	0.4582	11.3623	25.34
	500000	0.4536	13.4189	106.19
3.5	1	0.5818	2.1189	0.00
	1000	0.5747	2.2591	1.60
	10000	0.5074	4.6022	6.93
	50000	0.4733	9.0453	16.44
	100000	0.4662	10.7903	27.14
	500000	0.4619	12.7089	114.18
4	1	0.5829	2.1727	0.00
	1000	0.5765	2.3038	1.57
	10000	0.5125	4.5550	7.07
	50000	0.4797	8.7458	17.23
	100000	0.4731	10.3263	28.79
	500000	0.4692	12.1551	121.26
4.5	1	0.5844	2.2290	0.00
	1000	0.5785	2.3514	1.55
	10000	0.5181	4.4907	7.25
	50000	0.4870	8.4347	18.14
	100000	0.4808	9.9011	30.51
	500000	0.4772	11.5536	129.75
5	1	0.5858	2.2879	0.00
	1000	0.5805	2.4024	1.52
	10000	0.5228	4.4756	7.34
	50000	0.4927	8.2226	18.83
	100000	0.4869	9.5803	31.93
	500000	0.4835	11.0868	137.01
6	1	0.5893	2.4147	0.00
	1000	0.5849	2.5145	1.46
	10000	0.5329	4.4605	7.51
	50000	0.5042	8.1046	19.54
	100000	0.4985	9.4712	33.07
	500000	0.4951	10.9906	141.52
7	1	0.5934	2.5545	0.00
	1000	0.5899	2.6414	1.40
	10000	0.5430	4.4695	7.63
	50000	0.5155	7.9623	20.34
	100000	0.5101	9.2497	34.65
	500000	0.5069	10.6660	149.30
10	1	0.6086	3.0770	0.00
	1000	0.6069	3.1332	1.22

Table D.3 continued from previous page

s (mm)	freq (Hz)	Coil inductance (uH)	Coil resistance (AC) (mΩ)	Q-factor
	10000	0.5728	4.7265	7.61
	50000	0.5467	8.0345	21.38
	100000	0.5417	9.1712	37.11
	500000	0.5389	10.3514	163.54
12	1	0.6223	3.5476	0.00
	1000	0.6213	3.5887	1.09
	10000	0.5946	5.0369	7.42
	50000	0.5691	8.4106	21.26
	100000	0.5638	9.6025	36.89
	500000	0.5610	10.7301	164.24
15	1	0.6487	4.5671	0.00
	1000	0.6483	4.5916	0.89
	10000	0.6315	5.8353	6.80
	50000	0.6055	9.5013	20.02
	100000	0.5998	10.8293	34.80
	500000	0.5967	12.0691	155.32
18	1	0.6844	6.3271	0.00
	1000	0.6843	6.3402	0.68
	10000	0.6762	7.2781	5.84
	50000	0.6505	11.7006	17.47
	100000	0.6436	13.3264	30.34
	500000	0.6398	14.7009	136.72

Table D.4: Effect on the resistance and inductance of 3-Turn coil due to varying gap size between the coil(g)

g (cm)	freq (Hz)	Coil inductance (uH)	Coil resistance (AC) (mΩ)
0.5	1	0.4306	1.6296
	10000	0.3521	4.0804
	100000	0.3127	9.9790
	200000	0.3099	11.0175
	500000	0.3086	11.8639
1	1	0.4782	1.7933
	10000	0.4018	4.2393
	100000	0.3621	10.0650
	200000	0.3594	11.0694
	500000	0.3582	11.8699
2	1	0.5829	2.1727
	10000	0.5125	4.5550
	100000	0.4731	10.3263
	200000	0.4704	11.3334
	500000	0.4692	12.1551
3	1	0.7017	2.6464
	10000	0.6385	4.9524
	100000	0.5989	10.7963
	200000	0.5961	11.8113
	500000	0.5949	12.6213
4	1	0.8362	3.2573
	10000	0.7808	5.4938
	100000	0.7403	11.5523
	200000	0.7374	12.6071
	500000	0.7362	13.4846
5	1	0.9888	4.0750
	10000	0.9417	6.2508
	100000	0.8994	12.6337
	200000	0.8964	13.7414
	500000	0.8951	14.7147
6	1	1.1630	5.2262
	10000	1.1249	7.3319
	100000	1.0798	14.2356
	200000	1.0766	15.4069
	500000	1.0752	16.4146
6.5	1	1.2603	5.9982
	10000	1.2274	8.0224
	100000	1.1807	15.5266
	200000	1.1771	16.8492
	500000	1.1756	18.0124
7	1	1.3639	6.9677
	10000	1.3364	8.9217
	100000	1.2875	16.5042
	200000	1.2841	17.7570
	500000	1.2827	19.0045

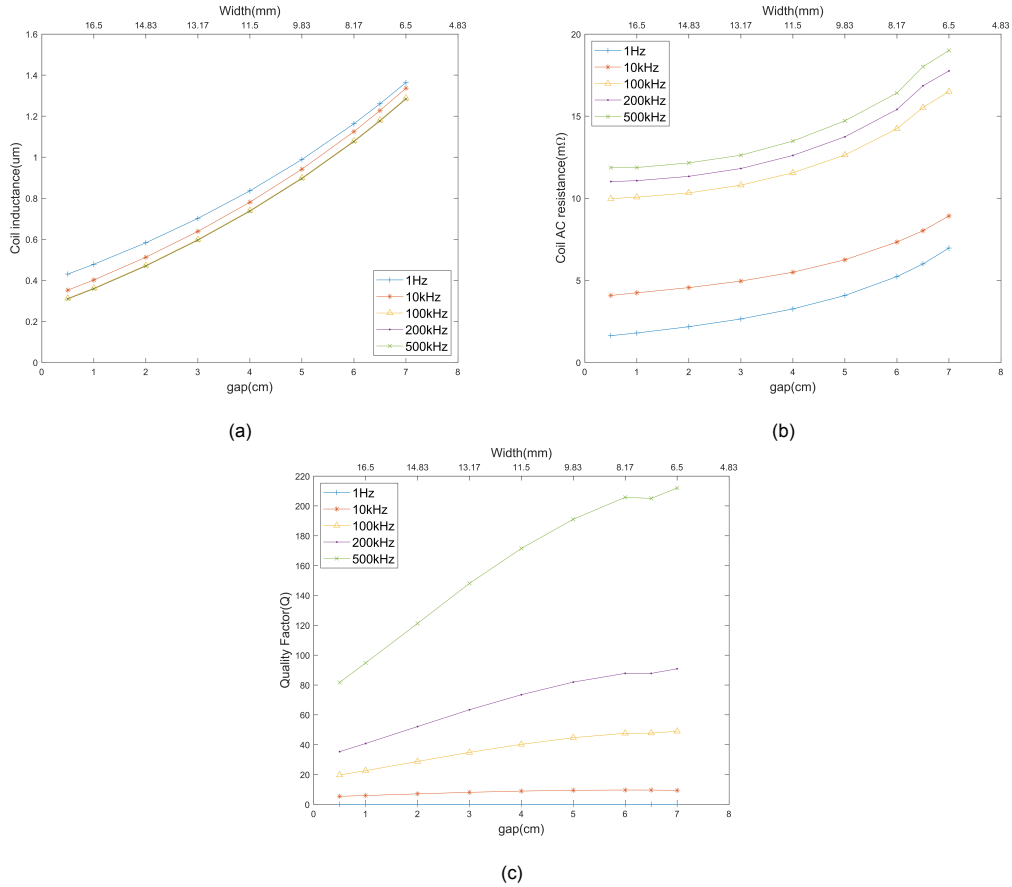

Figure D.2: 3Turn coil with varying gap size (a) Inductance (b) Resistance (c) Quality factor

Planar Coil with 5 Turns

Table D.5: Effect on the resistance and inductance of 5-Turn coil due to varying spacing between the coils(s)

s (mm)	freq (Hz)	Coil resistance (DC) (mΩ)	Coil inductance (uH)	Quality Factor (Q)
0.5	1	11.0592	1.6786	0.001
	1000	11.1944	1.6765	0.941
	10000	19.0601	1.5899	5.241
	50000	62.6133	1.4163	7.106
	100000	112.8234	1.3263	7.386
	500000	205.9082	1.1952	18.236
1	1	11.5495	1.6773	0.001
	1000	11.6669	1.6756	0.902
	10000	18.4868	1.5981	5.431
	50000	49.8109	1.4471	9.127
	100000	77.3398	1.3856	11.257
	500000	117.6126	1.3189	35.230
1.5	1	12.0820	1.6772	0.001
	1000	12.1839	1.6757	0.864
	10000	18.2111	1.6077	5.547
	50000	43.7513	1.4734	10.580
	100000	63.0742	1.4251	14.196
	500000	88.0131	1.3797	49.247
2	1	12.6613	1.6784	0.001
	1000	12.7502	1.6772	0.826

Table D.5 continued from previous page

s (mm)	freq (Hz)	Coil resistance (DC) (mΩ)	Coil inductance (uH)	Quality Factor (Q)
	10000	18.1239	1.6178	5.608
	50000	40.2767	1.4966	11.673
	100000	55.6651	1.4556	16.430
	500000	74.5934	1.4199	59.799
2.5	1	13.2955	1.6800	0.001
	1000	13.3726	1.6790	0.789
	10000	18.1867	1.6278	5.624
	50000	38.1264	1.5168	12.498
	100000	51.0758	1.4804	18.211
	500000	65.8352	1.4509	69.234
3	1	13.9929	1.6828	0.001
	1000	14.0597	1.6819	0.752
	10000	18.3691	1.6378	5.602
	50000	36.5660	1.5362	13.198
	100000	48.0278	1.5033	19.666
	500000	60.6093	1.4773	76.575
3.5	1	14.7634	1.6871	0.001
	1000	14.8209	1.6864	0.715
	10000	18.6480	1.6489	5.556
	50000	35.3596	1.5564	13.829
	100000	45.9851	1.5264	20.856
	500000	58.1969	1.5021	81.085
4	1	15.6170	1.6909	0.001
	1000	15.6666	1.6903	0.678
	10000	19.0638	1.6587	5.467
	50000	34.7352	1.5742	14.238
	100000	44.9040	1.5460	21.633
	500000	57.1655	1.5224	83.667
4.5	1	16.5681	1.6969	0.001
	1000	16.6108	1.6964	0.642
	10000	19.6616	1.6700	5.337
	50000	34.5492	1.5902	14.460
	100000	43.3223	1.5640	22.684
	500000	53.3074	1.5438	90.983
5	1	17.6387	1.7035	0.001
	1000	17.6750	1.7031	0.605
	10000	20.3715	1.6815	5.186
	50000	34.7997	1.6075	14.512
	100000	43.0622	1.5820	23.083
	500000	52.0050	1.5632	94.432
6	1	20.2305	1.7192	0.001
	1000	20.2564	1.7190	0.533
	10000	22.3086	1.7050	4.802
	50000	35.8500	1.6441	14.407
	100000	44.5033	1.6189	22.856
	500000	53.9835	1.5994	93.078
7	1	23.6589	1.7381	0.000
	1000	23.6768	1.7380	0.461
	10000	25.2019	1.7297	4.312
	50000	38.0358	1.6794	13.871
	100000	46.5588	1.6546	22.329
	500000	55.3406	1.6359	92.865
8	1	28.4315	1.7596	0.000
	1000	28.4432	1.7596	0.389

Table D.5 continued from previous page

s (mm)	freq (Hz)	Coil resistance (DC) (mΩ)	Coil inductance (uH)	Quality Factor (Q)
	10000	29.4873	1.7552	3.740
	50000	40.7948	1.7188	13.237
	100000	50.0114	1.6951	21.297
	500000	59.9527	1.6749	87.768
9	1	35.5164	1.7872	0.000
	1000	35.5233	1.7872	0.316
	10000	36.1588	1.7851	3.102
	50000	44.8182	1.7634	12.361
	100000	54.5124	1.7438	20.099
	500000	68.5399	1.7209	78.877
10	1	47.0994	1.7905	0.000
	1000	47.1018	1.7904	0.239
	10000	47.3222	1.7897	2.376
	50000	50.4027	1.7822	11.108
	100000	53.7655	1.7750	20.743
	500000	58.3851	1.7675	95.107
11	1	69.6422	1.8509	0.000
	1000	69.6431	1.8508	0.167
	10000	69.7301	1.8506	1.668
	50000	71.1923	1.8481	8.155
	100000	73.6227	1.8447	15.743
	500000	79.9185	1.8379	72.246

Table D.6: Effect on the resistance and inductance of 5-Turn coil due to varying gap size between the coil(g)

g (cm)	freq (Hz)	Coil resistance (AC) (mΩ)	Coil inductance (uH)
0.5	1	11.4980	1.2881
	10000	15.6095	1.2439
	100000	40.6246	1.1246
	200000	46.8773	1.1095
	500000	50.8959	1.1033
1	1	12.7061	1.4122
	10000	16.6460	1.3719
	100000	42.1506	1.2528
	200000	48.5766	1.2374
	500000	52.7287	1.2310
1.5	1	14.0691	1.5469
	10000	17.7731	1.5106
	100000	43.4133	1.3944
	200000	50.1786	1.3786
	500000	54.4679	1.3719
2	1	15.6170	1.6909
	10000	19.0638	1.6587
	100000	44.9040	1.5460
	200000	52.3271	1.5297
	500000	57.1655	1.5224
2.5	1	17.3913	1.8450
	10000	20.6041	1.8172
	100000	46.2069	1.7057
	200000	53.1292	1.6900
	500000	57.6995	1.6832
3	1	19.4476	2.0107
	10000	22.4285	1.9870
	100000	48.4874	1.8763
	200000	55.2869	1.8607
	500000	60.1945	1.8538
3.5	1	21.8614	2.1888
	10000	24.5413	2.1691
	100000	51.2779	2.0627
	200000	58.5181	2.0462
	500000	63.4190	2.0390

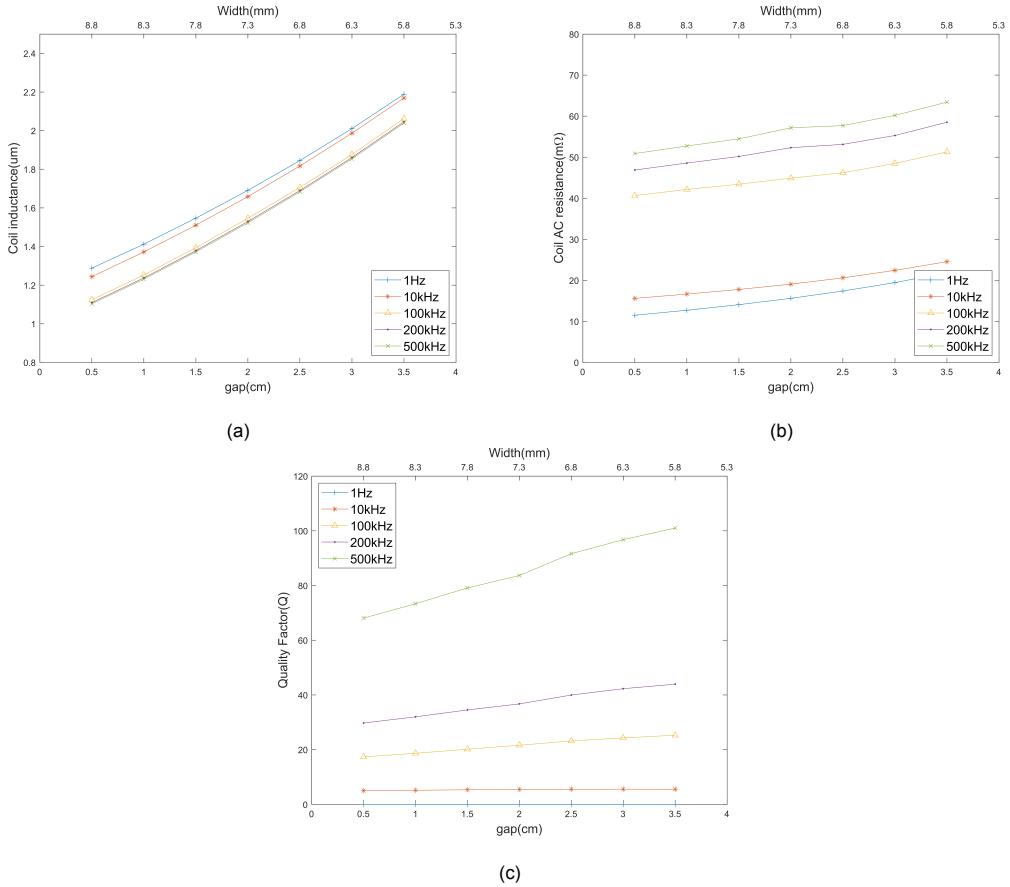

Figure D.3: 5Turn coil with varying gap size (a) Inductance (b) Resistance (c) Quality factor

E

Datasheets

Figure E.1: Maxeon3 Solar Module

MAXEON™ GEN III SOLAR CELLS

Electrical Characteristics of a typical Maxeon Gen III Cell
At Standard Test Conditions (STC)
STC: 1000W/m², AM 1.5G and cell temp 25ºC

	Cell Bin	Pmpp (Wp)	Eff. (%)	Vmpp (V)	Impp (A)	Voc (V)	Isc (A)
Ultra Peak Performance	Me1	3.72	24.3	0.632	5.89	0.730	6.18
Ultra Premium Performance	Le1	3.63	23.7	0.621	5.84	0.721	6.15
Ultra High Performance	Ke1	3.54	23.1	0.612	5.79	0.713	6.11

Electrical parameters are nominal values.
Temp.Coefficients in SunPower Panels: Voltage: -1.74mV/ºC, Current: 2.9mA/ºC, Power: -0.29%/ºC

Spectral Response

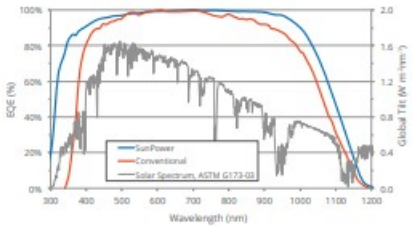

References
SunPower: NREL data, commissioned by SPWR
Conventional: Progress in Photovoltaics: Research and Applications, Solar cell efficiency tables, version 36 18(5), (2010) 46–352

Cell Physical Characteristics

Wafer:	Monocrystalline silicon
Design:	All back contact
Front:	Uniform, black antireflection coating
Back:	Tin-coated, copper metal grid
Cell Area:	Approximately 153cm²
Cell Weight:	Approximately 6.5grams
Cell Thickness:	150µm +/- 30µm

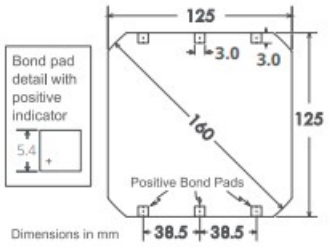

Bond pad area dimensions are 5.4mm x 3.0mm
Metal finger pitch between positive and negative fingers is 471um.
Positive/Negative pole bond pad sides have "+/-" indicators on leftmost and rightmost bond pads

Figure E.2: Solar Cell Maxeon3 datasheet

MAXEON 3 POWER: 390–400 W | EFFICIENCY: Up to 22.6%

Electrical Data			
	SPR-MAX3-400	SPR-MAX3-395	SPR-MAX3-390
Nominal Power (Pnom) [2]	400 W	395 W	390 W
Power Tolerance	+5/0%	+5/0%	+5/0%
Panel Efficiency	22.6%	22.3%	22.1%
Rated Voltage (Vmpp)	65.8 V	65.4 V	65.0 V
Rated Current (Impp)	6.08 A	6.04 A	6.00 A
Open-Circuit Voltage (Voc)	75.6 V	75.6 V	75.5 V
Short-Circuit Current (Isc)	6.58 A	6.57 A	6.56 A
Max. System Voltage	1000 V IEC		
Maximum Series Fuse	20 A		
Power Temp Coef.	−0.27% / °C		
Voltage Temp Coef.	−0.236% / °C		
Current Temp Coef.	0.058% / °C		

Warranties, Certifications and Compliance	
Standard Tests [3]	IEC 61215, IEC 61730
Quality Management Certs	ISO 9001:2015, ISO 14001:2015
Ammonia Test	IEC 62716
Desert Test	IEC 60068-2-68, MIL-STD-810G
Salt Spray Test	IEC 61701 (maximum severity)
PID Test	1000 V: IEC 62804
Available Listings	TUV
IFLI Declare Label	First solar panel labeled for ingredient transparency and LBC-compliance. [4]
Cradle to Cradle Certified™ Bronze	First solar panel line certified for material health, water stewardship, material reutilization, renewable energy & carbon management, and social fairness. [5]
Green Building Certification Contribution	Panels can contribute additional points toward LEED and BREEAM certifications.
EHS Compliance	RoHS, OHSAS 18001:2007, Recycle Scheme, REACH SVHC-163

Operating Condition And Mechanical Data	
Temperature	−40°C to +85°C
Impact Resistance	25 mm diameter hail at 23 m/s
Solar Cells	104 Monocrystalline Maxeon Gen 3
Tempered Glass	High-transmission tempered anti-reflective
Junction Box	IP-68, Stäubli (MC4), 3 bypass diodes
Weight	19 kg
Max. Load [6]	Wind: 2400 Pa, 244 kg/m² front & back Snow: 5400 Pa, 550 kg/m² front
Frame	Class 1 black anodized (highest AAMA rating)

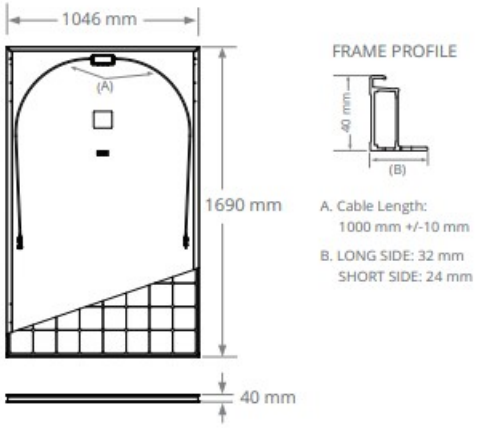

Figure E.3: PV module Maxeon3 datasheet